NTNU – Trondheim
Norwegian University of
Science and Technology

Experimental Studies of Flow- and Electric Properties of Oil Droplets Including Suspended Clay Particles

Alexander Mikkelsen

Physics

Supervisor: Jon Otto Fossum, IFY

Norwegian University of Science and Technology
Department of Physics

Abstract

Experiments on oil droplets made of silicone oil and sodium-fluorohectorite (Na-Fh) clay particles suspended in castor oil were performed. The electric field (E-field)-induced structuring of clay particles placed inside the droplet was studied using two optical microscopes with optical paths normal to one another. This configuration allowed for simultaneous observation of the droplet behavior from both a front view (optical path perpendicular to E-field lines) and a side view (optical path parallel to E-field lines). Prior to the application of the electric field, the Na-Fh particles were randomly dispersed inside and on the surface of the silicone oil droplet. The isotropic distribution in zero field was confirmed by adjusting the focus on the microscope and examining the intersection between the clay particles and focus plane.

The application of direct current (DC) electric fields initiated clay particle movement inside the drop and the formation of a ribbon pattern consisting of short particle chains oriented parallel to the E-field direction. The ribbon formation rate displayed a linear E-field dependence and viscous flow inside the droplet seemed to govern the particle structuring. The viscous flow inside the drop was briefly studied together with the phenomenon of droplet rotation appearing at strong DC E-fields.

The clay particles behaved differently when an alternating current (AC) E-field was applied. AC E-fields (with frequency equal to 200 Hz) produced chain patterns throughout the drop and parallel to the E-field direction. In both the AC and DC E-field, the particle alignment was time-dependent, and after the application of the E-fields, clay particles slowly spread out and clustered in the bottom of the drop. Settling experiments were also performed and revealed that the stress exerted by the surrounding castor oil on the settling silicone oil droplet was reduced by a factor approximately equal to 1.8 when 1% Na-Fh clay particles were added.

The stability and length of oil-water droplets with smectite clay[1] particles formed in an oval microfuidic T-junction and by using the cross-flow shear method have also been studied. Clay particles were found to affect the length of the formed droplets when the flow rate ratio $Q_{\mathrm{d}}/Q_{\mathrm{c}} > 1$[2], but large variations in droplet length and measurement errors make it difficult to conclude whether the effect is systematic or not. The variation in droplet length was generally observed to increase when clay particles were added to the continuous phase (dist. water) and when $Q_{\mathrm{d}}/Q_{\mathrm{c}}$ was increased.

Surface tension measurements performed with the Du Noüy ring method revealed that the distilled water had some impurities that may have interacted with the clay particles. The pendant drop method was later used to perform surface tension measurement of pure dist. water with or without clays exposed to air or oil. Adding clay particles to the water did not change the surface tension considerably. However, droplet lengths measured at the end of the microfluidic chip showed that clay particles might need more time to affect droplet properties.

[1] Laponite, bentonite and sodium fluorohectorite (Na-Fh).

[2] Q_d and Q_c are the flow rate of the dispersed (oil) and continuous phase (dist. water with or without clay), respectively.

Acknowledgements

Firstly I would like to thank my supervisor Professor Jon Otto Fossum for his guidance and inspiration during my work with this thesis, for including me in his research group and for giving me the opportunity to work with interesting projects and people. Some of the experiments presented in this thesis report were performed together with fellow master student Knut Kjerstad at NTNU[3] who did a great job mapping flow patterns and examining the correlation between ribbon formation time and electric field strengths and droplet sizes. I greatly appreciate his valuable inputs and collaboration during the experiments.

I am very grateful to post.doc. fellow Zbigniew Rozynek at NTNU for his encouraging spirit, great assistance and good advices. Ph.D. candidate Rene Castberg at UiO[4] is acknowledged as the author of the MATLAB script used in the electric field experiments and has also been a great resource during my studies.

I also would like to thank Professor Marcio Carvalho and his research group at PUC-Rio[5] for including me with openness and generosity in the research group, for giving me the opportunity to be a part of their research and for their guidance and help with the experiments performed at PUC. Finally I want to express my thanks to thank Adrian Rennie at UU[6] for both accommodating me and helping me with superficial and interfacial surface tension measurements at his laboratory, as well as for sharing his knowledge on the subject.

[3]Norwegian University of Science and Technology.
[4]University of Oslo.
[5]Pontifícia Universidade Católica do Rio de Janeiro.
[6]University of Uppsala.

Contents

List of Figures

List of Tables

Chapter 1

Introduction

Smectite clays are of great scientific interest because of their plethora of unique physiochemical properties, e.g. extremely small crystal size (a few nanometers), large cation exchange capacity, variations in surface charge and types of exchangeable ions, large and chemically active surface area and interactions with inorganic and organic liquids (Odom, 1984). Industrial applications for clays range from petroleum-relevant areas (rheology modification, oil well-drilling and -stability) to food and cosmetics (Velde, 1992). Clay particles are also known to change and/or improve physical properties (i.e. mechanical strength, thermal stability, conductivity, etc.) of the medium they are suspended in (Walls et al., 2003; Kim et al., 2008; Ratna et al., 2006). Being abundant, inexpensive, and environment friendly, clays are by some authors recognized as "the materials of the 21st century"(Bergaya et al., 2006). Research and studies of liquid suspensions of clays have increased significantly the recent years (see figure C.5). However, understanding the complex physical phenomena in clay systems and their applications is far from complete.

Microfluidics, dealing with devices, the behavior, precise control and manipulation of fluids at the micrometer length scale, is an area that has received considerable attention in recent years (Thorsen et al., 2001; Kobayashi et al., 2001; Sugiura et al., 2004; Stone et al., 2004; Garstecki et al., 2006; Zhao and Middelberg, 2011). The force balance in microfluidic systems is totally different from normal decimetric systems. The surface to volume ratio is much higher (by several orders of magnitude), capillary forces dominate viscous shear forces and gravity is usually neglected. Certain laboratories have tried to use the dominant capillary forces in a constructive manner, and this has given rise to the microfluidics of drops, called digital microfluidics. The object of this field is to transport and transform fluid samples in a controlled manner, not in canals, but in drops (Tabeling, 2005).

The first commercialized product produced on a large scale using microfluidic technology was the ink jet printer head. With the technology commercially established, the path from ink jet printer heads to highly controlled micro droplet dispensers was a short one. Instead of controlling small drops on paper, plates containing wells for chemical or biological analyzes were used. The small size of microfluidic devices has many advantages over that of normal sized systems. Small sample volumes can quickly be analyzed at low cost, and with high resolution and sensitivity. Short molecular diffusion distances and the capability for precise control and manipulation of flows are other important microfluidic device characteristics.

Microfluidic chips produced by the millions allow for a massive number of tests and experiments to be run in parallel. These parallel experiments save time and greatly widen the experimental scopes. The ultimate goal is to build a large system of chips, a so-called lab on a chip, used to detect, mix and transport biological molecules, characterize raw samples and control chemical reactions, all with one small device. Functional microfluidic devices, such as mixers, heaters, pumps, sensors and separators have already been developed (Stone et al., 2004), but there is still an enormous amount of progress to be made in this domain. Chemical engineering and the miniaturization of factories are other fields for microfluidics. Better control of endothermic- or exothermic reactions and reduction of transport- and chemical-contamination risks are the main advantages. The appeal of microsystems for chemical engineering has been present since 1996 and is is a field being actively explored and developed today (Ehrfeld et al., 1996; Srinivasan et al., 1997). Much is expected from the microfluidic field in the future. In 2001 microfluidics was declared to be one of ten technologies capable of "changing the world"(Weigl and Hedine, 2002).

Electric fields (E-fields) have the ability to induce fluid motion in liquids, and conversely, fluid flow can give rise to an E-field (Melcher and Taylor, 1969). When affected by an E-field, liquid drops have several responses, like deformation, rotation, coalescence or breakup. The drop behavior is governed by a force balance between electrical forces caused by free charges in the interior and exterior of the drop, interfacial surface tension and drag forces from induced viscous flows. Fluid motion that can be controlled by an E-field has a wide range of applications, i.e. electro-sprays, ink-jet printing, electrohydrodynamic pumps, etc. (Salipante and Vlahovska, 2010).

Adding smectite clays in various concentrations to droplets makes the droplet behavior more complex and may be an interesting way to align and/or organize the clay particles and while simultaneously controlling droplet properties. Soft displays, lab-on-a-chip for accurate chemical reactions, biological processes or even boolean logic (for simple microfluidic computing) are suggested uses for such "smart" droplets (Niu et al., 2009). Studies of dielectric droplet deformation can also be useful for understanding deformation of biological cells subject to E-field. Clay particles in oil suspensions are known as electrorheological fluids (ERFs) since the internal ordering of the clay particles often leads to dramatic changes in the rheological properties (viscosity, yield stress, shear modulus, etc.) of the suspensions (Wen et al., 2003). If an E-field is applied and strong enough (usually 1 kV/mm), the clay particles become polarized. The particles consequently orient in the E-field and aggregate, which results in the formation of chain-like structures parallel to the electric field direction (Fossum et al., 2006; Wang et al., 2009; Rozynek et al., 2010).

While pure liquid droplets affected by E-field are well documented in the literature and their behavior mostly understood, research on E-field-controlled liquid droplets with clays is almost nonexistent. Initial studies on E-field controlled deformation of silicone oil drops containing laponite clay particles was recently performed by our research group member Hersvik (2010). His experiments showed that laponite particles affected the time scale of the deformation processes and also formed chain patterns inside the droplet. Motivated by these results, the first part of this study examines silicone oil droplets with different smectite clay particle concentrations and the behavior of droplet and clay particles in various E-fields.

Two phase microfluidic flows are formed when two immiscible (or partially misicble) fluids are brought into contact in microfluidic devices. The applications for such flows are numerous, involving reaction (Song et al., 2006), mixing (Tice et al., 2003; Wang et al., 2009), emulsions (Kobayashi and Nakajima, 2002), biomedicine (Jakeway and de Mello, 2000) and material synthesis (Wang et al., 2004; Nisisako and Torii, 2007). Manipulating and controlling droplet size, size distribution, flow behavior and flow pattern is crucial in all these applications. These demands are met by the microfluidic technology and monodispersed droplets formed in microfluidic devices. One of the most frequently used microfluidic geometries to produce monodispersed droplets is a T-junction by using the cross-flow shear method (Thorsen et al., 2001; Tice et al., 2003; Zheng and Ismagilov, 2005; Xu et al., 2008). This method generates droplets that are highly monodispersed with an equal spacing between drops. In spite of the popularity of the T-junction geometry, no cross-flow experiments containing smectite clay particles have been performed. The smectite clay particles are expected to be surface active and thus alter the capillary force and droplet properties in the two phase flow.

The use of clay particles is also expected to influence the stability of emulsions. Several techniques for producing monodisperse emulsions have been developed in the last decade, including shear breakage of polydisperse viscous droplets in viscoelastic complex fluids (Mason and Bibette, 1997), membrane emulsification (Nakashima et al., 1991), emulsification of micro-channel (Kawakatsu et al., 1997) and co-continuous phase flow through capillary devices (Umbanhowar et al., 2000). A number of groups have also tried to create emulsions in microfluidic systems (Umbanhowar et al., 2000; Sugiura et al., 2001). The experiment of Thorsen et al. (2001) proved that interesting structures, such as intertwined droplets, can be the basis for forming an emulsion. Emulsions are generally stabilized by the use of surfactants, but solid particles dissolved in one phase can also stabilize emulsions (Binks, 2002). This is known as pickering emulsion. The solid particles adsorbs at the interface of the two liquids, thereby creating a physical barrier that hinders coalescence. Clay minerals are known to produce very stable pickering emulsions (Binks, 2002; Ashby and Binks, 2000). Experimenting with clay particles and pickering emulsion in microfluidic geometries constitutes a departure point for the development of systems that may, in the future, allow for the creation of "tailor-made" emulsions. (Tabeling, 2005)

Formations of water-oil emulsions in porous media in oil reservoirs is a common phenomenon in the oil extraction industry. Pumping water down to the porous media produces a two phase flow involving complex dynamics of coalescence and breaking up of droplets, resulting in a wide distribution of droplet sizes. The oil-water interfaces are difficult to stabilize and separate, and the difficulties result in residual oil in the pores and increased extracting expenses (Kokal, 2005; Raikar et al., 2009). Pumping water with clay particles in it through oil in porous media resembles the stirring of oil-water mixtures, and could produce a kind of pickering emulsion that would stabilize the oil-water interfaces. Depending on the solubility of the particles, an oil-in-water emulsion can be transformed into a water-in-oil emulsion depending on whether the solid particles are hydrophobic or hydrophilic (Yan et al., 2001). The relative effect of viscous forces to interfacial tension forces is given by the Capillary number (Ca), an important parameter in microfluidics: $Ca = \mu u/\sigma$, where μ is the dynamic viscosity, u is the characteristic velocity of the injected fluid and σ is the interfacial tension between the two fluids. Literature data show

that the percentage of oil recovery in porous media, considering the residual oil saturation, is essentially zero when the capillary number is less than 10^{-6} and essentially 100% when higher than 10^{-3} (Baviere, 1991). Thus, if we could increase the number of capillary action in three or four orders of magnitude, we could also achieve a recovery of almost 100% of oil in the swept area.

There are many mechanisms for emulsion formation in porous media. One mechanism is external pumped water pressing oil out of pores and into the water flow. This two phased flow is well-modeled by the flow in microchannels meeting at a T-junction. Campos (2011) studied the flow of different oil-water systems, their properties and their behavior in an oval microfluidic T-junction by using the cross-flow shear method. His experiments showed that fluid parameters like viscosity, flow rates and interfacial tension all affected the formed droplet lengths. Using this as a starting point, the second part of this study examines two phase oil-water flows with smectite clay particles and how the clay particles affect the stability and length of formed droplets in a microfluidic T-junction.

The layout of this thesis report is as follows. Firstly, the thesis report introduces fundamental theory, models and relevant work from literature in chapter 2. The experimental set ups and methods are then explained in chapter 3 and 4, respectively. In chapter 5, the experimental results are presented and discussed in detail. As mentioned earlier, the study is divided in two main works with experiments investigating (1) oil droplet and clay behavior in applied E-fields, and (2) oil-water two phase flow with clay particles. The two works will be described, presented and discussed in sequence in each of the previously mentioned chapters starting with (1). Finally, conclusions, suggestions for further work and a summary of the main results are presented in chapter 6.

Chapter 2

Theory

Some basic theory and concepts are necessary to understand and describe the later experimental results. These topics include, among others; clay and its properties, electrorheology, surface tension, wetting, surfactants, mechanism for droplet creation in T-junctions and some models. Important previous results and work found in the literature will also be presented and utilized.

2.1 Smectite clays and their properties

Smectite clays are of great scientific interest because of their unique and varied physiochemical properties like extremely small crystal size, variations in internal chemical composition, structural characteristics caused by chemical factors, large cation exchange capacity, large surface area that is chemically active, variations in types of exchangeable ions and surface charge, and interactions with inorganic and organic liquids (Odom, 1984). The most relevant properties for this work will be described in more detail in this section.

Smectite clays are build up by layers of negatively charged oxygen atoms together with different types of positively charged cations placed in fixed and specific positions. A two-dimensional schematic diagram of the structure is presented in figure 2.1. Oxygen and Silicon atoms (and sometimes A^{3+} and Fe^{3+}) together form tetrahedral sheets (layer 1 and 3 in figure 2.1) with the tetrahedral apexes pointing toward each other. Between the two tetrahedral layers there is a octahedral sheet that may contain cations like Al^{3+}, Fe^{3+}, Fe^{2+} Mg^{2+} or Li^{+}. Smectite structures are classified as 2:1 phyllosilicates based on the presence of the two tetrahedral sheets and the one octahedral sheet (Odom, 1984).

An interlayer consisting of loosely held hydrated cations separates the smectite structural units (layer 1-3). The presence of these cations is necessary to balance the negatively charged structure caused by internal substitution of ions in the tetrahedral and octahedral sheet. Interlayer surface and cation hydration between smectite structural units is a unique property of smectite clays (Odom, 1984). Type and location of cations in the tetrahedral and octahedral framework distinguish different clays in the smectite group. The charge on the smectite layers is intermediate and varies from 0.4 to 1.2 e^{-1} per unit cell (Si_8O_{20}) (Beson et al., 1974). Fluorohectorite, montmorillonite (bentonite) and laponite are the most relevant silicate clay members for our experiments. Some of their physical properties are summarized in table 2.1.

Table 2.1: Physical properties of laponite, montmorillonite and fluorohectorite. CEC is the cation exchange capacity, BET is the particle surface area calculated with BET theory and ρ is the particle charge density. The table is adapted from (Kaviratna et al., 1996).

Clay	Part. size (Å)	CEC (meq/100 g)	BET (m^2g^{-1})	ρ (e^{-1}/u. cell)
Laponite	200	48	300	0.4
Montmorillonite	2000	90	80	0.6
Fluorohectorite	20 000	122	3	1.2

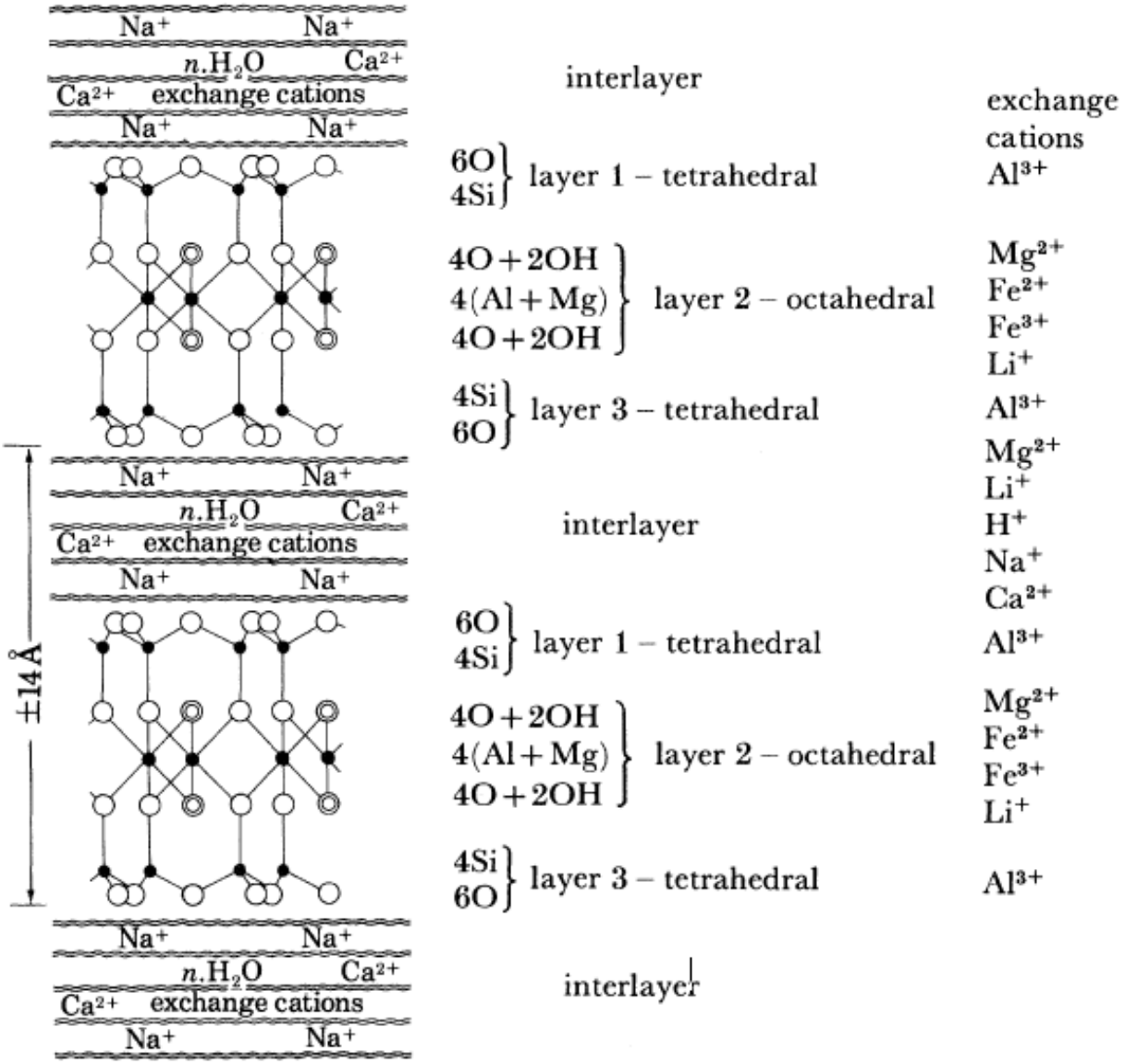

Figure 2.1: Two dimensional shematic diagram of the smectite clay structure. The figure is adapted from (Odom, 1984).

Bentonite is an absorbent aluminum phyllosilicate. It is an impure clay consisting mostly of montmorillonite which has its structural charge originating from substitution of Mg^{2+} for $A1^{3+}$ in the octahedral sheet. Both fluorohectorite and laponite are synthetic hectorites and display two extremes in particle charge and layer size within the smectite group. Fluorohectorite (Fh) has the biggest layer charge per unit cell (1.2 e^{-1}) of the three listed clay types. It's layer charge results from the substitution of Li^{+} for Mg^{2+} in the octahedral sheet. Fluorohectorites differ from natural hectorites in that the OH groups have been replaced by F. Laponite has its charge from the same ion substitution as Fh, but as opposed to fluorohectorite, none of the OH groups have been replaced by F. Alkaline earth ions like Ca and Mg and/or the alkali metal Na are typical hydrated cations in the interlayer used to balance the negative surface charge. Sodium fluorohectorite (Na-Fh) has the nominal chemical formula $Na_{0.6}[(Mg_{2.4}Li_{0.6})Si_4O_{10}F_2]$ per half unit cell (da Silva et al., 2002), while the chemical formula for laponite is $Na_{0.7}[(Mg_{5.5}Li_{0.3})Si_8O_{20}(OH)_4]$ per unit cell (Ashby and Binks, 2000).

In dry form, clay can be seen as small grains (figure 2.2 a) made of crystalline platelets (figure 2.2 b). For some clays, like Na-Fh, the stack of platelets can be quite thick compared to their diameter. Na-Fh clay contains 80 - 150 platelets on average with thickness in the 30 - 150 nm range, while the diameter varies from around 100 nm - 20 μm (DiMasi et al., 2001). The polydispersity in particle size allows Na-Fh suspensions to be sort by size, which may result in layers of gels, sols and/or sediments. The thickness of the platelet stack makes the clays stiff and rigid against transverse layer distortion. Scanning electron microscopy (SEM) pictures of Na-Fh clay are presented in figure 2.3. The SEM pictures display the high particle aggregate polydispersity in terms of both size and shape. In the right picture (figure 2.3), it is even possible to see an individual particle consisting of a multi-layer stacking of silicate sheets.

Each platelet is made of unit cells (figure 2.2 d) repeated in two directions, resulting in a disc shape (figure 2.2 c). The height of each unit cell is approximately 1 nm. It has been estimated that a typical laponite crystal (platelet) contains up to 2000 of these unit cells (Rockwood, 2010). For laponite dispersed in water, the disc shaped platelet diameter is approximately 30 nm (Ashby and Binks, 2000).

As mentioned earlier, clays have the ability to absorb water and organic compounds in the interlayers between the platelets. This ability makes clays attractive and important within the context of "nanosandwiches" as a basis for nanotechnologies (Oriakhi, 1998). The distance between the platelets and thereby the volume of the clay particles increase when water is intercalated between the platelets. The arrangements and number of water molecules intercalated between the platelets can be controlled by temperature and relative humidity (da Silva et al., 2002, 2003). For Na-Fh there can only exist three stable hydration states, with zero, one or two intercalated water layers. Na-Fh clay in solution does not have the ability to hydrate further or exfoliate. The large layer charge of Na-Fh may be the cause that prevents further separation of the platelets.

As distinct from Na-Fh, laponite platelets do not remain in stacks when dispersed in water. The sodium ions in the interlayer hydrate, the structure swells and the plates separate, resulting in nanometer thick platelets. This distinct "nano-size" allows laponite to form clear gels and films. Addition of polar compounds like salt and surfactants to the laponite dispersion will reduce the osmotic pressure holding the sodium ions away from the particle surface.

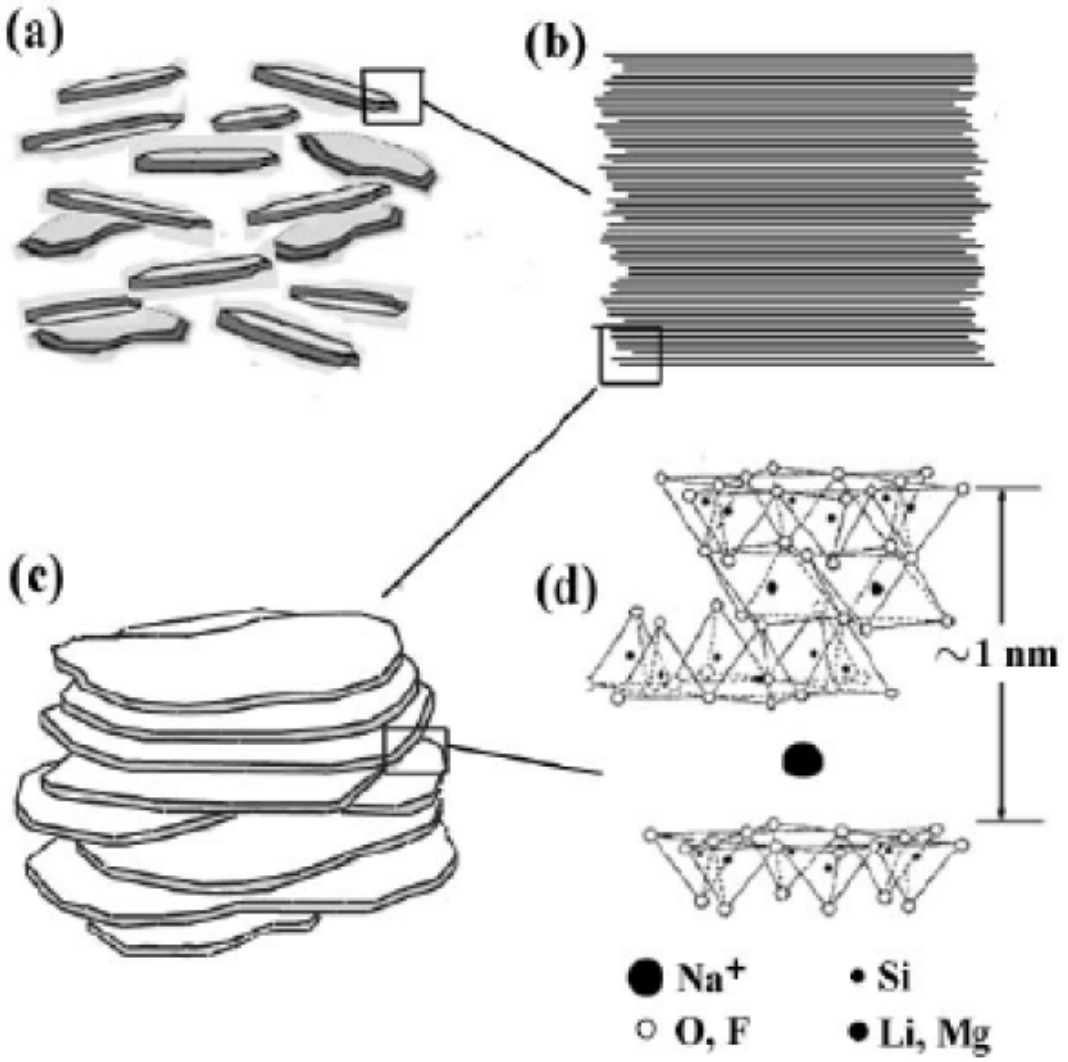

Figure 2.2: Smectite clay from (a) macro scale grains to (d) nano scale atom structure.

This allows the weaker positive charge on the edge of the crystals to interact with the negative surfaces of adjacent crystals (Rockwood, 2010).

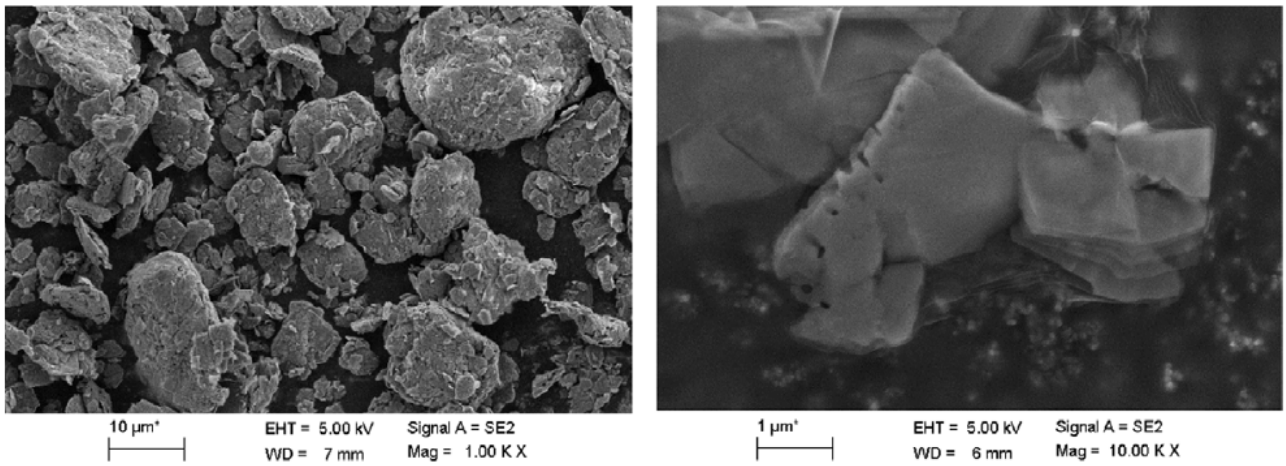

Figure 2.3: SEM images of Na-Fh clay particles with magnifications of 1000 (left) and 10 000 (right), respectively. Images and caption from (Rozynek et al., 2010).

2.2 Dielectric sphere in electric field

Some of the experiments presented later in this thesis report involve studies of silicone oil droplets with clay particles placed in electrical fields (E-fields). We start by calculating the resulting E-field for a solid dielectric sphere embedded in a dielectric medium with a homogeneous E-field applied. A solid dielectric sphere is a simplified model of the droplet and a good starting point to understand the physics behind the experiments. The derivation mainly follows (Griffiths, 1999). In the static case, the potential is related the the applied E-field as:

$$\vec{E} = -\nabla V. \tag{2.1}$$

Gauss's law relates the distribution of electric charge to the resulting electric field:

$$\nabla \cdot \vec{E} = \frac{\rho}{\epsilon_0}, \tag{2.2}$$

where ρ is the charge density and ϵ_0 is the vacuum permitivity. With no free charges on the surface of the sphere and by operating with ∇ on the combination of equation 2.1 and 2.2, we get:

$$\nabla^2 V = 0. \tag{2.3}$$

The boundary conditions for a sphere made of homogeneous linear dielectric material and with radius a are given by:

$$V_{in} = V_{out}, \quad \text{for } r = a, \tag{2.4}$$

$$\epsilon_{in}\frac{\partial V_{in}}{\partial r} = \epsilon_{out}\frac{\partial V_{out}}{\partial r}, \quad \text{for } r = a, \tag{2.5}$$

$$V_{out} \to -E_0\, r\cos\theta, \quad \text{for } r \gg a, \tag{2.6}$$

where E_0 is the applied uniform electric field, r is the distance from the center of the sphere and θ is the angle from the direction of the electric field through the center of the sphere. ϵ_{in} is the permittivity inside the sphere, while ϵ_{out} is the permittivity of the surrounding material. The solution of eq. 2.3 with the boundary conditions is derived in appendix A. With $\epsilon_r = \epsilon_{in}/\epsilon_{out}$ and $r\ \cos\theta = z$, the field inside the sphere is:

$$\boldsymbol{E} = \frac{3\boldsymbol{E_0}}{\epsilon_r + 2}, \tag{2.7}$$

which shows that the E-field inside the sphere is uniform. The electric field inside and outside the sphere is illustrated in figure 2.4. From appendix A, the potential outside the sphere is:

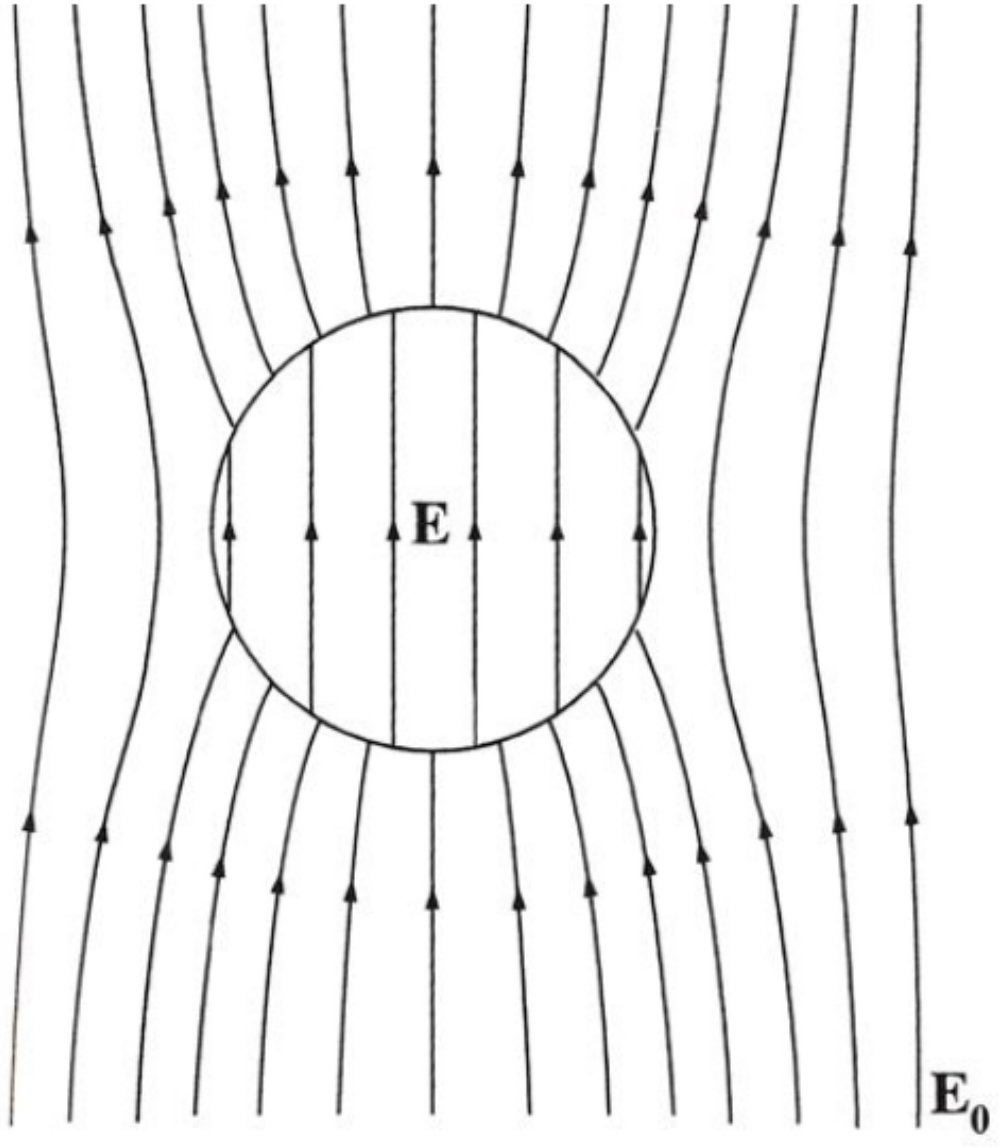

Figure 2.4: Electric field inside and outside a dielectric sphere when a homogeneous uniform electric field E_0 is applied. Illustration from Griffiths (1999).

$$V = \frac{B_1 \cos\theta}{r^2}, \tag{2.8}$$

while the potential of a general dipole field is:

$$V = \frac{p \cos\theta}{4\pi\epsilon_0 r^2}. \tag{2.9}$$

Using the expression for B_1 (eq. A.18) and combining eq. 2.8 and 2.9, the total dipole moment is given by:

$$\vec{p} = 4\pi\epsilon_0 \frac{\epsilon_{in} - \epsilon_{out}}{\epsilon_{in} + 2\epsilon_{out}} a^3 \vec{E_0}. \tag{2.10}$$

Like the E-field, the polarization $\vec{P}$ inside the sphere is constant. The total dipole is equal to the volume integral of the polarization $\vec{P}$ which is expressed by:

$$\vec{P} = \frac{p}{\frac{4}{3}\pi a^3} = 3\epsilon_0 \frac{\epsilon_{in} - \epsilon_{out}}{\epsilon_{in} + 2\epsilon_{out}} \vec{E_0}. \tag{2.11}$$

Since $\vec{P}$ is parallel to $\vec{E_0}$, the polarization charge on the surface of the sphere can be expressed as:

$$q_\sigma = \vec{P} \cdot \hat{n} = P\cos\theta, \tag{2.12}$$

where $\hat{n}$ is the unit vector normal to the sphere surface and $\vec{P}$ is given by eq. 2.11. We see that the sphere is a dipole since positive surface charges are induced on one pole (side) of the sphere while negative surface charges are induced on the other pole.

2.3 The perfect dielectric model

In a study of aerosol droplet distortion, Konski and Tacher Jr. (1953) developed a model for droplet deformation in a constant electric field . The deformation of insulated droplets was described by minimizing the sum of surface energy and electric potential energy of the droplet ellipsoid. By balancing interfacial surface tension and electrical forces, Allan and Mason (1962) described the same deformation. The applied E-field acts on the polarized surface charges (given in eq. 2.12) and deforms the droplet by stretching it along the E-field direction. For small deformations of *conducting* drops in a dielectric medium, both methods predict:

$$D = \frac{9}{16}\frac{a\epsilon_{out}\epsilon_0 E_\infty^2}{\sigma}, \tag{2.13}$$

where D is the deformation of the drop, a is the droplet radius, ϵ_{out} is the relative permittivity of the surrounding fluids, ϵ_0 the vacuum permittivity, E_∞ is the applied field strength and σ is the interfacial surface tension. The droplet deformation is defined as:

$$D = \frac{d_\parallel - d_\perp}{d_\parallel + d_\perp}, \tag{2.14}$$

where $d_\parallel$ is the length or diameter of the drop in the direction parallel to the electric field and $d_\perp$ is the diameter in the direction perpendicular to the electric field. A droplet with $D > 0$ ($d_\parallel > d_\perp$) has a prolate shape, while a droplet with $D < 0$ ($d_\parallel < d_\perp$) is defined as an oblate drop. For a *conducting* droplet in equilibrium, the pressure inside and outside the drop is uniform. The electric stresses on the droplet are balanced by the interfacial tension at the droplet surface. The applied E-field induces a dipole proportional to $\cos\theta$, where θ is the angle from the direction of the E-field. An E-field normal to the droplet surface will thus create stress that varies as $\cos^2\theta$ which will stretch the droplet along the direction of the applied field, resulting in a prolate deformation.

For a *dielectric* drop with a dielectric medium outside, the deformation is more complicated than eq. 2.13:

$$D = \frac{9}{16}\frac{a\epsilon_{out}\epsilon_0 E_\infty^2}{\sigma}\frac{(\epsilon_{in} - \epsilon_{in})^2}{(\epsilon_{in} + 2\epsilon_{in})^2}. \tag{2.15}$$

As seen in eq. 2.12, the induced dipole charges are proportional to $\cos\theta$. The applied E-field will pull the charges at each droplet pole in opposite directions, resulting in a prolate deformation. For both a conductive and dielectric droplet, the deformation is proportional to E^2. A reversal of the E-field will therefore give the same prolate deformation. However, Allan and Mason (1962) observed oblate deformations for dielectric droplets which cannot be predicted by the perfect dielectric model. The surrounding carrying fluid could no longer be viewed as an insulator. Based on this, the leaky dielectric model was developed.

2.4 The leaky dielectric model

Taylor (1966) realized that no matter how small the conductivity of the surrounding liquid, charges will always be able to reach the drop interface, i.e., the fluids are not perfect dielectrics as assumed before. He discovered that electric stress caused by the free mobile charges built up at the drop interface had to be balanced by variable pressure difference between the inside and outside of the drop. The fluids are dragged into motion and viscous flows inside and outside of the drop create the needed pressure difference. The electrostatic approximation can safely be utilized in this model since the characteristic time for electric processes, $t_C \equiv \epsilon/\sigma$, is much greater than the typical time for magnetic processes, $t_M \equiv \mu\sigma l^2$ (Saville, 1997).

Taylor based his model on the assumption that the potential in and outside the droplet can be approximated by the potential in and outside a static *conducting* sphere submerged in a conducting fluid. The assumption is fair since the electric charge conduction is relative fast compared to the fluid motion that convects charge. In most cases, the effects of charge convection are likely to be negligible. The potential inside V_{in} and outside V_{out} is given by (Taylor, 1966):

$$V_{in} = \frac{3}{2+R} E_0 r \cos\theta, \tag{2.16}$$

$$V_{out} = (r + \frac{1-R}{2+R}\frac{a^3}{r^2}) E_0 \cos\theta, \tag{2.17}$$

where $R \equiv \sigma_{in}/\sigma_{out}$ is the ratio of conductivity between the fluid inside and outside the drop. The fluids are assumed to exhibit ohmic resistance. The resulting electrical field therefore exhibits a similar shape as the dielectric sphere illustrated in fig. 2.4. Compared to the dielectric sphere potentials (eq. A.19 and A.20), the potentials for the leaky dielectric model are quite similar.

The component of the electric field tangential to the drop interface must be continuous across the boundary. The electrical stress caused by the applied E-field acts both normally and tangentially at the interface, while the surface tension only acts normally to the drop surface. Taylor therefore found viscous flows necessary to balance the tangential component of the electric stress. Viscosity in the fluid flow produces a drag in the opposite direction which becomes the balancing force along the surface. Taylor developed a discrimination function that predicts whether the deformation will be prolate or oblate (Taylor, 1966):

$$\phi(S, R, \lambda) = S(R^2 + 1) - 2 + 3(SR - 1)(\frac{2\lambda + 3}{5\lambda + 5}), \tag{2.18}$$

where $S \equiv \epsilon_{out}/\epsilon_{in}$ is the permittivity ratio, $\lambda \equiv \mu_{in}/\mu_{out}$ is the viscosity ratio, R the conductivity ratio σ_{in}/σ_{out} and the subscripts in and out denote the values for the fluid inside and outside the drop, respectively. Prolate deformation is predicted when $\phi > 1$, and oblate deformation when $\phi < 1$. Understanding that both a difference in relative permittivity ϵ_i and conductivity σ_i over the drop boundary contribute to shape deformation, the combined effect on drop deformation D is summarized by the following equation (Salipante and Vlahovska, 2010):

$$D = \frac{9}{16}\frac{a\epsilon_{out}E^2}{\gamma S(2+R)^2} \times \phi, \tag{2.19}$$

where ϕ is given in eq. 2.18. From the equations above one realizes that the drop response depends on the mismatch of fluid properties between the interior and exterior drop fluid, represented by R, S and λ. The conduction response of a fluid is given by:

$$SR = \frac{t_{c,out}}{t_{c,in}}, \quad \text{where } t_{c,in} = \frac{\epsilon_{in}}{\sigma_{in}} \; t_{c,out} = \frac{\epsilon_{out}}{\sigma_{out}}. \tag{2.20}$$

The charge relaxation time t_c measures how fast charges are supplied to restore equilibrium. Let us look at the buildup of surface charge on the drop. Firstly, assume that the system (fluid inside and outside drop) has no net charge ($E_0 = 0$, i.e. everything is electrically neutral). If the conductivity inside the drop is higher than the surrounding fluid outside ($t_{c,out} > t_{c,in}$ and $SR > 1$), applying an E-field will allow charges inside the drop to reach the interface faster than the charges in the surrounding fluid. The interface charge distribution is then dominated by charges brought from the interior fluid. This result in a dipole moment aligned with the E-field and a reduced E-field inside the drop. The charges at the drop poles are thus attracted toward the electrodes and the drop is pulled in a prolate shape.

In the opposite case, if the conductivity inside the drop is lower than that of the surrounding phase ($t_{c,out} < t_{c,in}$ and $SR < 1$), the charging of the interface is dominated by charges from the fluid outside the drop. The E-field inside the drop is then enhanced and the drop dipole is reversed and oriented opposite to the applied E-field direction. Either oblate or prolate deformation is possible in this charge configuration. The two charge configurations are illustrated in figure 2.5.

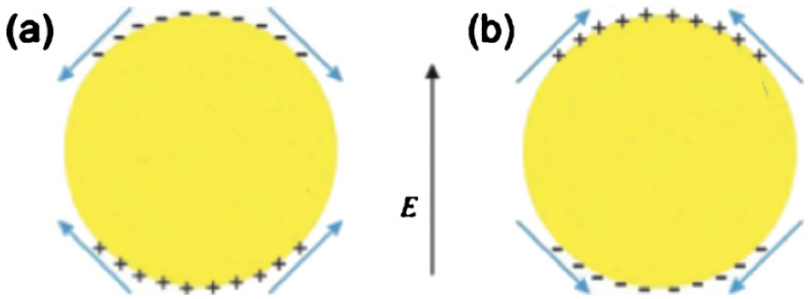

Figure 2.5: Surface charge distribution and direction of surface electric tractions for a drop with (a) $SR < 1$ and (b) $SR > 1$. Picture and caption from (Salipante and Vlahovska, 2010).

The fluid flow along the drop surface has a direction from the drop pole to equator when $SR < 1$ and the other way around when $SR > 1$ (Taylor, 1966). However, deformation does not need to correlate with the flow direction. The viscosity ratio is also observed to have a small effect on the discrimination function (eq. 2.18) as well (Salipante and Vlahovska, 2010). Figure 2.6 displays the viscous flow and direction in more detail when the charge relaxation time t_c is largest inside the droplet.

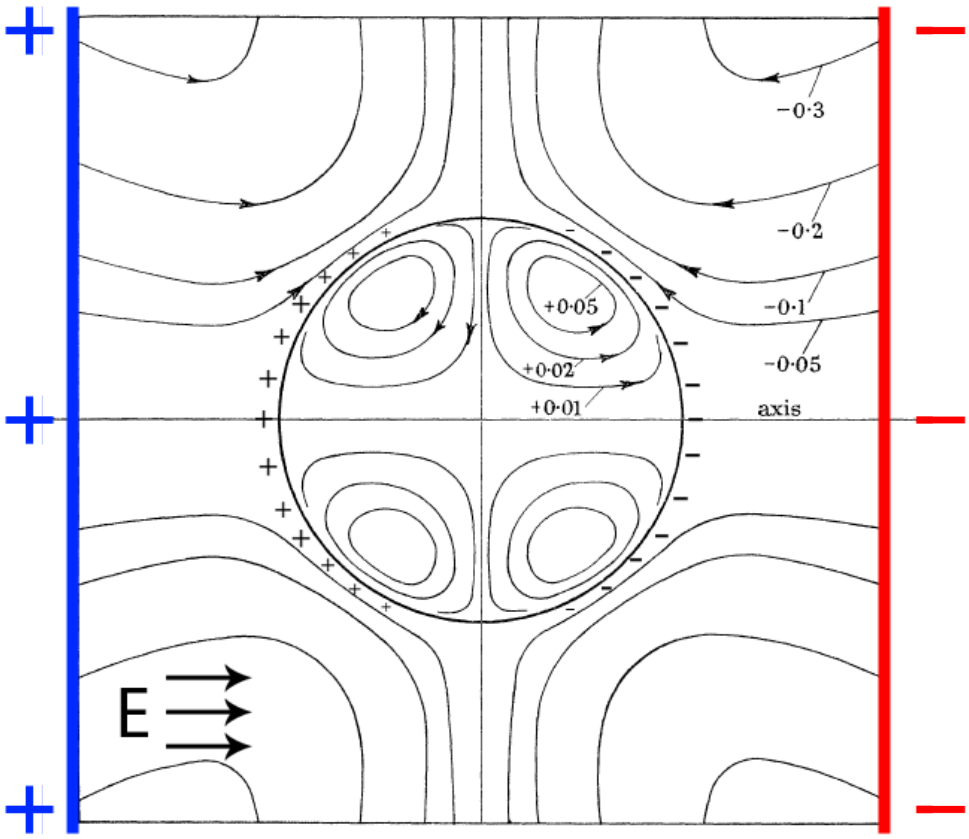

Figure 2.6: Streamlines of viscous flow in dielectric drop when $SR < 1$. The density of fieldlines indicates flow speed. Parallel electrodes run at the sides of the figure creating a uniform electric field indicated by E. Free surface charge accumulation that induce the fluid flow is indicated with + and - signs around the drop surface. Illustration adapted from (Taylor, 1966).

Taylor's leaky dielectric model has been supported by experimental photographs taken by McEwan and de Jong presented in Taylor (1966), and the model is in qualitative agreement with nine of the thirteen cases studied by Allan and Mason (1962). Studies by Torza et al. (1971) showed qualitative agreement with experiments as well, but the results were not consistent with the quantitative aspects of the theory. As predicted, the deformation was proportional to aE_∞^2, but the proportionality factor exceeded the theoretical value in almost all cases. Later, corrections of the leaky dielectric model were developed due to charge convection (Feng, 1999), corrections for larger deformations (Saville, 1997; Baygents et al., 1998) and due to corrections for small conductivities (Zholkovskij et al., 2002), among other reasons.

The leaky dielectric model seems to be accurate for small deformations, but it does not fully capture all phenomena observed in experiments. Nonaxisymmetric drop shapes have been discovered (Krause and Chandratreya, 1998; Ha and Yang, 2000; Sato et al., 2006) where the drop major axis is tilted with respect to the E-field and the fluids undergo rotational flow. This is found only for drops satisfying $SR < 1$ and above a threshold E-field. The observations resemble the Quincke rotation (Quincke, 1896) of a rigid sphere which will be described in the next section.

2.5 Quincke rotation

The spinning of a rigid sphere in a uniform E-field has been known since Quincke (1896) first developed the theory in 1896. For rotation to occur, the induced dipole moment of the sphere has to be oriented opposite to the direction of the applied field (see figure 2.7). As we remember, this is the case when the exterior fluid has a larger conductivity than the interior fluid, i.e. $SR > 1$. This configuration becomes unstable above a critical E-field strength E_Q and a small perturbation is enough to displace the dipole which and make the E-field rotate the sphere. The rotational axis is always perpendicular to $\vec{E}$. As the sphere and its induced surface charge rotate, the exterior fluid recharges the interface. The balance between the electric and hydrodynamic torque gives the rotation rate w (Salipante and Vlahovska, 2010):

$$w = \pm \frac{1}{t_{mw}} \sqrt{\frac{E_0^2}{E_Q^2} - 1}, \tag{2.21}$$

where

$$t_{mw} = \frac{\epsilon_{in} + 2\epsilon_{out}}{\sigma_{in} + 2\sigma_{out}} \tag{2.22}$$

and

$$E_Q^2 = \frac{2\sigma_{out}\mu_{out}(R+2)^2}{3\epsilon_{out}\epsilon_{in}(1-SR)}. \tag{2.23}$$

The charge distribution is given by:

$$Q = \epsilon_{out} E_0 \frac{SR-1}{S(R+2)\sqrt{1+t_{mv}^2 w^2}} \cos(\varphi + \beta), \tag{2.24}$$

where

$$\beta = \arctan(\frac{1}{t_{mw} w}) = \arctan[(\frac{E_0^2}{E_Q^2} - 1)^{-1/2}] \tag{2.25}$$

is the dipole "tilt" angle (see figure 2.7). The equation above shows that β increases with an increasing E-field strength E_0. By examining eq. 2.21, one sees that a rotation is only possible when the electric field E_0 exceeds a critical value given by E_Q.

A droplet cannot be assumed similar to a rigid sphere. As we know, a droplet in a uniform E-field will deform at any field strength. Below the critical field for drop electrorotation E_c, the deformation will be symmetric and can be described by the leaky dielectric model. The flow inside and around the drop gets more complicated when $E_0 > E_c$ and the drop starts to rotate. As the drop rotates, the fluids will be dragged with the drop and acquire a rotational component. The charge convection is affected by the straining flow, and the critical field for drop electrorotation E_c, is different from the critical field for the Quincke rotation E_Q.

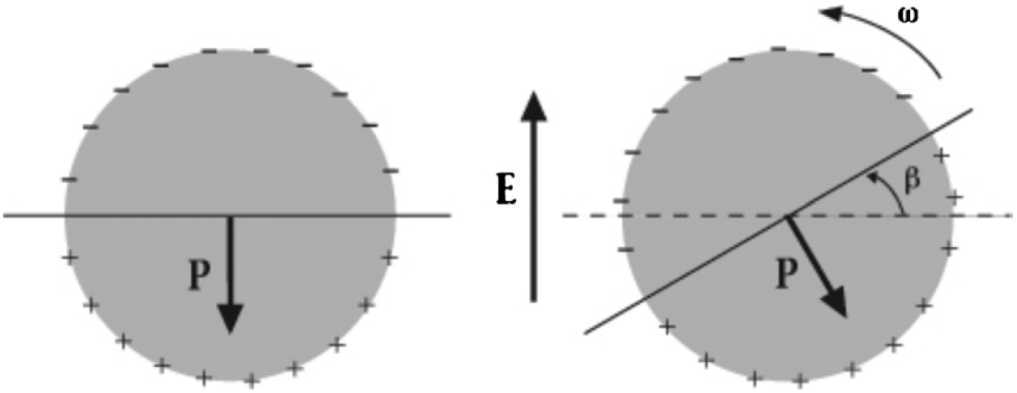

Figure 2.7: Charge distribution in unstable equilibrium for a sphere with $SR < 1$. Above a critical field strength, constant rotation around an axis perpendicular to the electric field is induced by the misaligned dipole moment of the particle (right). The rotation can be either clock- or counterclockwise. Illustration and caption from (Salipante and Vlahovska, 2010).

2.6 Electrorheology

In the previous sections we have examined how a uniform E-field affects a droplet by deforming and rotating it. The next step is to introduce smectite clay particles and investigate how they behave in an applied E-field. We will look at smectite clay particles suspended in silicone oil. Such suspensions are known as electrorheological fluids (ERFs). ERFs are complex fluids that solidify or become very viscous when submitted to an applied electric field. When an external E-field is applied and strong enough (usualy 1 kV/mm), the clay particles become polarized. This phenomenon of polarization has been known since Winslow (1947) first discovered it in 1947. The particles consequently orient in the field and aggregate, which results in the formation of a chain-like structure parallel to the electric field direction (Fossum et al., 2006; Wang et al., 2009; Rozynek et al., 2010). The structuring occurs within seconds, and disappears almost instantly when the field is removed. A microscopic image of the induced chain formation is displayed in figure 2.8.

The internal ordering of the clay particles often leads to dramatic changes in the rheoological properties (viscosity, yield stress, shear modulus, etc.) of the suspensions (Wen et al., 2003). Fossum et al. (2006) investigated silicone oil suspensions with smectite clay particles placed between two copper electrodes. They observed chains parallel to the applied E-field and found a critical electric field necessary to trigger the electrorheological behavior to be $E_c \sim$ 400 V/mm. X-ray studies were also performed during, which they noticed a change in particle platelet separation and where they revealed that the particles align along silica sheets. This former result may indicate that intercalated ions and water molecules play a role in the electric polarization. Using wide angle x-ray (WAX) scattering techniques, Rozynek et al. (2010) observed that the particle orientation occurs very fast with respect to chain formation and aggregation. They also found that the time needed to create columns of aggregated particles decreases as the electric field increases.

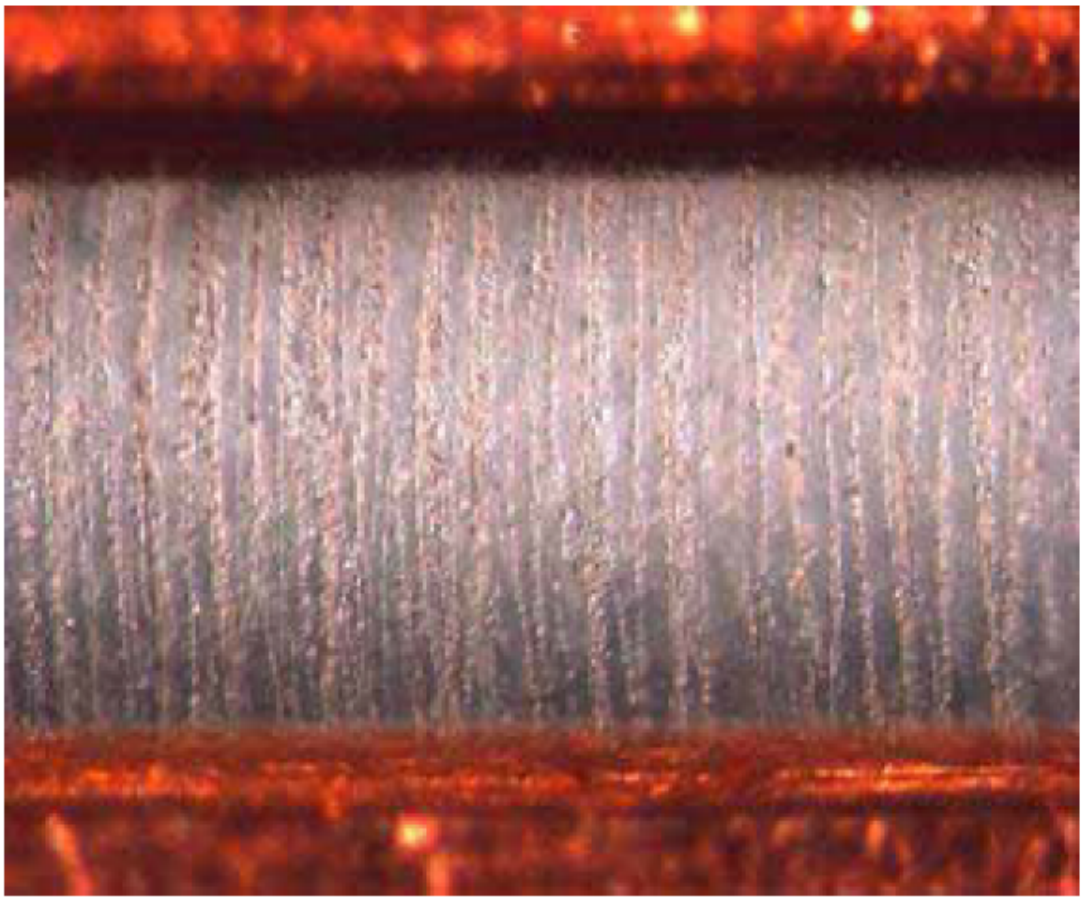

Figure 2.8: Microscope image of electrorheological chain formation in oil suspension of smectite clay particles caused by an applied E-field. Picture from (Fossum et al., 2006).

2.7 Surface tension

How can a razor blade rest on the water surface even when it has a density larger than water? Or why is the water surface in a glass filled completely with water spherical-shaped and above the brink when one instead expects the water to overflow at that point? The answer is a special force on the boundary surface between fluids, namely, the surface tension. Liquids consist of molecules, each of which is surrounded by other molecules with a distance close to the molecule diameter (Lien and Løvhøiden, 2001). Strong, short-ranged and attractive cohesive forces (van Der Waals forces) act between the molecules. The intermolecular forces are illustrated in figure 2.9 a). To remove a molecule from the other molecules, work against these forces has to occur. In the bulk of a liquid (with distance to the surface), the force of cohesion between the molecules is the same in all directions. This is not the case for molecules on the surface. These molecules experience a net force of attraction that pulls them back into the body of the liquid. This is due to the fact that there are more molecules below than above and outside the surface.

Because each of the molecules inside the liquid is bound by the other molecules, these molecules possess a (negative) potential energy. The potential energy increases when one tries to move the molecule outside the liquid, so molecules on the surface have higher potential energy than molecules in the bulk of the liquid. Every system seeks the state with the lowest potential energy. To achieve this, the liquid tries to take the shape that has the biggest possible surface area/volume ratio, namely, the shape of a sphere.

In equilibrium, the surface area of a fluid volume reaches its minimum value. To increase the surface area, work against the molecule forces has to be performed. The surface tension γ is defined as the work per unit required to increase the surface:

$$\gamma = \frac{dW}{dA}. \tag{2.26}$$

This is under the assumption that the temperature is held constant during the work. γ could also be defined as the surface energy of the liquid. Surface tension is typically measured in J/m^2 or N/m.

Imagine a spherical oil drop with radius R surrounded by water. These two fluids are immiscible and the hydrostatic pressure in water p_w and oil p_o are different. The surface tension of the oil drop will minimize the surface area by exerting an inward force on the drop. To prevent the oil drop to collapse, p_w must be lower than p_o. We want to find the relationship between the pressures and the surface tension γ. The surface area of the oil drop is $A = 4\pi R^2$. The force on the oil/water surface due to the pressure difference is then:

$$F = (p_o - p_w)A = (p_o - p_w)4\pi R^2. \tag{2.27}$$

This force is balanced by the surface tension force. If the drop radius increase with an infinitesimal length dR, the surface area of the drop will increase with $dA = 8\pi R dR$. The pressure forces will then exert work against this expansion given by;

$$dW = F dR = (p_o - p_w)4\pi R^2. \tag{2.28}$$

By using equation 2.26 we get:

$$\gamma = \frac{dW}{dA} = \frac{(p_o - p_w)4\pi R^2}{8\pi R dR} = \frac{(p_o - p_w)R}{2} \tag{2.29}$$

Arriving at this equation we assumed a spherical shape. A more general curved shape can be described with two radius of curvature R_1 and R_2. The pressure difference between the two sides of the interface can then be expressed with the Laplace equation:

$$p_c = \Delta p = \gamma(\frac{1}{R_1} + \frac{1}{R_2}). \tag{2.30}$$

The pressure p_c is known as the capillary pressure. The derivation of the equations followed Lien and Løvhøiden (2001).

2.8 Wetting and contact angle

Liquids on a surface will act differently depending on their wettabilities. For instance, an oil and a water drop placed on a horizontal glass plate will not spread equally. The oil drop tends to avoid contact with the glass by contracting, while the water drop "likes" to have more contact and greases itself on the surface. In this sense, water is a wetting liquid regarding glass surface, while the oil is non-wetting. The contact angle is the angle between the tangent to the drop's profile and the surface at the intersection of the solid, liquid or vapor. This angle is used to define and compare the liquid wettabilities on different surfaces. A liquid is wetting if the contact angle is below 90° and non-wetting if it is above 90° (Lien and Løvhøiden, 2001). The contact angle for a wetting and non wetting liquid is displayed in figure 2.9 b) and c).

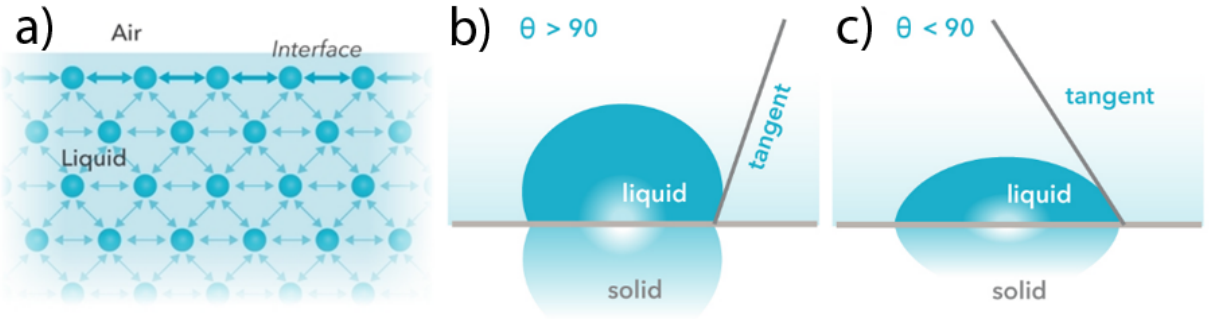

Figure 2.9: Illustration of a) the intermolecular forces in a liquid, b) the contact angle of a non-wetting liquid and c) the contact angle of a wetting liquid. Illustrations from Attension.

2.9 Surfactants

A surfactant is an amphiphilic molecule consisting of a hydrophilic and a hydrophobic part. For most surfactants, the hydrophilic part is an ion forming the "polar head", while the hydrophobic tail is formed by one (or several) aliphatic chains $CH_3(CH_2)_n$. The aliphatic chains try to force water molecules to organize themselves in a entropically unfavorable way. The hydrophobic tail of the surfactant will therefore try to avoid water, while the polar head tries to stay in contact with water (see figure 2.10 A).

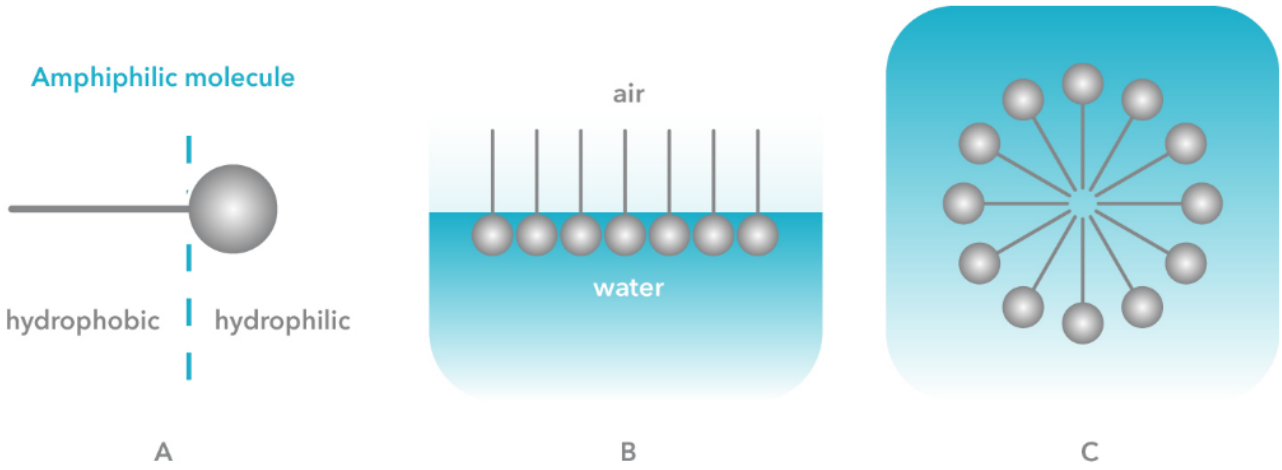

Figure 2.10: Illustration of A) an amphiphilic molecule with a hydrophilic and a hydrophobic part, B) surface active molecules and C) a spherical micelle. The illustrations are adapted from Attension.

By adding a water-soluble surfactant to an aqueous environment, the interfacial tension of the system can be significantly reduced. The hydrophilic head will stay in the water, while the hydrophobic tail of the surfactant stays out of the water at the surface (illustrated in figure 2.10 B). One may think that the surfactant is found primarily at the interfaces, but thermal agitation tends to homogenize the surfactant concentrations and prevent zero bulk concentration. When the surfactant concentration is high enough, the system forms micelles, aggregates typically made up of several hundred surfactant molecules. The structure is formed due to its energetic advantage: the aliphatic tails are protected from the aqueous environment, while only the polar heads are exposed to water (figure 2.10 C).

CMC is the critical micellar concentration. For surfactant concentrations C_s below the CMC, molecules are individually present in the bulk, while for C_s above the CMC, micelles are formed and are in equilibrium with both molecules in the solution and at the interface. The typical influence of a surfactant on the interfacial tension is displayed in figure 2.11. As the surfactant concentration increases, the interfacial tension decreases. This is due to the covering of the interface by a larger number of amphiphilic molecules. This trend continues until the surface is saturated when $C_S = C_{sat}$. The interfacial tension continues to decrease after this, but much more slowly. When the concentration reaches CMC, the interfacial tension saturates at its lowest level. An increase of surfactant concentration will only increase the number of micelles and will not alter the energy of the system.

Adding surfactants will also affect the contact angle. By adding the right type and sufficient amount of surfactant, a system might go from a partial wetting regime to a total wetting regime (as showed in figure 2.9 b and c). For the water-oil system, adding a surfactant considerably diminishes the water/oil γ_{WO} and solid/oil γ_{SO} interfacial tensions. The solid/water γ_{SW} interfacial tension will also decrease, but proportionally less if the used surfactant is less soluble in water. Increasing the surfactant concentration will then decrease the contact angle between the solid and liquid towards zero and detachment. This and other effects are exploited by laundry detergents for washing clothes. Stains adsorbed onto clothings are transformed to drops and detached by detergents and hydrodynamic currents of the washing machine.

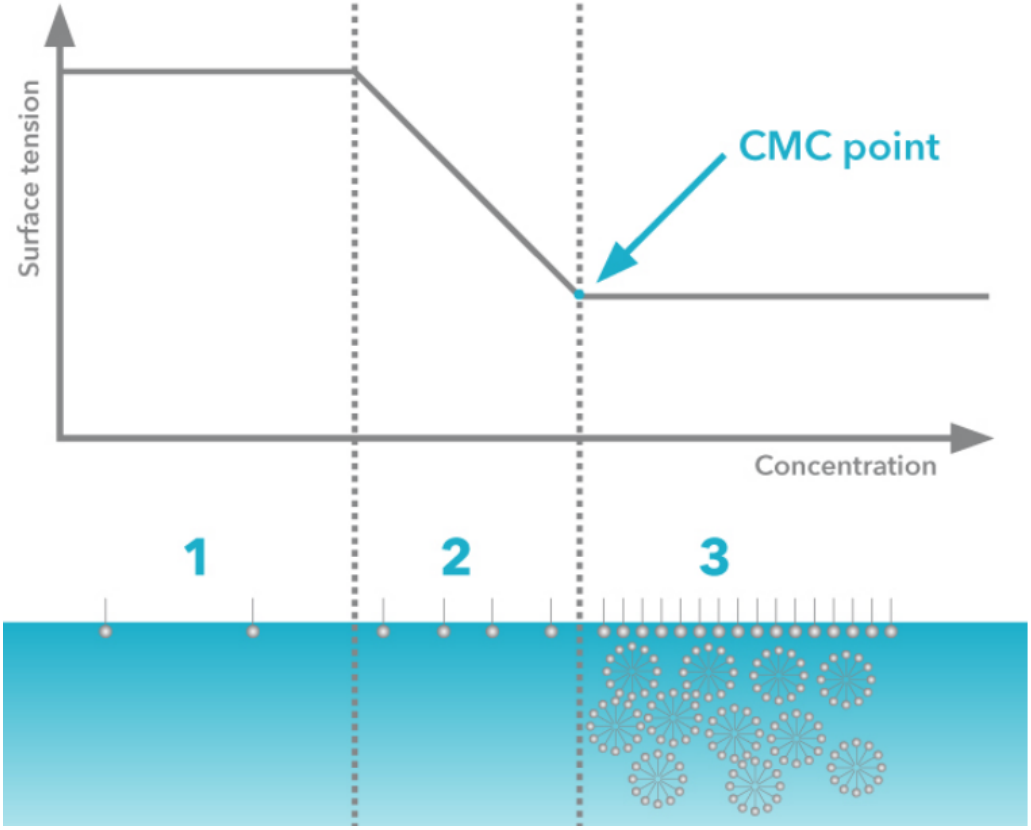

Figure 2.11: A typical graph displaying surface tension (γ) versus log of surfactant concentration added (C_s). The graph shows three phases: 1) at very low C_s, only a slight change in γ is detected. 2) Adding more surfactant decreases γ till 3) surface becomes fully loaded and there is no further change in γ. Graph and captions are adapted from Attension.

When a liquid-liquid system like water-oil is miniaturized, a scaling effect tends to reduce the action of surfactants. Let us look at such a system with a given surfactant concentration C_0. We assume that the surfactant is only found in the water phase (insoluble in oil). The surfactant concentration is given by:

$$C_0 = C_V + C_S \frac{S}{V}, \tag{2.31}$$

where C_V and C_S are the bulk and surface surfactant concentrations, respectively, S is the surface area exposed to water, and V is the water volume. We then have, by order of magnitude;

$$C_S \approx l(C_0 - C_V), \tag{2.32}$$

where l is the scale of the system. This relation implies:

$$C_S < lC_0. \tag{2.33}$$

We see that by decreasing the scale at a fixed C_0, the surfactant surface concentration C_S tends to diminish. The number of surfactant molecules at the interface is less and less, and their action is thus reduced. This effect is not negligible since miniaturization can reduce l by several orders of magnitude (Tabeling, 2005).

2.10 Emulsions

An emulsion is a dispersion of droplets of one liquid (dispersed phase) in another liquid (continuous phase). A mixture of oil droplets in water is known as an oil-in-water emulsion (e.g. milk), while the opposite is a water-in-oil emulsion (butter). For small droplets to form, weak interfacial tensions are necessary. This is because capillary effects favor large drops and will destabilize the emulsion by causing droplets to coalesce. Emulsions are generally stabilized by the use of surfactants. The emulsions can be distinguished by the size of the droplets: emulsion systems with droplets larger than a micrometer are called macro-emulsions, while micro-emulsions are made from submicrometric micelles. Macro-emulsions are in a metastable state since phase separation (for example milk to cream) is energetically favorable. Because micelles do not gain energy by coalescing, micro-emulsions are stable (Tabeling, 2005).

Solid particles dissolved in one phase can also stabilize emulsions (Binks, 2002). This is known as pickering emulsion. The solid particles adsorbs at the oil water interface, thereby creating a physical barrier that hinders coalescence. Clay minerals are known to produce very stable pickering emulsions (Binks, 2002; Ashby and Binks, 2000). The droplets have to be covered by at least one mono layer of clay, otherwise they coalesce (Yan and Masliyah, 1994).

2.11 Flow in oil reservoirs

To extract oil and gas from oil reservoirs in an efficient manner, a basic understanding of the dynamic liquid flow is crucial. In these reservoirs, oil and gas are stored in small pores with diameters ranging from 10 to 100 μm. The volume flow q_V through a surface A in such a porous medium is expressed with Darcy's equation

$$q_V = -\frac{k \cdot A\Delta p}{\eta}, \tag{2.34}$$

where k is the permeability of the rock type, Δp is the pressure difference in the flow direction and η is the viscosity coefficient. This equation describes the average flow through pores with different sizes. The equation is only valid for one phase flow. For two immiscible fluids flowing through the pores at the same time, like water and oil, the equation has to be adjusted. The water tends to wet the pore walls, while the oil stays away in the middle. Capillary pressure occurs due to surface tension forces, and the presence of one fluid will affect the other. The relative permeability k_r is an empirical function describing how well a liquid is flowing in pores with the presence of another liquid as compared to the flow if it was alone. Darcy's equation for oil and water is then:

$$q_i = -\frac{k \cdot k_{ri} \cdot A\Delta p}{\eta_i}, \tag{2.35}$$

where i = 1,2 for water and oil, respectively. Typical relative permeabilities are presented in figure 2.12.

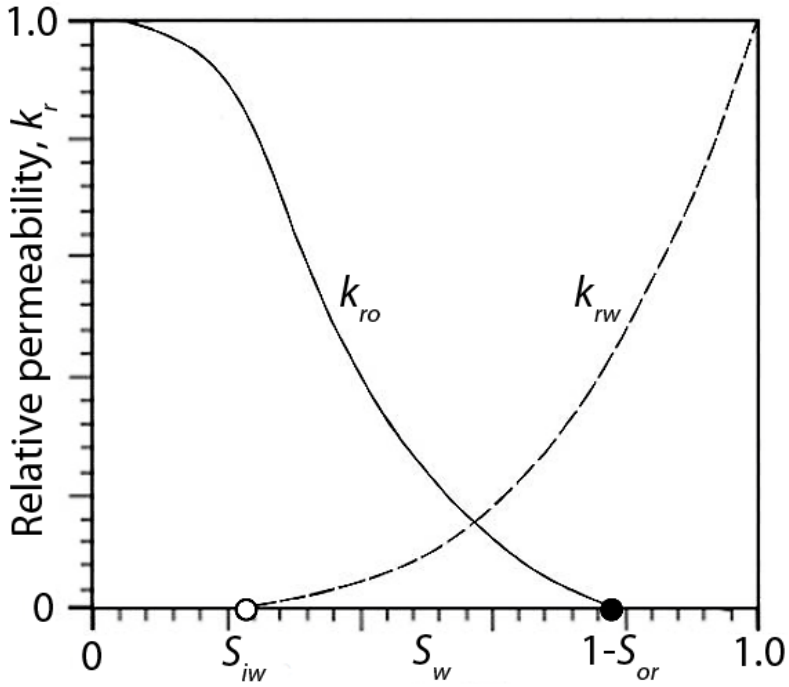

Figure 2.12: Typical relative permeabilities for oil k_{ro} and water k_{rw} against liquid saturation S_w. Figure adapted from Lien and Løvhøiden (2001).

S is the liquid saturation. K_{ri} equals zero when S_i is below approximately 20%[1]. This is since small pockets of liquids form at small liquid saturations and are separated from the rest. In other words, it is not possible to empty an oil reservoir below 20% of the remaining oil saturation[2]. Water with high pressure is used to extract oil from the reservoirs. The number of possible ways for the water to move through the pores is infinite. Oil in the biggest pores will be pushed out first since the capillary pressure increases with a decrease in droplet radius (equation 2.30).

To extract as much oil from the reservoirs as possible, a balance between the capillary forces and external forces has to be found. The oil flow can also be improved by decreasing the viscosity of the oil or increasing the viscosity of water. Other methods include changing the oil drop sizes and surface tension. The T-junction we will use in the flow experiments is a good model for the water and oil drop formation in the pores. Finding a way to control the droplet volume/length can increase the oil extraction and increase profits by millions of dollars (Lien and Løvhøiden, 2001).

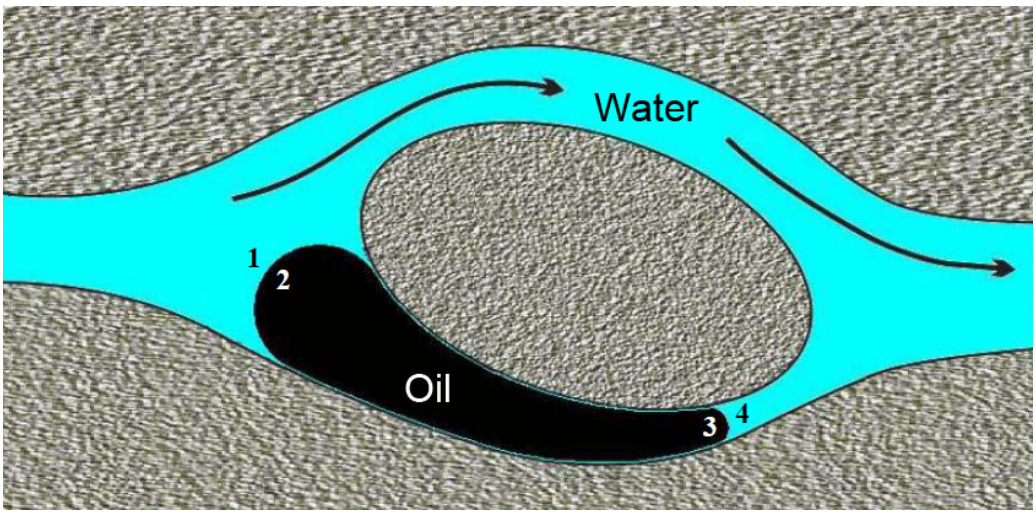

Figure 2.13: Illustration of an oil drop trapped in a pore in the presence of a pressure gradient generated by the water flow in the porous medium. Illustration adapted from Baviere (1991).

Figure 2.13 illustrates a situation that could happen in an oil reservoir wetted by water. There are two parallel pores where one of the pores contains trapped oil. One sees that the 1-2 interface is larger than the 3-4 interface. By using equation 2.30 and by asuming equal water pressure on both sides of the oil, the capillary pressure $p_{c12} < p_{c34}$ and the oil drop moves to the left and stays trapped. To drive the oil drop to the right and out of the pore, a water pressure gradient Δp must exist and satisfy: $\Delta p/2\sigma > (1/R_{34}) - (1/R_{12})$. As mentioned in the paragraphs above, the size of the water pressure gradient is controlled by adjusting the parameters in equation 2.35.

[1]This value depends on parameters like the fluids and wettabilities of the rock type.

[2]However, if water and oil can be mixed and flow together as one liquid, all the oil can be extracted. This is possible if the surface tension between water and oil is removed by adding surfactants. These surfactants are in most cases too expensive for the method to be profitable.

2.12 Two phase microfluidic flow

Three categories of parameters control the properties of two-phase flow in microchannels; the channel geometry, flow conditions and the properties of the two fluids. Important dimensionless numbers are used to describe these factors. The first dimensionless number worth mentioning is the Reynolds number (Re). It describes the importance of inertial forces relative to viscous forces and is given by:

$$Re = \frac{\rho d u}{\mu}, \tag{2.36}$$

where ρ is fluid density (kg/m^3), d is a characteristic length scale (m), u is the characteristic velocity (m/s) and μ is the dynamic viscosity (Pa $\cdot$ s). When considering micro scales, the Reynolds number is much smaller than 1. The small number indicates that for microchannel flows, the inertial force is dominated by the viscous force. The Bond number (Bo) is another dimensionless number. It compares the importance of gravitational forces relative to interracial forces:

$$Bo = \frac{\Delta\rho g d^2}{\sigma}, \tag{2.37}$$

where $\Delta\rho$ is the fluid density difference (kg/m^3), g is the gravitational acceleration (m/s^2) and σ is the interfacial tension between the two fluids in contact (N/m). As the Reynolds number, the Bond number is much smaller than 1 at micro scales. Gravitational forces are thus dominated and insignificant relative to surface forces.

The relative effect of viscous forces to interfacial tension forces is given by the Capillary number (Ca), an important parameter in microfluidics;

$$Ca = \frac{\mu u}{\sigma}. \tag{2.38}$$

Other dimensionless numbers worth mentioning are the Ohnesorge number (Oh) and the Weber number (We). The Oh number compares viscous force to inertial and interfacial tension forces, while the We relates inertial effects to surface tension (Zhao and Middelberg, 2011):

$$Oh = (\frac{Ca}{Re})^{1/2} = \frac{\mu}{(\rho d\sigma)^{1/2}}, \tag{2.39}$$

$$We = Re \cdot Ca = \frac{\rho u^2 d}{\sigma}. \tag{2.40}$$

2.12.1 Droplet formation regimes in T-junction

The flow experiments presented later in the experimental and method chapters are performed in a microfluidic T-junction. Cross-flowing mode is used with the continuous phase (dist. water with or without clays) introduced from the vertical channel of the T-junction while the disperse phase (oil) flows through the perpendicular channel (see figure 2.14). Short spherical droplets and longer "plug" droplets are two kinds of patterns produced in the T-junction. As will be discussed in more detail later, the plug length is found to decrease with the flow rate ratio of the continuous phase to the dispersed phase (Q_c/Q_d), together with the total flow rate.

Tice et al. (2004) observed three droplet formation regimes when changing the flow rate. With low flow rates and capillary number Ca between 7.0×10^{-4} and 7.6×10^{-2}, droplet plugs are sheared off right at the T-junction. The sharp breakup is due to the domination of the interfacial tension force pronounced at low flow rates. By increasing the flow rates and Ca number (to between 1.9×10^{-3} and 8.2×10^{-2}), the disperse phase flows a bit into the horizontal channel and forms a long neck before plugs are sheared off. Even longer necks are formed, but the plug size becomes smaller when the flow rates and Ca increase further ($2.2 \times 10^{-2} \leq Ca \leq 1.1 \times 10^{-1}$). The relative viscous force becomes more dominant when the flow rate increases and the interfacial tension force is no longer sufficient for sharp plug breakups. This allows a laminar flow of the disperse phase in the horizontal channel before the shear-off takes place (Tice et al., 2004). The three regimes presented are named as squeezing, dripping and jetting. They have also been confirmed by a numerically study of droplet formation in T-junction microchannels (De Menech et al., 2008).

2.13 Droplet formation mechanism

Understanding the droplet formation mechanism is crucial to control and adjust the behavior of the flow pattern. One approach, taken by Thorsen et al. (2001) and Tan et al. (2004), analyzed the forces involved in the droplet formation process. Channel geometry, structure and properties (channel type, dimension and hydrophobicity), fluid properties (density, viscosity, interfacial tension and contact angle) and operating parameters (pressure, flow rate ratio, temperature, electric fields, etc.) are all variables affecting the dynamics of droplet formation. Several dimensionless parameters are used to express these variables. As already mentioned, depending on the parameters, some variables are more dominant than others. Working on a micrometer scale, the effect of gravity and inertia can typically be ignored. Thus, for our experiments, the capillary number Ca becomes the most important dimensionless parameter. Ca distinguishes the three droplet formation regimes that have been defined: squeezing, dripping and jetting. Our experiments have been performed with low Ca numbers, so only the squeezing regime will be relevant in this context.

In the squeezing regime, the capillary number is typically less than 0.01. When this is fulfilled, the interfacial force dominates the shear stress and droplet breakup is governed by the hydrostatic pressure drop across the emerging droplet in the T-junction. As the dispersed fluid fills the main channel (figure 2.14 a and b), a growing interface between the phases occurs. As this interface grows and deforms, it will expel the continuous fluid around itself and induce extra pressure (Laplace pressure).

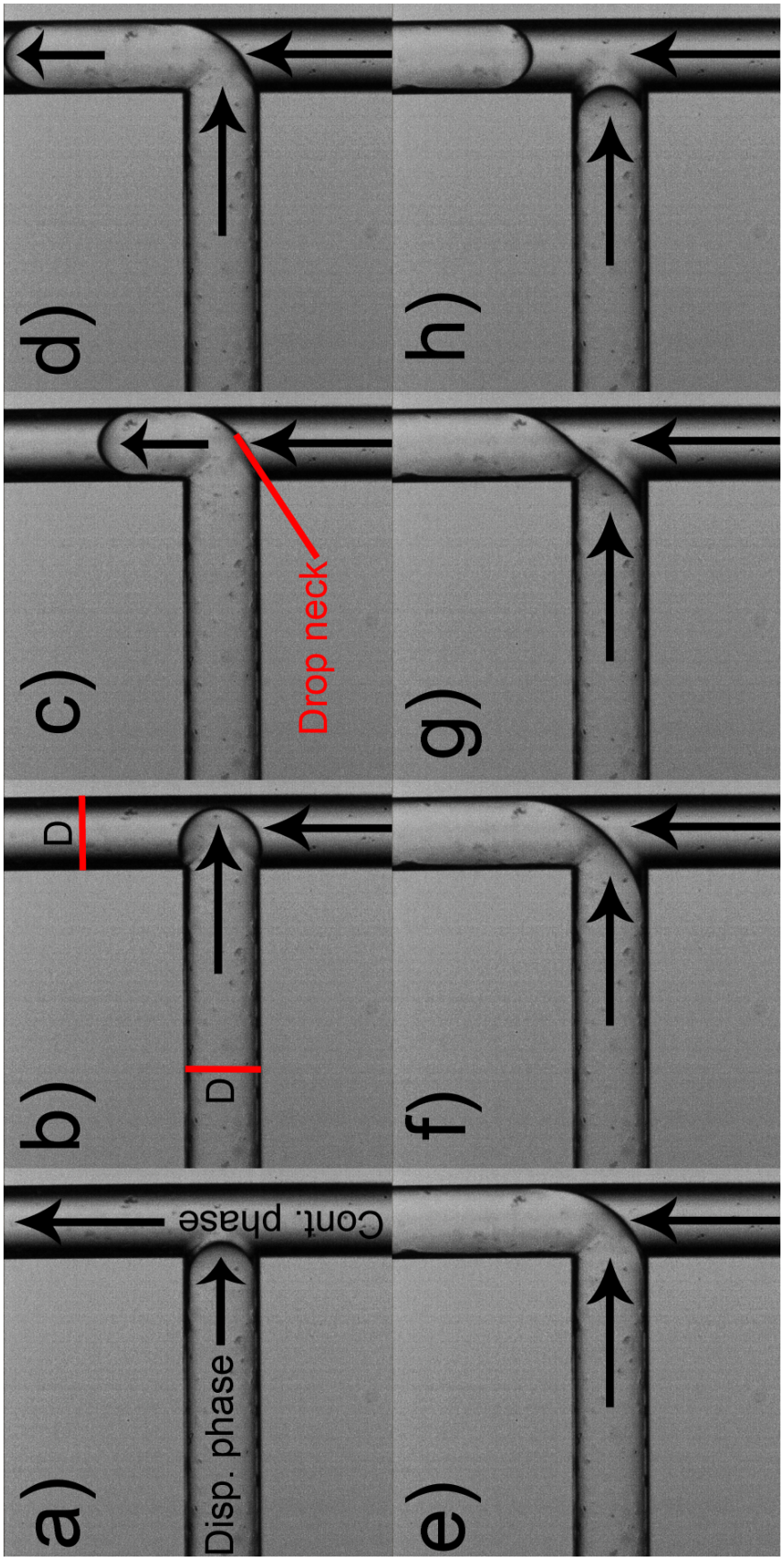

Figure 2.14: a) - h) Pictures of the droplet/plug formation in a microchannel T-junction. Disperse phase (dist. water w. 1.5% Na-Fh) is introduced from the horizontal channel while the continous phase (OP3 mineral oil) flows in the vertical channel. The flow rate ratio $Q_c/Q_d = 1$ and the microchannel diameter $D = 110$ μm.

Li et al. (2012) observed local velocity and pressure fluctuations during a droplet formation period and found that the fluctuations decrease in amplitude when the continuous phase velocity increases. They also observed inner droplet circulation motion caused by shearing on the interface and Laplace pressure. This motion verifies that the pressure inside a droplet is dynamic. The local pressure near the T-junction inlet increases as the droplet forms. It reaches a summit right before the drop reaches the wall (figure 2.14 b). The pressure in the continuous flow is then higher than the resistance pressure (in the dispersed phase, Laplace pressure). As found in equation 2.30, the Laplace pressure decreases when the curvature of the drop increases. The droplet travels downstream and the droplet neck decreases until it breaks (figure 2.14 c - g). The tip of the neck recoils to the inlet channel of the dispersed phase and the pressure in the continuous phase drops to its unperturbed value. This droplet formation mechanism is known as "rate-of-flow-controlled" breakup (Garstecki et al., 2005, 2006). Garstecki et al. (2006) proposed a scaling law to model the squeezing regime. This scaling law was later modified by Xu et al. (2008) and verified numerically by De Menech et al. (2008). The scaling law indicates that in the squeezing regime, the droplet size decreases with an increase in Ca and is almost independent of fluids properties:

$$L/w = \epsilon + \delta \frac{Q_d}{Q_c}, \tag{2.41}$$

where L is the droplet length, w is the width of the channel, ϵ and δ are fitting parameters depending on the geometry of the T-junction, while Q_d and Q_c are the flow rate of the dispersed and continuous phase, respectively.

2.13.1 Interfacial effects on flow patterns

There are two interfaces in microfluidic two phase flows: fluid - fluid and fluid - wall. As seen in section 2.12, interfacial effects become dominant and important when working with micrometer scales. In determining whether ordered or disordered flow patterns occur, the wetting properties of the fluid-wall interface is crucial (Dreyfus et al., 2003). The hydrophobicity or hydrophilicity property of a solid surface is also found to be important. The wall properties can me expressed quantitatively by contact angles. It is found that ordered flow patterns can only be observed for fluids making contact angles larger than 90° (Xu et al., 2006c) with the channel wall. For contact angles beneath this, only disordered flow patterns can be observed. However, the contact angle can be changed by adding surfactants at different concentrations (Xu et al., 2006a).

2.13.2 Viscosity effect on droplet formation

Tice et al. (2004) studied both low($\mu = 2.0$ mPa·s) and high ($\mu = 18$ mPa·s) viscous continuous and dispersed phases. They found that all the four combinations of low and high viscosity for the dispersed and continuous phases produced regular plugs in T-junction microchannels. The manner in which viscosity affects the droplet size is not straightforward. It depends on channel geometries and properties, among other factors. Kobayashi et al. (2005) found that in straight-through microchannels, the dispersed phase viscosity η_d and not the oil type had an influence on the droplet size. A viscosity threshold value exists which governs the viscosity and droplet size relationship. Under the threshold value, the droplet size decreases with increasing viscosity, while when the viscosity η_d is above the threshold value, the droplet size slightly

increase with η_d. It is generally easier to compare the interactions between different properties with dimensionless numbers than look at each property alone. The influence of viscosities on droplet formation can thus be read from the capillary number.

2.13.3 Surfactant effect

When working with flows at the micrometer scale, the large surface area to volume ratio makes surface effects more salient. However, at the same time, the action of the surfactants are reduced due to the scaling effect (eq. 2.33). Adding surfactants to the dispersed or continuous phase is often needed to stabilize the droplet formation (with regards to droplet size and spacing). Studies show that use of surfactants in the dispersed phase in T-junction droplet formation experiments decreases the interfacial tension between the liquids and thus the droplet diameter compared to systems without surfactants (van der Graaf et al., 2005; Campos, 2011). When the interfacial tension between the disperse and continuous phase is decreased, the flow resistant pressure in the droplet is smaller and its ability to withstand the pressure from the continuous phase is impaired. The drop neck will thus break faster and less disperse phase will flow into the main channel before the droplet form and flow downstream.

It is also found that increasing the surfactant concentration in the continuous phase results in smaller droplet sizes. The influence of surfactants in droplet formation is complex. Surfactants can reduce the equilibrium interfacial tension, but they may also exert dynamic effects by altering interfacial rheology and introduce dynamic interfacial tension effects (Schroder et al., 1998; van der Graaf et al., 2004). The mentioned effects affect droplet formation in a complex way that is not yet fully understood. It is observed that dynamic interfacial tension between two liquid phases is neither constant nor uniform and becomes more significant at low surfactant concentrations (Sugiura et al., 2004).

2.13.4 Geometry effect

The scaling law presented in section 2.13 is based on a T-junction having microchannels with rectangular cross sections. For this geometry, there will be four "open" gutters and a thin film above the droplet where continuous fluid flows around the moving droplet (see figure 2.15). Micro particle image velocimetry (μ-PIV) experiments show that for a quadratic cross section microchannel, at least 25% of the continuous fluid volume leaks through the four gutters before droplet detachment (van Steijn et al., 2007). In the squeezing regime, such leakage leads to a flow reversal that dominates the droplet detachment process. For oval cross section microchannels, as used in our experiments, this leakage is minimal. This results in an increase in the pressure exerted by the continuous phase on the drop and less time for the disperse phase to fill the microchannel. A T-junction having microchannels with circular geometry is thus expected to produce shorter droplets than a T-junction with rectangular microchannels.

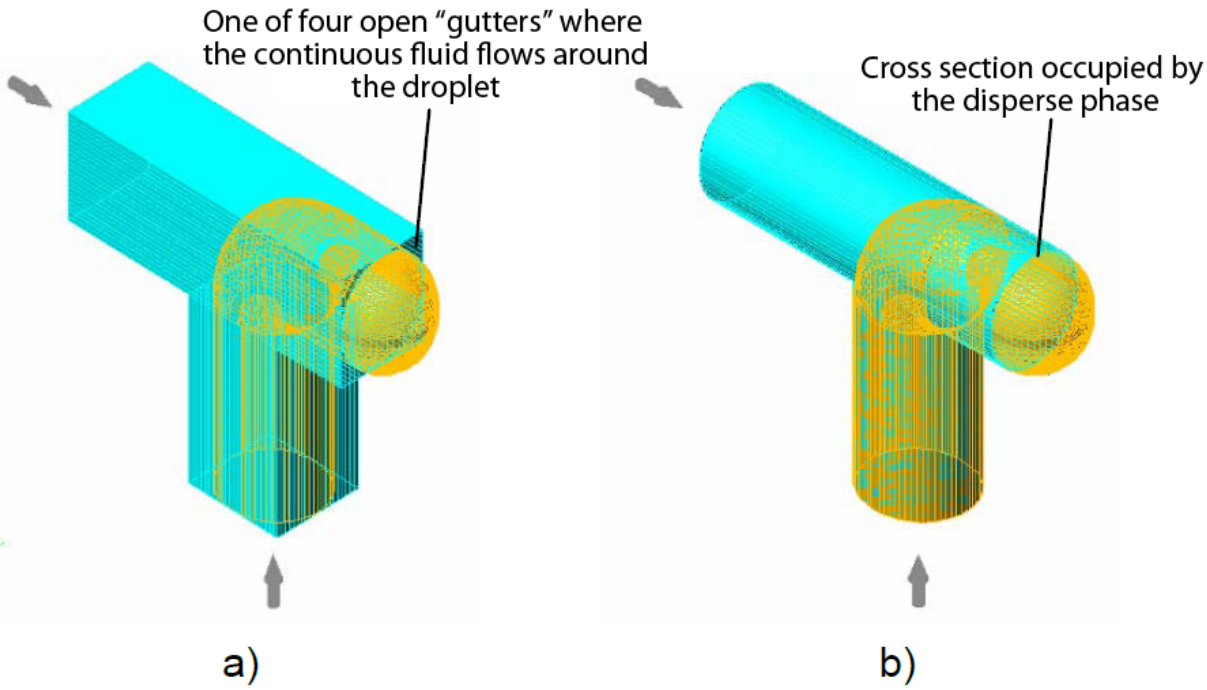

Figure 2.15: The difference between a) a rectangular- and b) an oval microfluid T-junction. The spheric shape of the formed droplet in a rectangular microfluid T-junction allows some of the continuous fluid to flow around the droplet through four open gutters. This is not the case for the oval microfluid T-junction where there is practically no available space around the formed droplet. Illustrations adapted from Campos (2011).

Chapter 3

Experimental set up

3.1 E-field induced clay pattern in droplet

Figure 3.1 displays the experimental setup for the E-field induced clay pattern in droplet experiments. The setup consists of three systems: The electric, the sample cell and the image acquisition system.

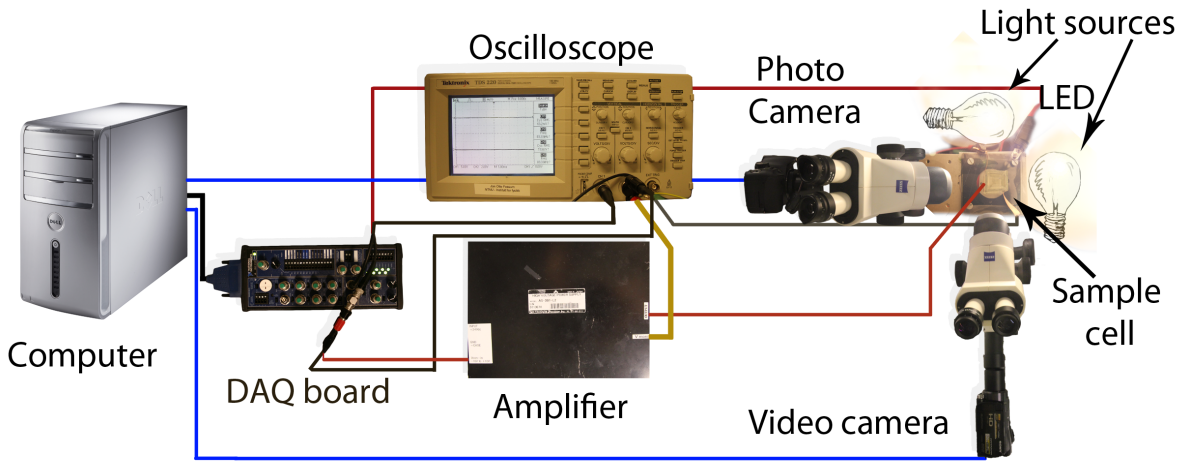

Figure 3.1: Experimental setup: Droplets with clay in E-field.

3.1.1 Electric system

With a MATLAB (a numerical computing environment) script and a DAQ (data acquisition) card, a computer is used to generate a signal between -10 and 10 V, at a specific frequency. This signal can be either a direct current (DC) signal or an alternating current (AC) square wave. The generated signal is monitored by an oscilloscope in addition to being amplified 300 times by an amplifier. From the high voltage amplifier, the signal continues to the sample cell via cables and conducting tape. Measurements of the amplification is made possible by connecting the amplifier monitor output to the oscilloscope (figure 3.1).

3.1.2 Sample cell

The custom-made sample cell (with measurements) is presented in figure 3.2. It consists of three glass sides and two transparent conducting sides made of ITO (Indium Tin Oxide). The sample cell has a cubic-cuvette form where the top part is open for samples to be poured in. The conducting sides are placed on the outside of the cell and separated by a gap equal to 12 mm. Conducting tape and crocodile clips are used to conduct the current from the amplifier to the cell. An adjustable stage is used to adjust the height of the sample cell, while movements in other directions are controlled by moving the whole stage.

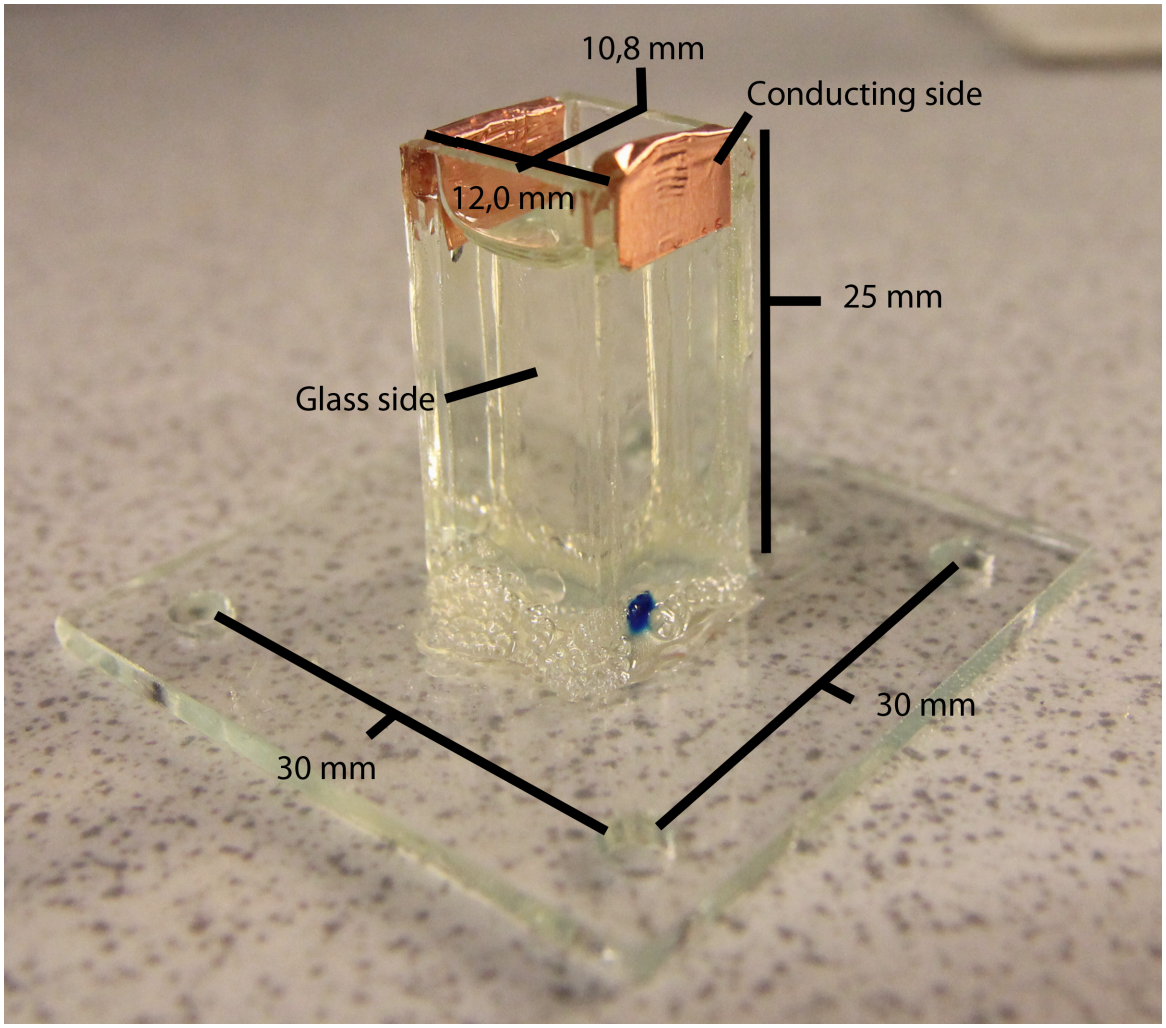

Figure 3.2: The custom-made sample cell.

3.1.3 Acquisition

To view the small clay particles inside the sample cell, two microscopes together with two light sources are used. A Sony video camera and a Canon photo camera are attached to the microscopes with optical paths normal to one another. This configuration allows for simultaneous observations of the droplet behavior from both a front view (optical path perpendicular to E-field direction) and a side view (optical path parallel to E-field direction). The focus is set to

manual on the cameras and white balance together with exposure can be adjusted to enhance the light and detail in captured images. Both for security reasons and also to help visualize when the applied electric field is turned on or off, a red LED is used (figure 3.1). It is connected to the DAQ, programmed in MATLAB and placed in the corner of the sample cell to shine a red light on the droplets when the electrical field is turned on.

3.1.4 Oils

Silicone oil (100 cSt from Dow Corning 200) with different Na-Fh clay concentrations was used to make droplets, while castor oil (Fluka 93912 delivered by Sigma-Aldrich Norway AS) was used as the suspending liquid. Both oils are immiscible with each other, relatively non-polar and have similar densities. Castor oil has approximately 10 times higher conductivity than silicone oil. This feature is favorable since it makes it easier to fullfill the requirements for Quincke rotation (section 2.5), which with clay particles may be interesting to study.

The castor oil is well suited as a suspending liquid with its high viscosity, which results in a low silicone droplet settling velocity. This is important since the fluid motion caused by gravity is then negligible compared to the electrically induced fluid flow. The decrease in droplet settling velocity also eases the image capturing and allows the droplet to fill a larger part the image. Table 3.1 presents the density, viscosity, conductivity and dielectric constant values for the oils.

Table 3.1: Manufactured density (ρ) and dynamic viscosity (μ) values at 25 °C and measured conductivity (σ) and dielectric constant (ϵ) values for the silicone and castor oil. * The conductivity value of 100 cSt silicone oil has been estimated.

Oil	ρ (kg/l)	μ (Pa·s)	σ (pS/m)	ϵ
100 cSt Silicone Oil	0.965	0.965	$\sim$ 3-5*	2.13
Castor Oil	0.961	0.65	45	3.37

Conductivity and dielectric constant values have been measured by Hersvik (2010). Hersvik was not able to measure the conductivity for the 100 cSt silicone oil, but it is reasonable to assume that its value lies in the 10 cSt silicone oil conductivity regime. The viscosity is the only property that parts the two oils and the 10 cSt silicone oil conductivity scales with the applied E-field (displaying a non-ohmic nature). The conductivity measures for the 10 cSt silicone oil were 3 and 5 pS/m for an applied E-field equal to 150 and 300 V/mm, respectively.[1]

[1] In their experiments, Salipante and Vlahovska (2010) measured the conductivity value of 100 cSt silicone oil to be 1.23 pS/m.

3.2 Microfluidic flow system

The experimental set up for the microfluidic flow experiments consists of an injection system, micro capillary and acquisition devices. The set up is displayed in figure 3.3.

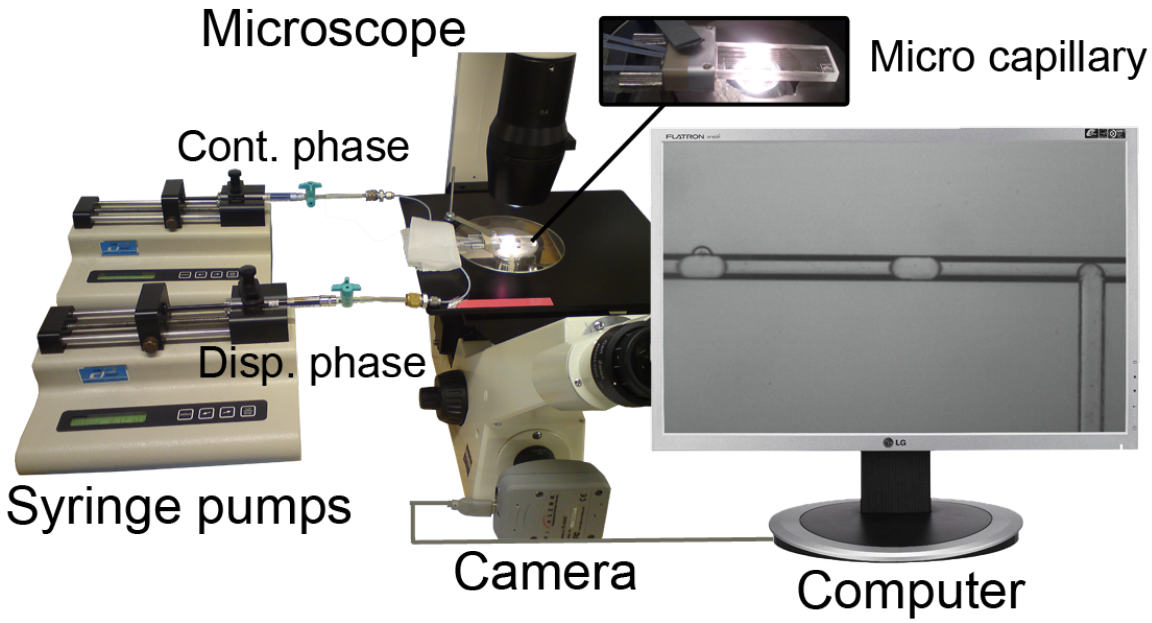

Figure 3.3: Experimental setup: Microfluidic flow system.

3.2.1 Injection system

The injection system consists of two syringes, two syringe pumps, a micro-capillary and accessories used for mounting the circuit. The fluids are injected with two *COLEPALMER 78-0100C* syringe pumps. The pumps have stepper motors where the gears can be controlled by a microprocessor, which provides volumetric injection rates with ± 0.5% accuracy and ± 0.2% reproducibility of measurements (Colepalmer). The minimum flow injection supplied by the pumps is 0.01 ml/hr.

Two glass syringes (figure 3.4a) containing 10 ml are connected to the micro-capillary via a three-way *Embramed* plastic tap and plastic/rubber tubes (figure 3.4b). The syringes have a metal plunger tip coated with teflon which ensures dimensional stability and does not allow leakage of liquid or gas even at high pressures (up to 200 psi). A "luer lock" connection gives a tight connection between the three-way *Embramed* plastic tap and syringes/pipes. The connections and tubes between the syringes and micro-capillary are designed to contain the smallest number of elements and volume. With this design, the work done by the pumps is accelerated and the system is as strict as as possible to minimize the risk of leaks and transition effects due to deformation of the tubes.

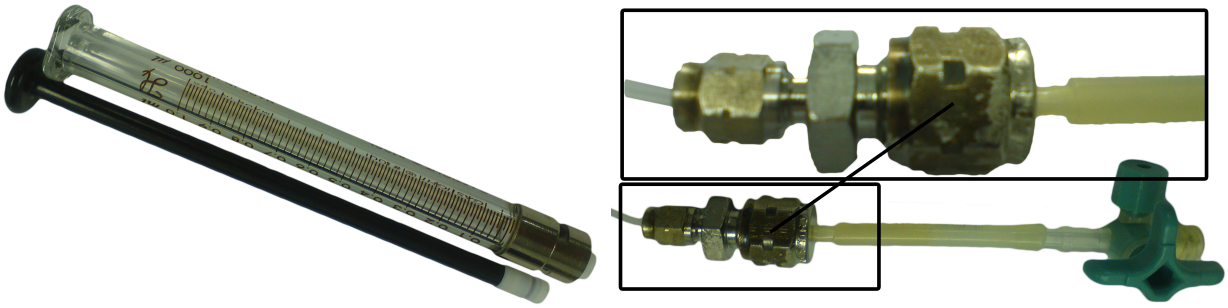

(a) Hamilton Gastight 1000 syringe. (b) *Embramed* plastic tap with tubes and connections.

Figure 3.4: Syringe and plastic tap.

3.2.2 Micro capillary

The capillary used for the flow experiments is a microfluidic T-junction (The Dolomite Centre Ltd, UK). The T-junction microchannel geometry is well suitable and often used to make and control droplets/plugs with high precision (Nissiako et al., 2002; van der Graaf et al., 2005; Xu et al., 2006b; Garstecki et al., 2006). It is made of glass and designed for a wide range of applications, including fluid mixing, micro-droplet formation and reactions. The capillary has high visibility and excellent chemical compatibility. Its surface is extremely smooth and it can function in a wide temperature and pressure range. According to the information sheet from the manufacturer (The Dolomite Centre), the device has been made by hydrofluoric acid (HF) etching and thermal bonding. The geometry of the channels presents an oval cross-section with the same size throughout the whole length of the channels. Figure 3.5 shows the microfluidic device and some of its features.

3.2.3 Acquisition system

The acquisition system consist of a Axiovert 40MAT (Carl Zeiss) optical microscope with adjustable light. The microscope has five different lenses (2.5×, 5×, 10×, 20× and 50×) that can be used. A PixeLink PL-A662 camera is connected to the microscope and a computer. This setup allows a live view on the computer so that one can observe exactly the same on the computer screen as through the microscope. For the analysis, the AxioVision software developed by Carl Zeiss is used. This software is well suited for capturing and processing pictures and videos. It also has tools for manual and automatic measurements of parameters like distances, diameters and areas.

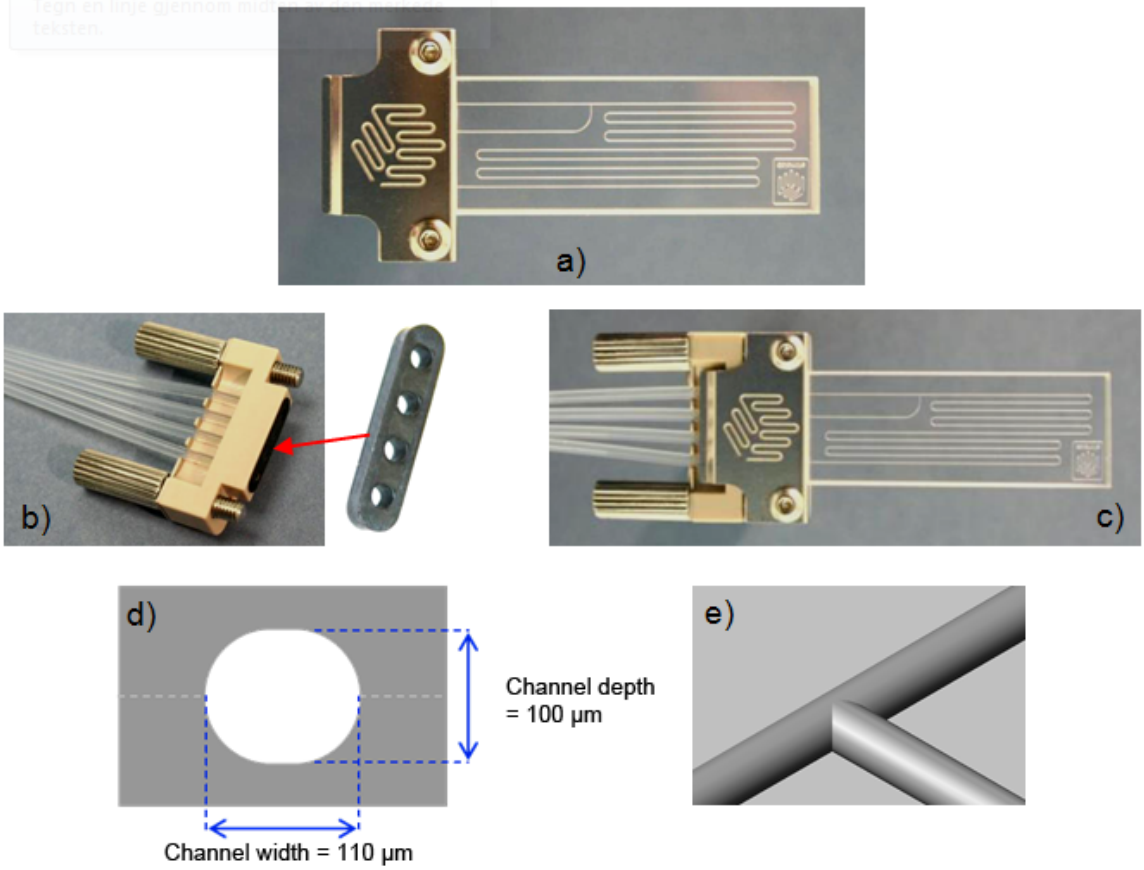

Figure 3.5: Image of a) Microfluidic T-junction, b) connector and seal, c) microfluidic chip mounted with tubes, d) channel cross-section profile and e) 3D image of T-junction. Images are adapted from The Dolomite Centre.

3.2.4 Fluids and clay

OP3 mineral oil and distilled water with and without clay particles are used in the flow experiments. The OP3 mineral oil was chosen because it has low viscosity at room temperature, is insoluble in water, is well known as a standard for calibrating instruments and also because Campos (2011) used this oil for similar experiments. In addition, the oil is colorless, odorless and soluble in most organic solvents. At room temperature (23 °C), the viscosity of the oil and water equals 3.40 and 0.94 mPa·s, respectively, while the superficial surface tension against air equals 22.0 and 72.3 mN/m (Campos, 2011). For this experiment, three different clay types are used: sodium fluorohectorite (Na-Fh), bentonite and laponite. The clay particles are described in more detail in section 2.1.

Chapter 4

Methods

4.1 E-field induced clay pattern in droplet experiments

Initially silicone oil with different Na-Fh clay concentrations was weighted and mixed together. The samples were then ultrasonicated between five and ten minutes to prevent clay particle aggregation and formation at the sample container bottom. Castor oil was poured inside the sample cell with a pipette. The samples were well shaken before a small drop was made using a high performance pipettor (accuracy $\pm$ 0.1 μL) and applied in the center and top of the sample cell (figure 4.1). To minimize measurement errors, it is important to make the drop without air bubbles and away from the sample cell walls.

Figure 4.1: High performance pipettor used to make droplets.

Further, the sample cell and microscopes were adjusted to improve the contrast and to place the drop in the center and top of the image. Both focus and magnification were set to let the drop fill about 1/4 of the viewed image. Exposure and white balance were also adjusted before an optimized image of the drop was seen in both cameras. Depending on the experiment, the cameras (photo and video) were set to either photo or movie mode before recording was initiated. After a few seconds and by using the *MATLAB* script, an electric field was applied across the electrodes.

During the experiments, the generated signal before and after amplification was measured with an oscilloscope. The electric field (E-field) was applied for a certain time and the focus and sample cell position were adjusted continually. These adjustments were necessary to keep the drop in focus and inside the captured image. Affected by the E-field and gravity, the drop moved both sideways and down. After the applied E-field was turned off, the cameras captured

images for some additional seconds. The instruments were then readjusted and a new droplet was made for the next experiment. Several experiments were performed in the same fashion and with different clay concentrations and/or E-fields. The time after the drop is made and to the E-field is applied is critical. A long break will result in clay aggregation in the bottom of the drop and the drop will slowly sink towards the bottom of the sample cell.

Some of the captured video files were imported in the video editing program *Adobe Premiere Pro CS5* where selected frames were saved. The frames were then edited in *Adobe Photoshop Lightroom 3* (photo editing program) where the contrast, sharpness and exposure were adjusted to enhance the clay particle details. A before and after picture comparison is shown in figure 4.2.

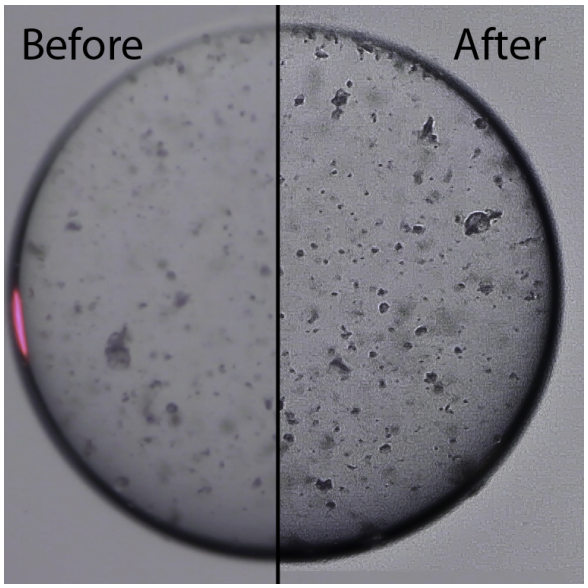

Figure 4.2: Comparison of image before and after editing.

4.2 Sample preparation

If the clay grains were big and lumpy, pestle and mortar were used to pulverize the clay. The weight of the liquid (oil or water) and clay were then measured separately before they were stirred together by a magnetic stirrer between half an hour to half a day depending on the clay, liquid and clay concentration. To prevent aggregation and big clay particles in the samples, the samples were ultrasonicated for at least 5 minutes. Ultrasonicating or shaking/stirring the samples is especially important to do right before using the samples since the clay particles sinks towards the bottom of the container and result in a non-uniform clay distribution.

4.3 Ring method

The Du Noüy ring method was used to measure superficial surface tension (SST) for different samples. In this method, a ring is immersed into the liquid and slowly lifted out through the surface. A lamella is formed (figure 4.5 b) and stretched to its maximum as the ring rises (figure 4.4, image 5-8). The maximum force is measured right before the lamella breaks and used to calculate the surface tension. The ring immersion depth and level to which it is raised right before the lamella breaks are irrelevant to this technique.

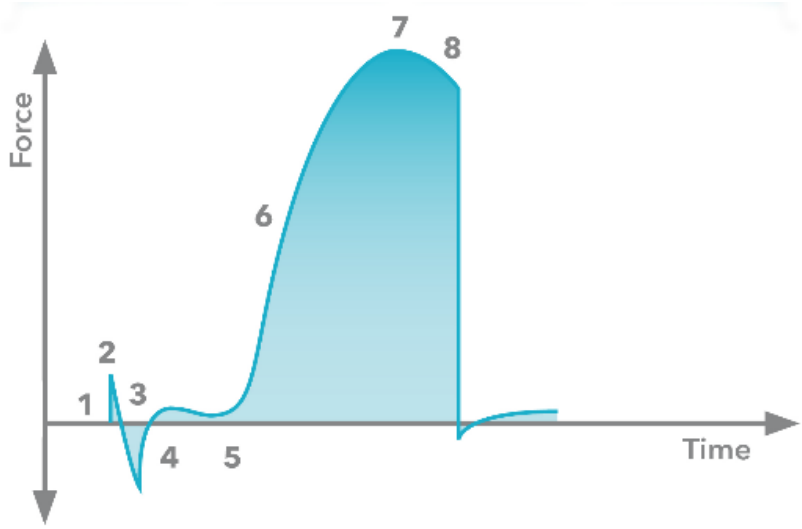

Figure 4.3: (1) The ring is above the surface and the force is zero before (2) it hits the surface. There is a slight positive force due to the adhesive force between ring and surface. (3) The force is negative since the ring must be pushed through the surface.(4) The ring breaks through the surface and a small positive force is measured due to the supporting wires of the ring. (5) The ring is lifted through the surface and the the measured force starts to increase. (6) The force keeps increasing until (7) the maximum force is reached. (8) After the maximum is reached, there is a small force decrease until the lamella breaks. Illustrations and caption adapted from Attension.

SST measurements of the samples were performed with a LAUDA VO 2001 tensiometer (figure 4.5 a) at 20 °C in the characterization of fluids lab (LCF) at Pontifícia Universidade Católica (PUC) - Rio. The tensiometer measures the voltage which is related to the force and surface tension through a standard excel sheet made by the manufacturer. The result is corrected with respect to temperature and geometric factors. Before measuring the samples, the tensiometer was controlled and calibrated by measuring the surface tension between air and ethanol, γ_e. At 20 °C, γ_e was measured to 22.9 mN/m. The tabulated values for γ_e differs, but are close to 22.3 mN/m (DDBST).

At least five voltage measurements were performed on each sample, but only the three medium voltages were averaged and used for the SST calculations. The samples attained their desired temperature by standing in a temperature controlled bath for at least half an hour. It was important to ensure an isotropic distribution of the clay particles in the samples before initi-

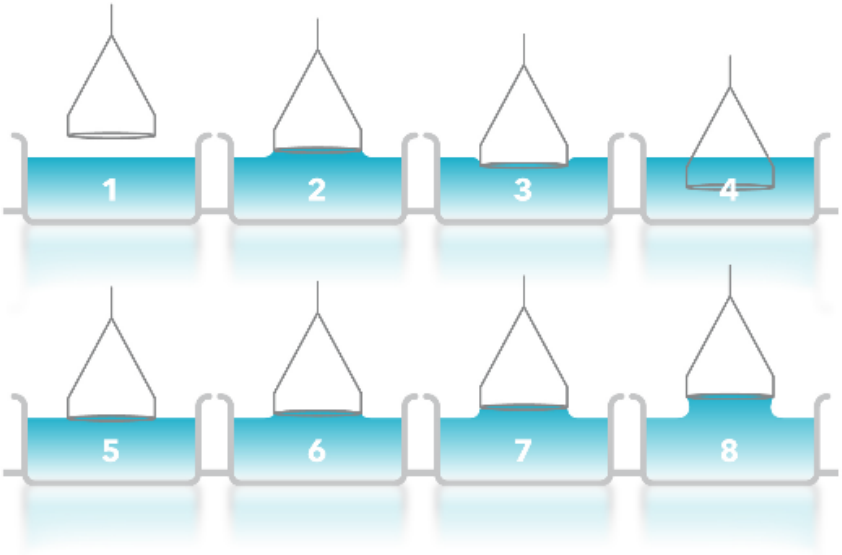

Figure 4.4: Ring positions. The numbers in this figure correspond to the numbers in figure 4.3. Illustrations adapted from Attension.

ating the measurements. The samples were therefore always shaken properly before they were poured inside the tensiometer container. The temperature during the measurements was controlled with a circulating oil system (figure 4.5 a) and measured with a digital thermometer. Figure 4.3 and 4.4 illustrate the ring positions and show the corresponding force felt on the ring during the measurements. After each measurement, the ring was cleaned by dipping it in distilled water and heating it over fire (figure 4.5 c).

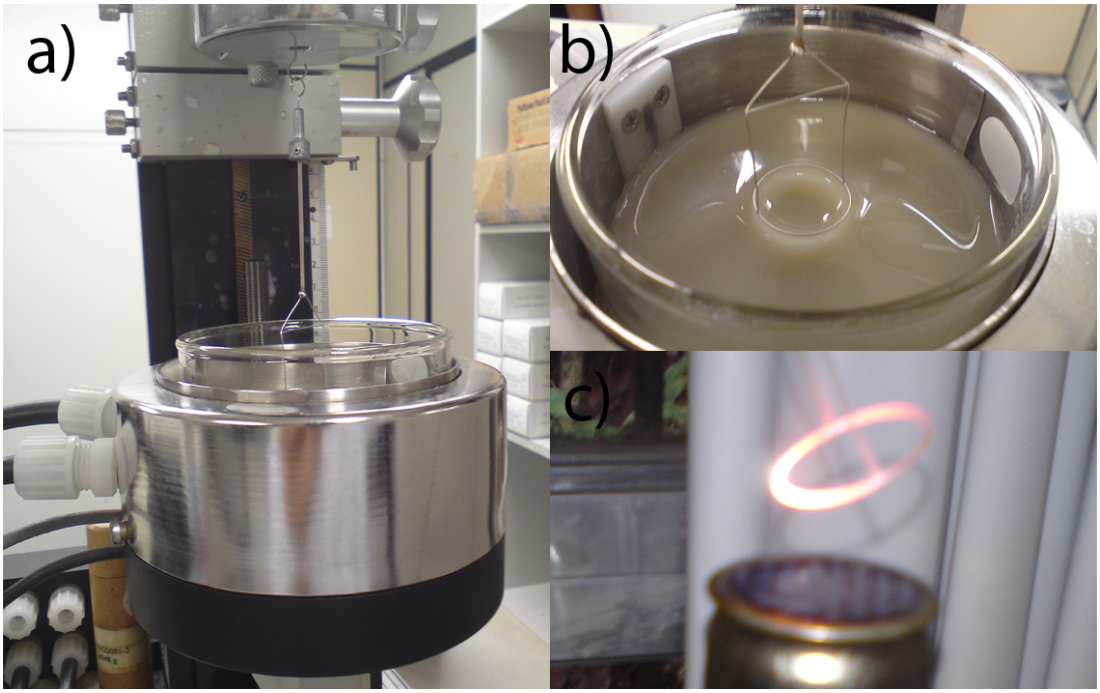

Figure 4.5: a) LAUDA VO 2001 tensiometer, b) formation of lamella as the ring rises, c) burning of the ring as part of the cleaning procedure.

Generally, the maximum voltage and thereby the SST did not change noticeably with time. However, the maximum voltage for some of the samples varied too much to be considered casual and explained by measurement errors or temperature changes. The SSTs of these samples were therefore measured against time ranging between a few seconds and half an hour. A dynamic behavior was discovered.

The Du Noüy ring method can only be used to measure the superficial surface tension between air/gas and a liquid. To find the interfacial surface tension (IST) between two liquids, one has to apply Antonoff's rule. In 1907, Antonoff found a relationship between the interfacial - and superficial surface tension. His rule states that the surface tension at the interface between two saturated liquid layers A and B in equilibrium is equal to the difference between the individual surface tensions of similar layers when exposed to air (Cardarelli, 2008):

$$\gamma_{AB} = \gamma_{B/air} - \gamma_{A/air} \tag{4.1}$$

4.4 Pendant drop method

The pendant drop method was also used to measure the superficial surface tension. This method has advantages in that it is able to use very small volumes of liquid, measure very low interfacial tensions and as opposed to the Du Noüy ring method, it can also measure the interfacial surface tension between two liquids. An image of the OCA pendant drop tensiometer is shown in figure 4.6 a).

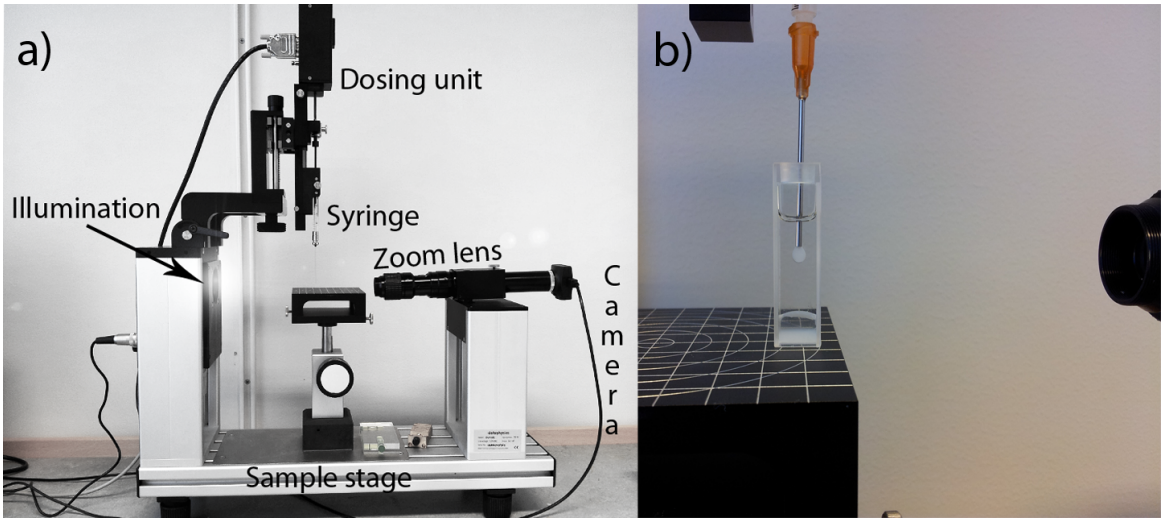

Figure 4.6: Picture of a) the pendant drop tensiometer and b) a water pendant drop with clay particles hanging from the syringe tip submerged in hexane oil.

Firstly the sample was well mixed and shaken/ultrasonicated. The syringe was then filled with the sample and mounted in the dosing unit. The outer diameter of the syringe needle was 0.5 mm, while the inner diameter was 0.31 mm. It is favorable to use needle diameters that are as large as possible, because then the drop will not form too spherically. However, one must be able to observe the whole drop to calculate the drop volume and surface tension. A scaling of the window part is therefore necessary, and this puts a limitation on the needle size. Density and dimension data were defined in the *SCA20* computer software (from Dataphysics) for later use in the volume and surface tension calculations.

The maximum image size of the camera is 768 x 576 square pixels and a pendant drop is more thin than high. The drop shape detection by the software is better the greater the drop, so to utilize the whole image, the camera was tilted 90 degrees. The syringe tip was positioned in the left and center of the tilted picture. Before initiating the measurements, the image was optimized by adjusting the illumination, contrast, focus and magnification. Droplets were then made as big as possible with the software controlled dosing unit. Depending on the sample, the camera captured pictures and/or videos with various frequencies and duration (dynamic tracking).

The pendant droplet shape is determined by the balance between gravity and surface forces. Gravity elongates the drop while the surface tension is endeavoring to hold the drop in spher-

ical form and minimize the surface. The drop shape will automatically be detected out of the contrast (bright-dark difference) of the drop image with the software. The surface/interfacial tension at the liquid interface can be related to the drop shape through the following equation:

$$\gamma = \Delta\rho g R_0^2/\beta \tag{4.2}$$

where γ is the surface tension, $\Delta\rho$ is the difference in density between fluids at interface, g is the gravitational constant, R_0 is the radius of drop curvature at drop apex and β is the shape factor. The shape factor can be defined through the Young-Laplace equation expressed as 3 dimensionless first order equations as shown in figure 4.7.

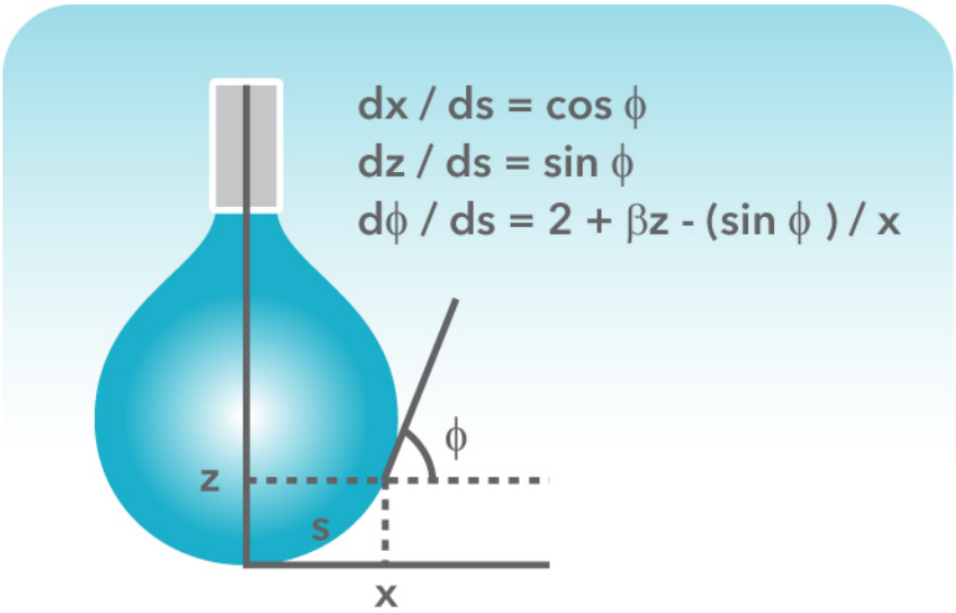

Figure 4.7: Young-Laplace equation and sketch of a droplet hanging from a syringe tip. Image from Attension.

The *SCA20* software calculates solutions of the Young-Laplace equation and thus β. With the densities of the two fluids in contact and the dimension of the droplet known, the surface tension can be calculated. The surface tension measurement data was saved as a list and later plotted in *Origin 7*. For interfacial surface tension measurements, the procedure is the same, but the syringe tip has to be submerged in the other liquid. Figure 4.6 b) shows a droplet made in hexane oil. It is important that the liquid container is square and highly transparent, otherwise it can be difficult to observe the pendant droplet. It is also crucial that the liquid in the syringe has a higher density than the liquid in the container. If not, the droplet will not be able to sink.

Dynamic measurements with samples containing clay particles were not possible. As time passed, more and more clay particles sank from the syringe and down to the pendant drop. The clay particle sedimentation increased the drop density and volume until it broke loose from the syringe tip. Figure 4.8 shows pictures of a pendant water drop exposed to air and hexane oil.

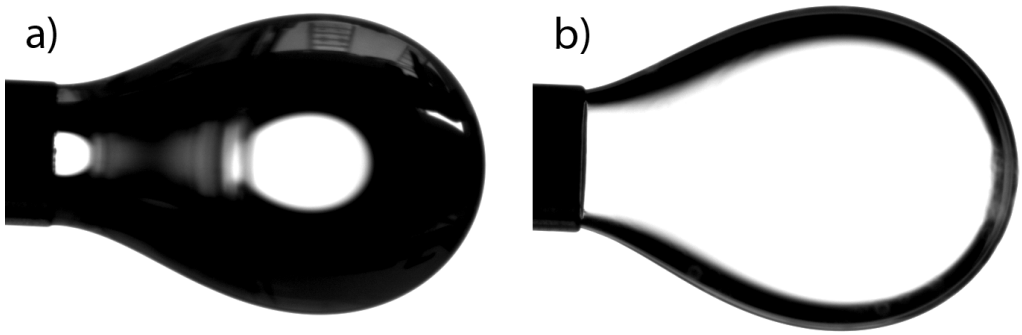

Figure 4.8: Pendant water drop exposed to a) water and b) hexane oil. The camera was tilted 90 degrees counterclockwise.

4.5 Density measurements

The specific mass (density) ρ for the different samples was measured by a *Olhaus Explorer* balance (figure 4.9 a) with an accuracy equal to $\pm$ 0.0001 g, together with a *Gay-Lussac* pycnometer (figure 4.9 b). The pycnometer was first weighed empty before a specific sample was poured inside. A temperature-controlled bath was used to control the temperature of the pycnometer and sample. When the desired temperature was reached, the pycnometer with the sample inside was weighed and the weight difference was calculated. With the sample volume, temperature and weight all known, calculating the density is straight forward.

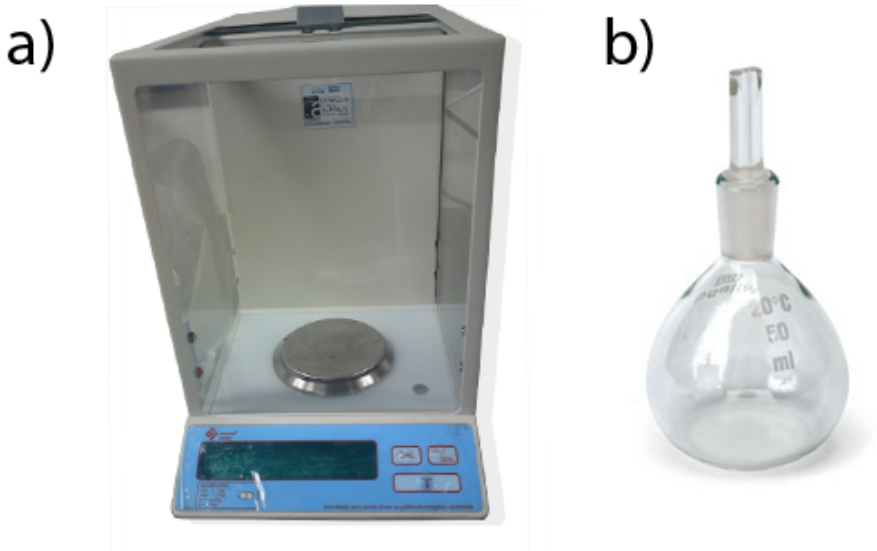

Figure 4.9: a) *Olhaus Explorer* balance and b) *Gay-Lussac* pycnometer. Picture b) is adapted from Scientific.

4.6 Viscosity measurements

The dynamic viscosity μ of the samples was calculated by multiplying the kinematic viscosity ν with the density ρ of the sample;

$$\mu = \nu \cdot \rho \tag{4.3}$$

A *Cannon-Fenske* viscometer immersed in a thermostatic bath (figure 4.10) was used to measure the kinematic viscosity. The technique evolves measuring the time a certain volume of the sample uses to flow through a known distance inside the capillary in the viscometer. One can then use the following equation to calculate the kinematic viscosity:

$$\mu = \frac{\pi D^4}{128V} g(cos\theta)t = Ct \tag{4.4}$$

where t is the measured time, g the gravity and C is a viscometer constant. C depends on the diameter of the capillary (D), the angle of the capillary (θ) and the volume of the sample (V) flowing in the viscometer. All measurements was performed at 20 °C.

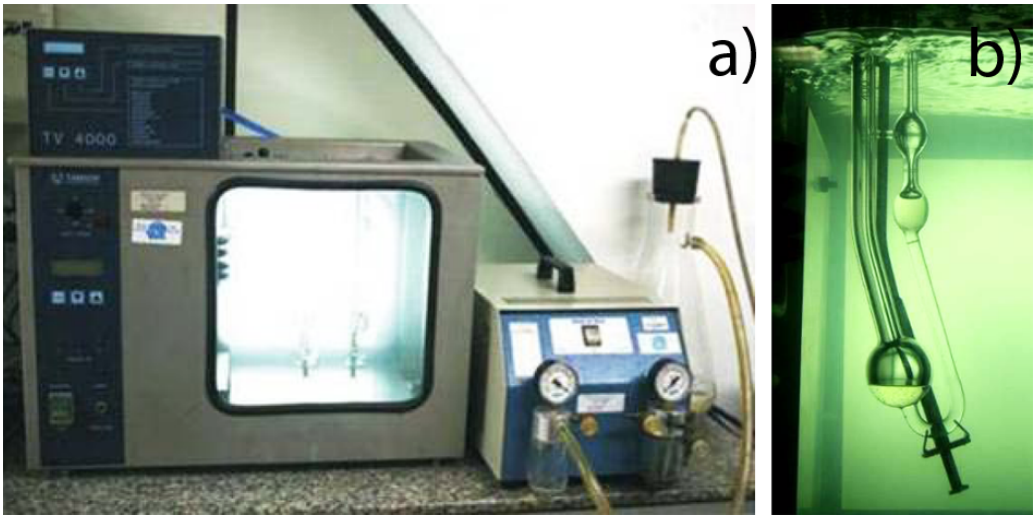

Figure 4.10: a) Thermostatic bath and b) a *Cannon-Fenske* viscometer immersed in the bath. Pictures from Campos (2011).

4.7 Droplet length measurements

Firstly, the samples were properly shaken and/or ultrasonicated before they were drawn in the syringe from the sample container center. The pipe and syringe were then connected. Avoiding air bubbles in the syringe and pipes is essential since they can alter the result. The syringe with pipe was therefore held vertically while around 2 ml of fluid was pushed out of the syringe. With no air bubbles left in the syringe and pipe, the syringe was fastened to the syringe pump and the pipe was connected to the micro capillary. To prevent leakage, it is important that the connection is tight. The flow rate will not be accurate when the system is leaking. The same procedure was performed on the oil syringe and repeated after each experiment.

With the connection well established, the syringe pump with the continuous phase[1] was turned on. When the continuous phase filled the microchannel, the disperse phase was pumped in (see figure 4.11). The initial flow rate on both pumps was set to 0.10 ml/h and with this rate, the system needed *sim* 5-10 minutes to stabilize. In this context, stable signifies continuous flow at both channels and that droplets were formed in the T-junction with more or less the same length L and interval. The microchannel was then adjusted and moved till the T-junction was placed in the microscope picture center. A proper lens was selected before the micro channel was set in focus. With the *AxioVision* software running on the computer, the exposure, gamma, intensity and scale settings were optimized. With a 2.5 $\times$ lens, the scaling was equal to 2.262 μm/pixel.

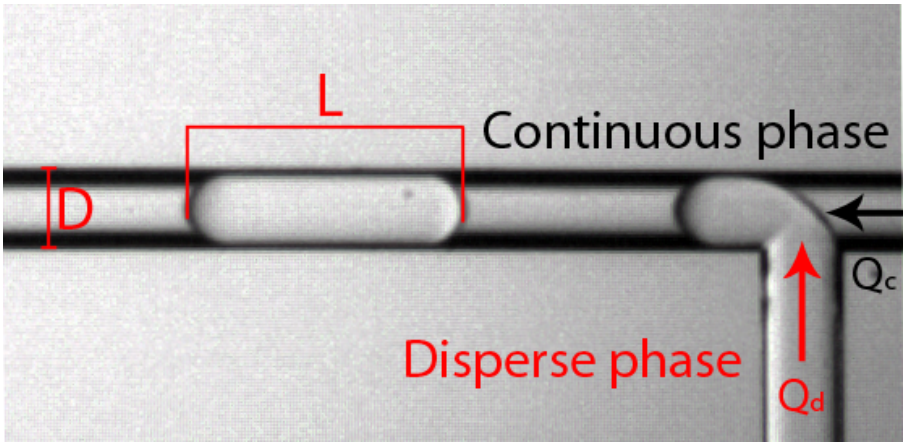

Figure 4.11: Image of droplet formation in T-junction. The continuous phase flows in the horizontal channel with flow rate Q_c, while the disperse/discontinuous phase flows in the vertical channel with flow rate Q_d. L is the measured droplet length and D is the microchannel diameter.

With all adjustments optimized, the continuous and disperse phase flow rate was set to the desired values. When the system was stable (after approximately five minutes), images were captured during five minutes and with a 30 seconds interval between each shot. 11 pictures

[1] Cross flowing mode is used with the continuous phase (water with or without clays) introduced from the horizontal channel of the T-junction and the disperse/discontinuous phase (oil) flowing through the perpendicular channel.

were captured for each flow rate. For high flow rates, the distance between formed droplets increased. This resulted in some blank captured images without formed droplets. The interval between each picture was therefore decreased to 15 seconds for the high flow rate measurements. The flow ratio between the two phases in the measurements (Q_d/Q_c ranged from 0.04 to 3. Flow ratio range and number of flow rates to use was based on previous work and experiences done with the same setup (Campos, 2011). This includes limitations of the injection system (minimum flow rate), limitations of the image acquisition (exposure) and the size of the droplets.

The droplet length (L) from all of the captured pictures was measured in *AxioVision* (see figure 4.11). The shortest and longest L was removed and an average of the nine remaining lengths (L_a) was calculated for each specific flow ratio. Eventually, the standard deviation and the standard error of the mean (SEM) were calculated and used as error bars in the generated graphs. A time effect was investigated for some of the samples. The droplets formed right after the T-junction were measured and their L_a was compared with L_a for droplets near the microchannel exit. For these measurements, a picture was captured every fifth second during one minute.

When changing samples, the microchip, syringes and tubes were thorough cleaned. The cleaning is especially important when samples contain clay particles that may block the microchannels. The cleaning procedure is as follows: empty the syringes, microchannels and tubes before washing them with hot water and soap. The parts are then ultrasonicated in hot water and soap for at least five minutes and usually multiple times. The parts are then washed with distilled water and dried.

Chapter 5

Results and discussion

5.1 Drag force

An experiment was set up to examine the frictional/drag force on a sinking silicone oil droplet with and without 1% (w/w) Na-Fh clay particles inside. A 25 cm long tube was filled with castor oil, and silicone oil droplets (with or without clay) were placed in the top and center of the tube. The time t for each droplet to sink a given distance x and droplet radius r were measured. The settling velocity of the droplets v_s could then be calculated and be used to find the frictional force given by Stoke's law:

$$F_d = 6\pi\mu r v_s, \tag{5.1}$$

where F_d is the frictional/drag force acting on the interface between the submerged silicone drop and the surrounding castor oil, μ the dynamic castor oil viscosity, r the drop radius and v_s the drop settling velocity. The settling velocity of the droplets are reached when the frictional force F_d combined with the buoyant force exactly balance the gravitational force. Figure 5.1 shows the set up with measurements.

Over the measured distance X_0 - X_f = 21.3 cm, the silicone drop without clay particles used t_{sil} = 239 min, while the silicone oil with clay particles used t_{clay} = 100 min. The settling velocity for the two drops is then calculated to be $v_{clay} \sim 3.5 \cdot 10^{-5}$ m/s and $v_{sil} \sim 1.5 \cdot 10^{-5}$ m/s. The radius of the two drops was measured to be $r_{clay} \sim 1.5$ mm and $r_{sil} \sim 1.3 r_{clay}$.

Stoke's law for settling velocity can be used to control the calculated settling velocity values and to give an estimate of the gravity effect on the droplets. The law is given by:

$$w = \frac{2(\rho_d - \rho_f)gr^2}{9\mu}, \tag{5.2}$$

where w is the settling velocity, ρ is the density (the subscripts d and f indicate droplet and surrounding fluid, respectively), g is the acceleration due to gravity, r is the particle radius and μ is the dynamic viscosity of the fluid. Inserting numbers, the theoretical settling velocity is:

$$w_{clay} = \frac{2 \cdot (965 - 961)\text{kg/m}^3 \cdot (1.5 \cdot 10^{-3}\text{m})^2}{9 \cdot 0.65\,\text{kg/m} \cdot s} \sim 3 \cdot 10^{-5}\,\text{m/s} \tag{5.3}$$

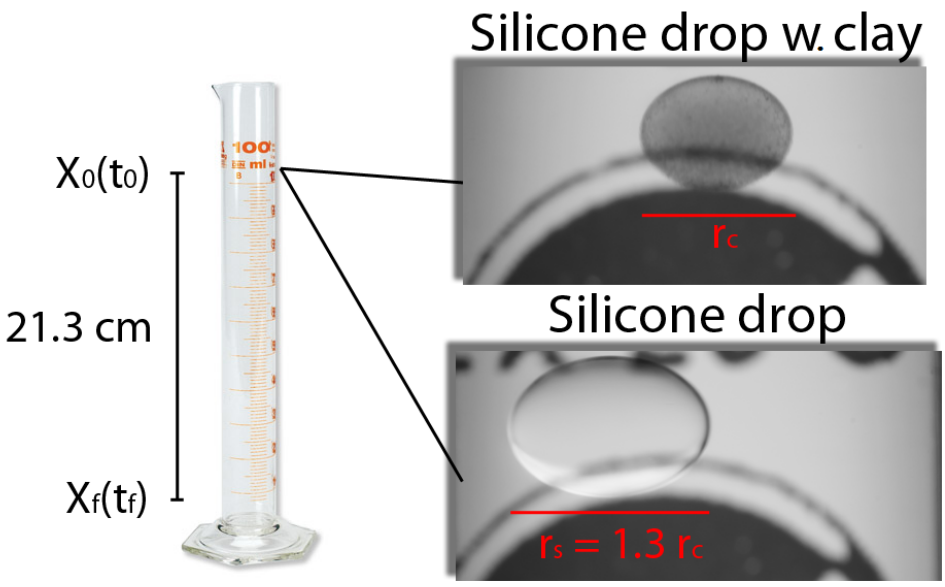

Figure 5.1: Experimental set up with measurements: Settling drop.

$$w_{sil} = w_{clay} \cdot (1.3)^2 \sim 1.7\, w_{clay} \sim 5 \cdot 10^{-5}\ \text{m/s}. \tag{5.4}$$

Stoke's law applies when the Reynold number (Re) of the particle is less than 0.1. Experimentally, Stokes' law hold within 1% for $Re \leq 0.1$ (Rhodes, 2008). Reynolds number for the settling drop is given by:

$$Re = \frac{\rho v L}{\mu} = \frac{961 kg/m^3 \cdot 3.5 \cdot 10^{-5} m/s \cdot 0.2m}{0.65 kg/m \cdot s} \sim 0.01, \tag{5.5}$$

where v is the mean velocity of the droplet relative to the surrounding fluid, L is a characteristic linear dimension (m), μ is the dynamic viscosity of the fluid and ρ is the density of the surrounding fluid. The measured settling velocity for the silicone droplet with Na-Fh clay $v_{clay} \sim 3.5 \cdot 10^{-2}$ mm/s is close to the theoretical value $w_{clay} \sim 3.0 \cdot 10^{-2}$ mm/s. The difference between $v_{sil} \sim 1.5 \cdot 10^{-2}$ mm/s and $w_{sil} \sim 5.0 \cdot 10^{-2}$ mm/s is larger. Pursuant to equation 5.2 and since $r_{sil} = 1.3\ r_{clay}$, the silicone oil drop without clay particles is expected to sink 1.7 times faster than the drop with clay particles. The expectation does not fit with the measurements where $v_{clay} > v_{sil}$. The distinction may be explained by measurement errors, Na-Fh clay particles changing the density of the drop, the fact that droplets are not spherical as assumed in Stoke's law and most important, that there is a difference in the drag force F_d acting on the droplets.

Using equation 5.1, the drag force acting on the droplets is calculated to be: $F_{sil} \sim 1.8\ F_{clay}$. The result indicates that the stress exerted by the surrounding castor oil on the silicone oil droplet in the tube is reduced by a factor approximately equal to 1.8 when 1% Na-Fh clay particles are added.

5.2 Zero field clay distribution

Before any electric field (E-field) was applied, the initial clay distribution in zero E-field was studied. 1% Na-Fh (w/w%) clay was mixed well with silicone oil until the clay particles were isotropically distributed in the sample. A droplet was then made and placed in the top center of the sample cell (filled with castor oil). The E-field was turned off during the whole experiment. Since the drop was surrounded by castor oil, it was difficult with only bare eyes to observe and predict how the clay distribution inside the drop developed. After a few minutes, the only thing one could observe with certainty was that a large part of the clay particles sank and aggregated at the bottom of the droplet. A camera and microscope were used to study the interior of the drop in more detail. The microscope was focused on the nearest drop surface and slowly shifted towards the other end of the drop while images were captured continuously (see figure 5.2).

As the focus plane of the microscope (inset in the images in figure 5.2) shifts from the nearest drop surface to the middle of the drop (figure 5.2 a - e, a larger portion of the clay particles inside the drop comes in focus and sharpens. To decide whether the clay distribution inside the drop is still isotropic or not, let us examine what particles are brought in focus and what particles stays blurred. If the particles are non-isotropically distributed along the drop surface, one would expect sharp focused particles to form rings as the focus plane intersects with the drop surface. No such sharp particle rings are observed on the images. Instead of observing focused particles in ring patterns, one finds focused particles in circles enclosed by the intersection ring. The result suggests that clay particles are isotropically distributed throughout the droplet before any E-field is applied.

One might question why no particles are focused in image 5.2 g. Not even inside the circle enclosed by the intersection ring. The explanation might be that (unfocused) blurred particles between the microscope and the focus plane conceal the focused particles that one should observe in the circle. This is not a considerable problem when the focus plane is positioned closer to the camera since the amount of blurred particles between the camera and focus plane is then much smaller. Nor would this be a problem if the particles were distributed along the drop surface.

5.3 AC E-field

As mentioned earlier in this paper, it has been shown that the viscous flow processes in a droplet are slow compared to the the dielectric polarization of the fluid (Vizika and Saville, 1992). It is therefore expected that a deformation of the droplet will be strongly dependent on the alternating current (AC) frequency f when an AC E-field is applied. When f is low, the time between changes in E-field direction is big and there is sufficient time for viscous flows in and around the drop to be induced and to affect the drop.

Figure 5.2: Images of droplets where the microscope is focused from the nearest to the farthest drop surface. The inset in each image illustrates the position of the focus plane on the droplet and is viewed perpendicular to the visual angle in the big images. The red transparent circle in each image displays the intersection of the focus plane and drop surface.

For higher f, the E-field changes too fast for viscous flows to arise. In that case, interfacial tension is the only force to balance the drop deformation caused by induced dipole charges on the drop surface. This has been confirmed by earlier work in our research group where oscillated deformations were observed for AC fields with $f = 1$ Hz, but was no longer present when $f \geq 10$ Hz. The result indicates that for our silicone/castor oil system, ~ 1 second is needed for viscous flow processes to affect the deformation. Such flow processes were avoided in our experiments by generating E-fields with AC frequencies above 200 Hz.

Silicone oil droplets with different clay concentrations (0.25 - 2%) were made in various sizes (1 - 4 mm in diameter) and studied with an applied AC E-field. The field strength was set to 600 V/mm peak to peak and applied for 90 seconds. Cameras recorded the experiment with views both perpendicular and parallel to the E-field direction. Video snapshots of a 2 mm silicone drop with 1% Na-Fh clay at times $t = 0$, 20, 40, 60 and 90 seconds after the E-field was applied are presented in figure 5.3.

A small and expected prolate deformation was observed immediately after the field was turned on ($t > 0$ s). As time evolves, the clay particles inside the drop move and align in weak chains parallel to the E-field direction. The chain pattern becomes more apparent with time and is most evident right before the field is turned off ($t = 90$ s). When viewed parallel to the E-field direction, the chains appear as dots. The position of the dots indicates that the chains are spread isotropically throughout the drop. Viscous flows inside and around the drop were not the detected during the experiment. After the field is turned off ($t > 90$ seconds), particles slowly spread out and sink to the bottom of the drop.

The droplet size did not seem to affect anything other than the drop settling velocity (as in accordance with eq. 5.2). Higher clay concentrations did not have any effect on the formation rate, but the visibility of the chains was slightly lowered. However, the strength of the E-field did affect the chain formation rate. Larger field strengths reduced the time for the chain patterns to form. No lower limit for the chain formation time was observed, but the time can be quite long (minutes) when the field strength is low (~ 100 V/mm peak to peak).
The prolate drop deformation observed in the experiment was expected and in accordance with the perfect dielectric model. The dipole charges at the drop surface are pulled towards their respective electrodes and the drop is thus stretched towards the electrodes. As stated in equation 2.15, the drop deformation depends on the squared E-field, so the field direction should not alter the prolate deformation.

The clay particle aggregation and the occurrence of chain patterns oriented along the E-field direction inside the drop is not surprising. As confirmed by (among others) Fossum et al. (2006), the clay particles become polarized and attach to each other when the E-field strength is larger than a critical value E_c. The initial isotropic clay distribution ensures that the chains spread evenly throughout the drop. As time evolves, more particles become attached to each other (forming chains). The particle attraction is too strong and the frequency of the field is too large for the particles to rotate with the changing field and break free from the chains. When there additionally is no viscous flow to break the chains, the pattern stays stable.

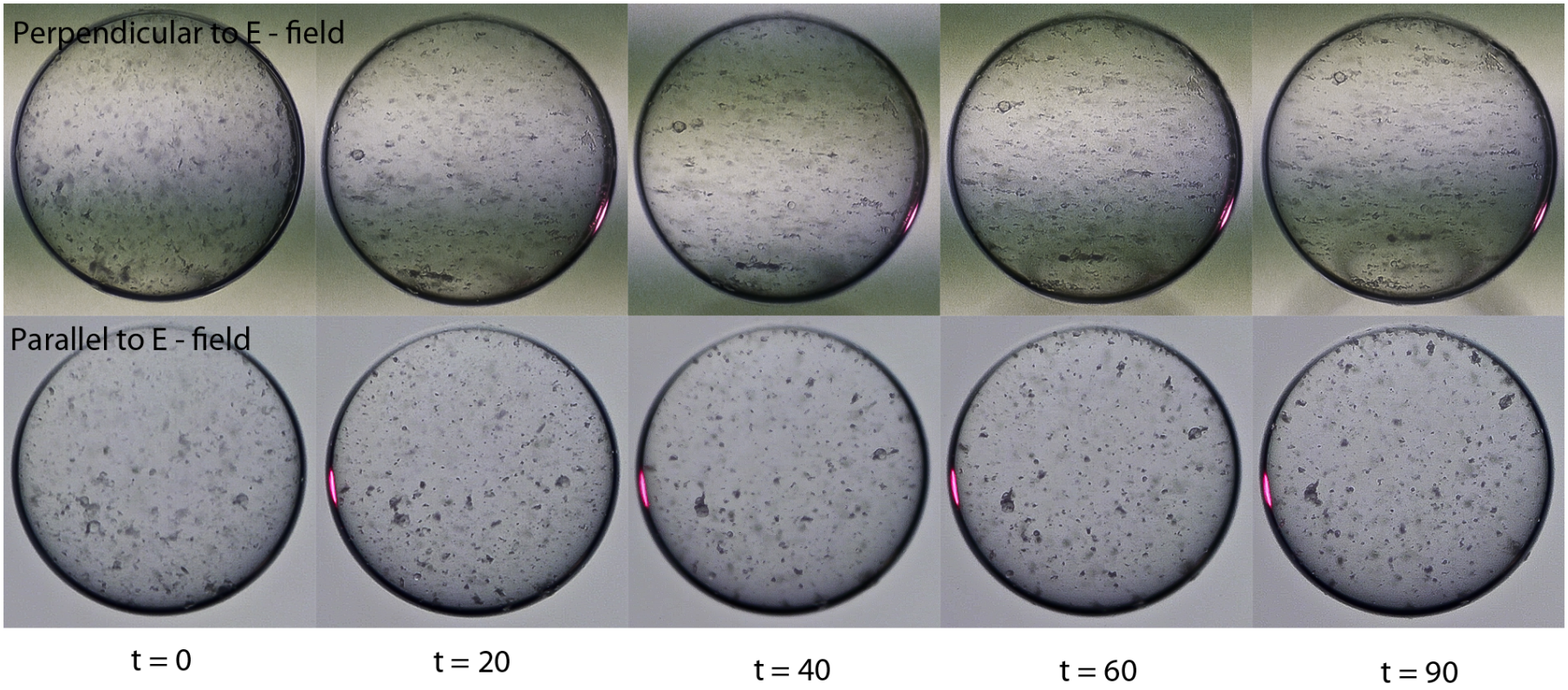

Figure 5.3: Formation of clay chain pattern viewed from two different angles at times t = 0, 20, 40, 60 and 90 seconds after an AC E-field is applied. The upper images are viewed perpendicular to the field direction and time synchronized with the lower images that have a view parallel to the field direction. The images are snapped from high definition (HD) video clips were the red light on the drop surface indicates that the field is on turned.

5.4 DC E-field

The same experiment as described in the section above was performed, but this time with a 200 V/mm direct current (DC) E-field applied for 60 seconds. Video snapshots of a $\sim$ 2 mm silicone drop with 1% Na-Fh clay at times t = 0, 5, 10, 20 and 60 seconds after the E-field was applied are displayed in figure 5.5. Before the field is applied (t = 0 s), the clay particles are isotropically distributed throughout the drop (as found in section 5.2).

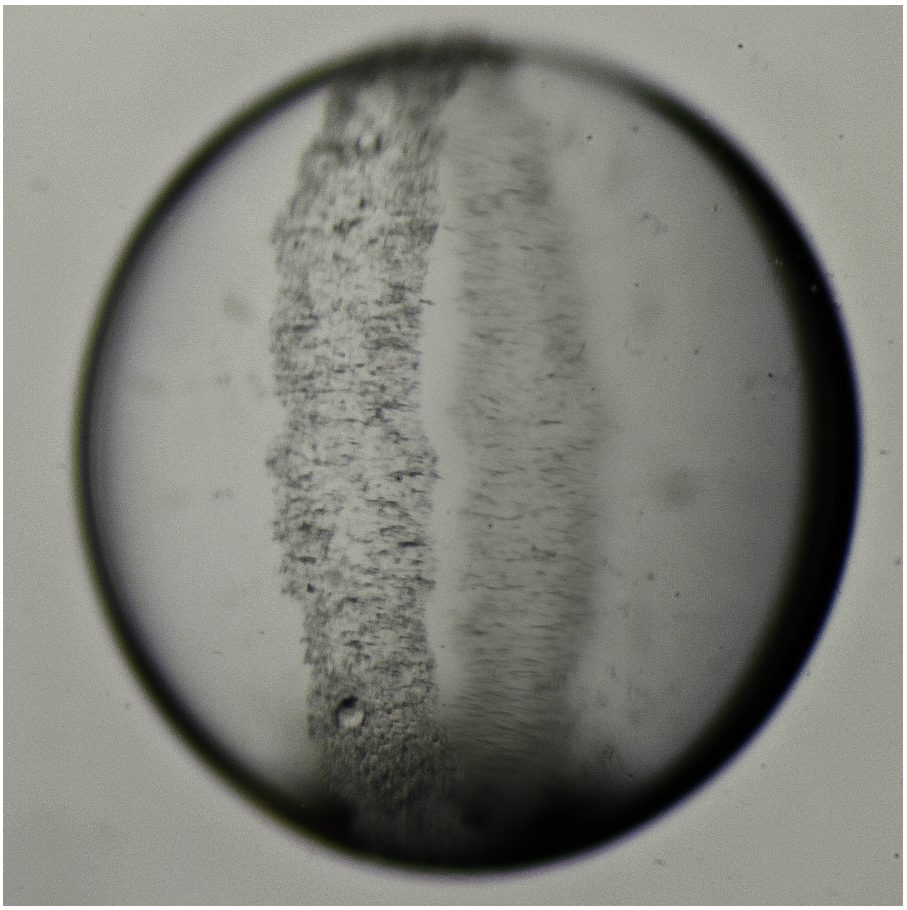

Figure 5.4: Clay particles forming a ribbon viewed from an angle $\sim$ 60 degrees from the E-field direction. The clay particles form small chains in the ribbon that are aligned with the E-field direction.

The particle distribution changes swiftly after the field is turned on (t > 0 s). From the view perpendicular to the field direction, clay particles form a ribbon in the middle of the drop composed of short chains oriented along the E-field. This pattern is recognizable already t = 10 seconds after the field is applied and is most evident right before the field is turned off (t = 60 s). Seen from the other view, parallel to the E-field, the clay particles move towards the surface of the drop and form a ring. The particles spread and sink slowly to the bottom of the drop after the field is turned off (t > 60 s). The combination of the two views suggests that the clay particles form a ribbon at the surface of the drop. This is confirmed and easier to see by viewing the droplet from an angle between the perpendicular and parallel view (see figure 5.4).

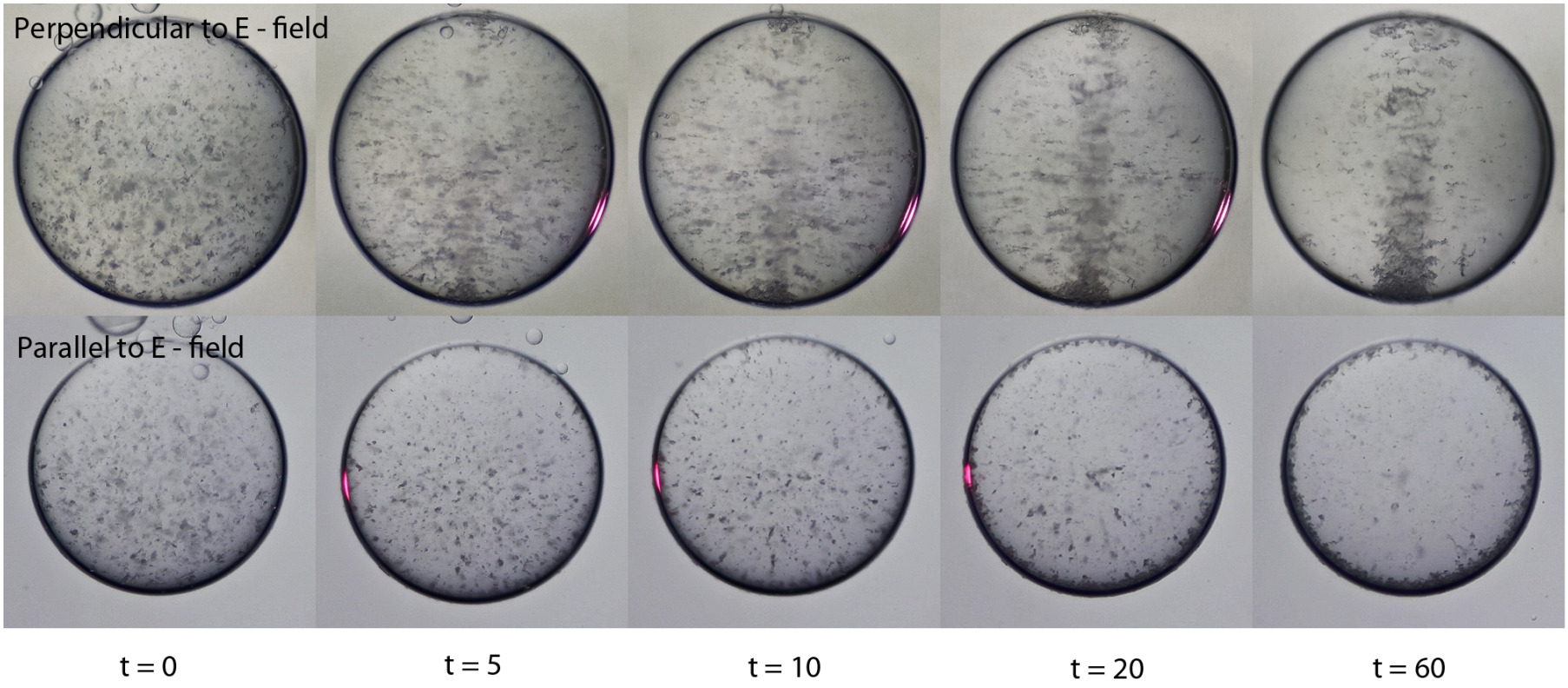

Figure 5.5: Formation of clay ribbon pattern viewed from two different angles at times t = 0, 5, 10, 20 and 60 seconds after a DC E-field is applied. The upper images are viewed perpendicular to the field direction and time synchronized with the lower images that have a view parallel to the field direction. The images are snapped from high definition (HD) video clips were the red light on the drop surface indicates that the field is on turned.

As opposed to drops affected by AC fields, the drop moved slowly and horizontally towards the positive electrode when the DC field was applied. Why the drop is negatively charged is not yet understood. As the drop moved horizontally, the formed ribbon was slightly displaced in the opposite direction of the drop movement. This is likely an effect caused by drag. In addition to horizontal drop movement right after the field was applied, viscous flow inside the drop was observed. The induced flow inside the drop was expected by Taylor (1966) in his leaky dielectric model (section 2.4). The flow inside the drop is studied and discussed in section 5.5.

The ribbon formation rate was studied in more detail by making silicone droplets with 0.5% Na-Fh clay and by varying the drop volume ($\sim$ 0.5 - 3.0 μL) and field strengths (75 - 250 V/mm). Overview pictures showing the drop and electrodes were used to measure the drop radius. The ribbon completion can be defined by examining the formation in more detail: After the field is turned on and the view is perpendicular to the E-field direction, the ribbon starts to form in the bottom of the drop and the initial clay pattern looks like the letter "V". The clay concentration is now higher in the bottom than near the top of the drop. As time goes on, the concentration evens out and the "V" shape turns into a "Y" shape. The clay particles close up before the clay concentration is evenly distributed in the drop and the ribbon achieves a "I" shape. The "V" $\rightarrow$ "Y" $\rightarrow$ "I" transition is displayed in figure 5.6.

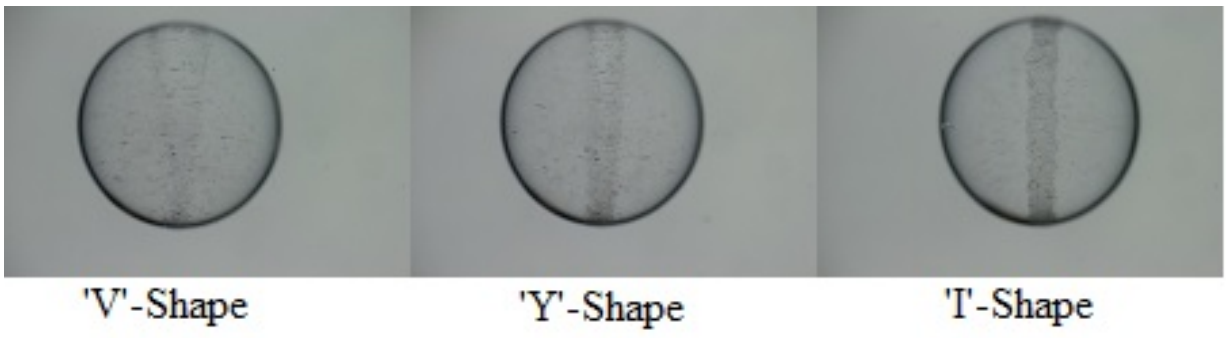

Figure 5.6: Clay particles are gradually forming a ribbon by making a "V" $\rightarrow$ "Y" $\rightarrow$ "I" transition. The view is perpendicular to the E-field direction. The images were captured by Knut Kjerstad.

The "I" shape is defined as the completion of the ribbon, and the time t for the clay particles to form this shape was measured. The "V" $\rightarrow$ "Y" $\rightarrow$ "I" transition is probably present due to the settling velocity of the drop and gravity effects. Xu et al. (2006b) discovered that settling displaces the charge distribution on the drop surface. To compensate for the displaced charge distribution, the settling causes flowlines in the lower hemisphere of the drop to increase in size. The viscous flow speed inside the drop increases and eventually brings the particles to the surface faster. The flowlines for a settling drop and a deformed drop are illustrated in figure 5.7. Changes in the flowlines between a drop with and without clay particles are not expected to be large since the drop settling velocity is very slow compared to the viscous flow inside the drop. However, the effect should be investigated in future work.

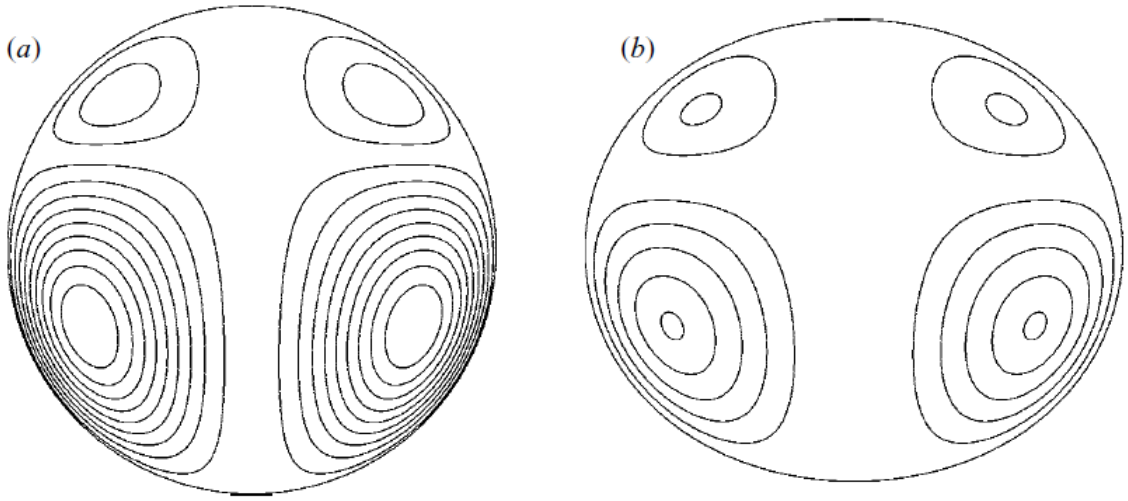

Figure 5.7: Illustration of streamlines inside (a) a spherical drop and (b) a deformed drop. Illustrations from (Xu et al., 2006b).

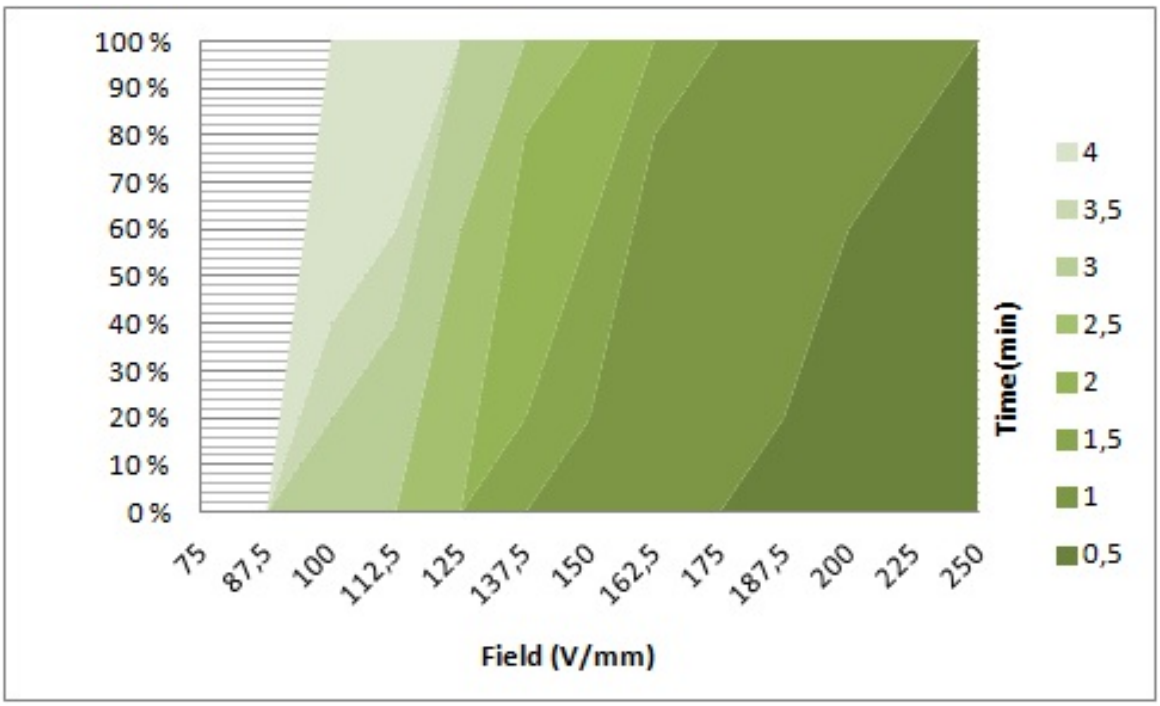

Figure 5.8: The percentage of droplets completing ribbon pattern in time t against different E-field strengths. The color ranges indicate measured time for clay particles to form ribbon. Darker color indicates less time. The chart is made by Knut Kjerstad.

The sample cell height and the settling of the droplets limited the measuring time to ~ 4 minutes. This time was not sufficient for ribbon formation when the field strength was below 100 V/mm. The time for ribbon completion t was measured for at least five droplets with the same size and being affected by the same E-field. The percentage of ribbons formed in time t against different E-field strengths is presented in figure 5.8. The measurements show that

for increasing field strength, less time to form ribbons is needed. For instance, one see that for $E = 200$ V/mm, half (50%) of the measured droplets formed the ribbon pattern after 30 seconds (0.5 min.), while 2.5 minutes were needed for the same number of droplets to form a ribbon when $E = 125$ V/mm. A logaritmic plot of the average measured time for a ribbon to form in droplets against different field strengths is presented in figure 5.9. The data points in the plot are well fitted with a slope having a value close to -2.4. The fit indicates that the time for ribbon completion is proportional to $cE^{-2.4}$, where c is a constant. This seems to be a reasonable result since the drop deformation and viscous flow inside the drop are proportional to aE^2 (section 2.4). I.e., we suppose that the ribbon formation is highly dependent on the viscous flow velocity inside the drop.

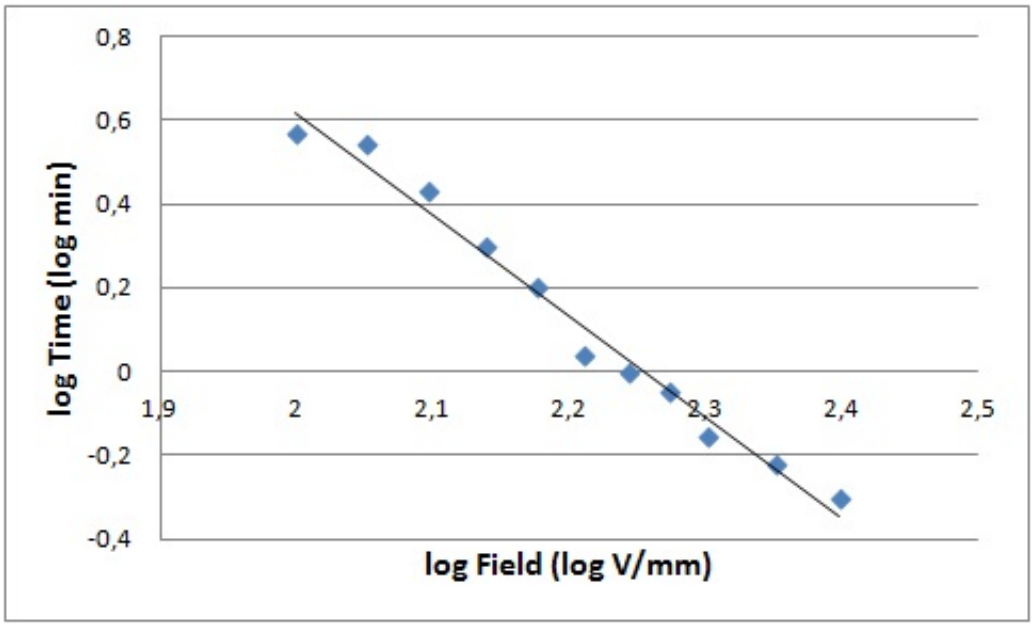

Figure 5.9: Log-log plot: Average time for ribbon completion against different E-field strengths. The graph is made by Knut Kjerstad.

In this experiment, pictures of the droplets were captured every 15 seconds. A higher capture frequency would have decreased the measurement uncertainties, especially for the stronger E-fields where the ribbon forms swiftly. It was also hard to define the "I" shape and the completion of the ribbon pattern. The definition problem makes this experiment hard to compare with potential future experiments since the ribbon completion definition may change a bit from person to person and from measured drop to drop. It is therefore possible that the measured proportional factor $cE^{-2.4}$ is closer to cE^{-2} and in better accordance with the leaky dielectric model.

We did not have sufficient time to perform time measurements for different clay concentrations and types. It was weakly observed and is also expected that an increase in clay concentration increases the ribbon width and the formation rate. This would be an interesting study for future work. Additional plots of the fraction of droplets to form ribbon in 1 min. for different drop sizes against E are presented in the appendix B chapter. For three different drop sizes, one see that the number of drops to complete a ribbon in 1 min. has a aE^2 linear dependence.

This result supports our suggestion that ribbon formation strongly depends on the induced viscous flow inside the drop.

Similarly to the previous AC field experiment, the clay particles inside the droplet form chains when the E-field is applied. The particles become polarized and attach to other dipoles. Viscous flow inside the drop is the factor that distinguishes the particle behavior in the two experiments. The induced viscous flow limits the size of the aligned chains in the DC field and thus prevents the chains from forming throughout the whole drop. The clay particles follow the flow pattern before they gradually attach to other particles at the drop surface and form a ribbon. It is not completely understood why the particles move to the drop surface. The centrifugal force arising from the circular flow may be one reason. We remember from section 2.4 and figure 2.6 that the tangential electric stress and thus the viscous flow at the droplet equator is zero since no free charges exist there. This explains why a ribbon is allowed to form and stay at the droplet equator without being destroyed.

5.5 Flow pattern

The flow inside the droplet was traced by capturing video clips and by observing the movement of clay particles when an E-field was applied. The flow seemed to have the same characteristic pattern that Taylor described in his leaky dielectric model (see figure 2.6). The flow outside the drop was traced by adding clay particles to the surrounding castor oil. The flow pattern around the drop resembled the Taylor flowlines as well.

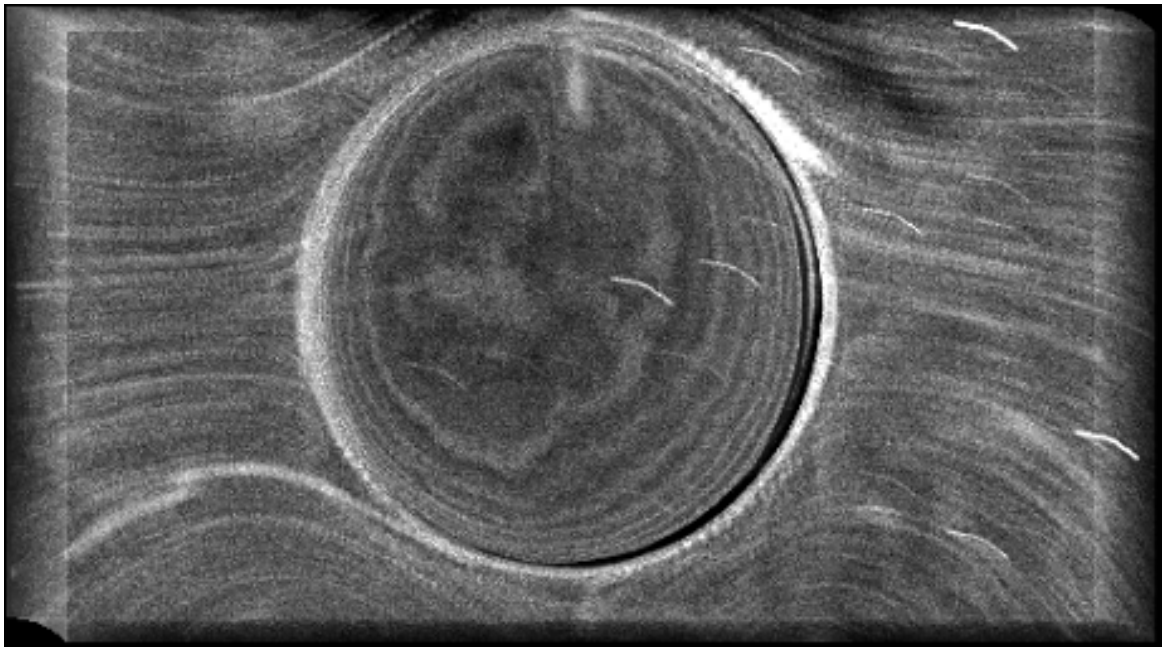

Figure 5.10: Illustration of the induced flow pattern around a drop when a DC E-field is applied. The image is created by assembling several video frames so that the tracer particles appear as flowlines. The illustration is made by Knut Kjerstad.

To investigate whether or not the polarized clay particles affect the viscous flow, the clay particles were substituted with dielectric latex beads ($\sim$ 10 μm in diameter). Latex beads were added to both the silicone and castor oil and used to trace the flow. Low concentrations ($<$ 1%) were used to ensure a high visibility. The flow pattern appeared exactly the same as the flow pattern observed by tracing clay particles. The result strongly indicates that the induced viscous flow inside and outside the drop is unaffected by the clay particles and their interactions. An illustration of the flow pattern around the drop is presented in figure 5.10.

The flowlines resembles those described by Taylor (1966). Due to focus and contrast problems, an illustration of the flow pattern inside the drop was hard to make. The flow pattern was however possible to observe in some of the video clips. New measurements could be improved by using a better light source (e.g. a laser sheet) and a dark background. As predicted by the theory, the latex beads formed a narrow ribbon without chains when the E-field was applied. The result is simply explained by the main difference between latex beads and clay particles, namely their ability to polarize or not. Latex beads are dielectric particles which will not polarize in an E-field and make electric interactions with other particles.

5.6 Rotation

When we performed the flow visualization experiments and applied E-fields with strengths above $\sim$ 300 V/mm, a new and unexpected phenomena appeared. The droplet deformation was no longer symmetric (axes perpendicular and parallel to the E-field direction) and the drop started to rotate. The deformation axes were tilted and the tilt angle β increased proportionally with the E-field strength. This phenomenon resembles the Quincke rotation. The tilt angle was difficult to measure since the drop never rotated solely in the plane normal to the camera view. In section 2.5 we found that the tilt angle β increases when the applied E-field E_0 increases and is larger than a critical value E_Q (equation 2.25), which is in accordance with our observations. It is hard to say for sure, but it appears that the direction of the drop rotation is perpendicular to the E-field direction.

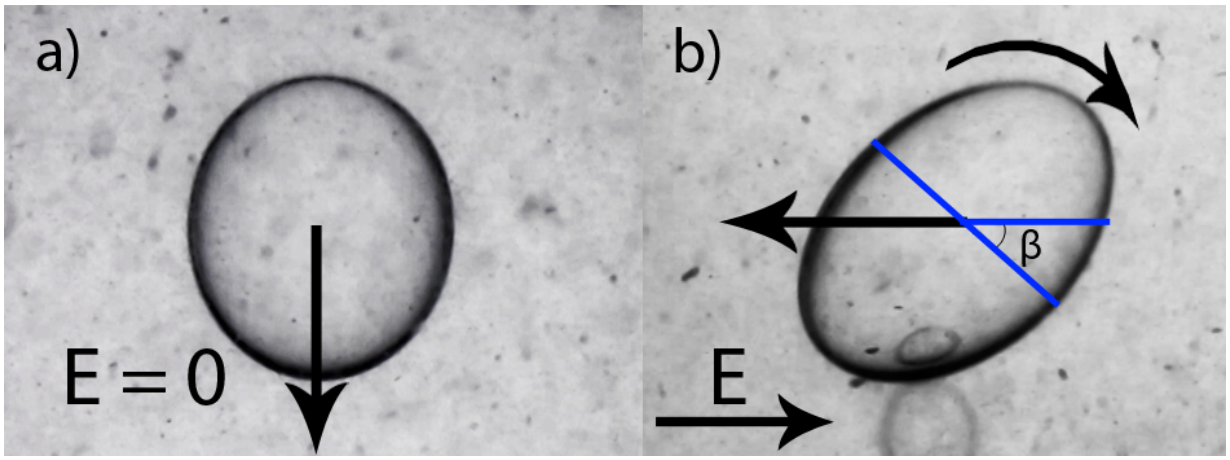

Figure 5.11: a) The E-field is zero and the droplet sinks towards the bottom of the sample cell. b) A 500 V/mm DC field is turned on. The droplet rotates counterclockwise, deforms and moves towards the positive electrode. Stronger E-field strength results in larger tilt angle β, oblate drop deformation, larger induced flow velocities and drop movement.

Figure 5.11 shows two video frames of the drop before and after a 500 V/mm DC field is applied. The particles in the surrounding castor oil are latex beads used to trace the flow. The latex beads in the castor oil showed that the flow around the drop rotated and increased in velocity when the E-field increased. The drop did not only move horizontally against the positive electrode after the field was turned on, it also moved in the camera view direction. The drop rotation and movement made it hard for us to track the drop and focus the image. These movements increased when the E-field became stronger. We did not study this rotation phenomenon in more detail due to limited time and problems with tracking the drop. It would be interesting to study the critical field strength E_c for droplet rotation, to track the flow inside the drop during rotation, measure tilt angle and confirm that the drop always rotate in a direction perpendicular to the electric field.

5.7 Surface tension: Ring method

As described in the method chapter, the Du Noüy ring method was used to measure the superficial surface tension (SST) γ between air and distilled water with different clay types and concentrations Φ. The measurements were necessary and important to choose clay types and concentrations for the later microchannel flow experiments.

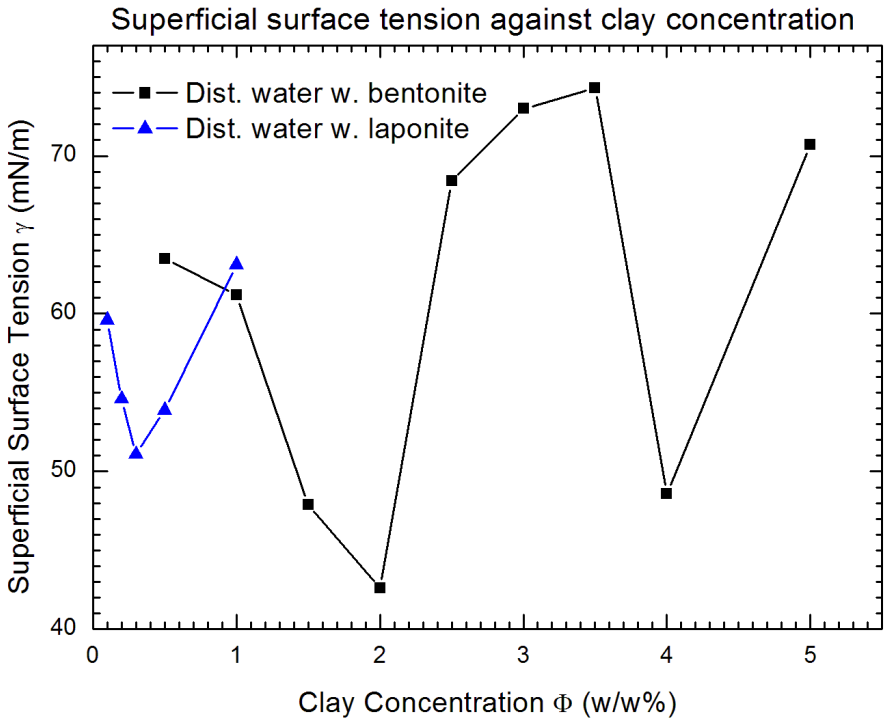

Figure 5.12: Superficial surface tension between air and distilled water with different laponite and bentonite clay concentrations. All measurements are performed at $T = 20$ °C.

The SST γ between air and water with different laponite and bentonite clay concentrations Φ is presented in figure 5.12. For low clay concentrations, the SST for water with both laponite $\gamma_{a,l}$[1] (triangle) and bentonite $\gamma_{a,b}$ (rectangle) approaches the measured SST for distilled water without clay $\gamma_{a,w}$ (63.7 mN/m), as expected. $\gamma_{a,l}$ appear to have a minimum for Φ_l equal to 0.25%. Φ_l higher than 1.0% were not measured since laponite starts to gel around this concentration (Gabriel et al., 1996). Local minimum values for $\gamma_{a,b}$ was found for Φ_b equal to 2 and 4%.

The fluctuating behavior of $\gamma_{a,b}$ against Φ_b may be explained by big bentonite grains in the sample and errors in the measurements. Large clay particles will sediment fast and lower the clay concentration near the air/water surface. Bentonite grains in contact with the measuring De Noüy ring may as well alter $\gamma_{a,b}$ considerably. SST measurements were repeated for some of the bentonite concentrations, but with no change in the results. Figure 5.12 shows that

[1]The subscripts a, l, b, w, n and o will hereafter be used to denote air, laponite, bentonite, distilled water, sodium-fluorohectorite (Na-Fh) and OP3 mineral oil, respectively.

both laponite and bentonite clay particles (in distilled water) have a heavy influence on the SST. For some bentonite concentrations, $\gamma_{a,b}$ even exceeds $\gamma_{a,w}$. However, the measured SST for distilled water $\gamma_{a,w}$ was unusually low[2] and some of these values should not be fully trusted until confirmed by other measurements.

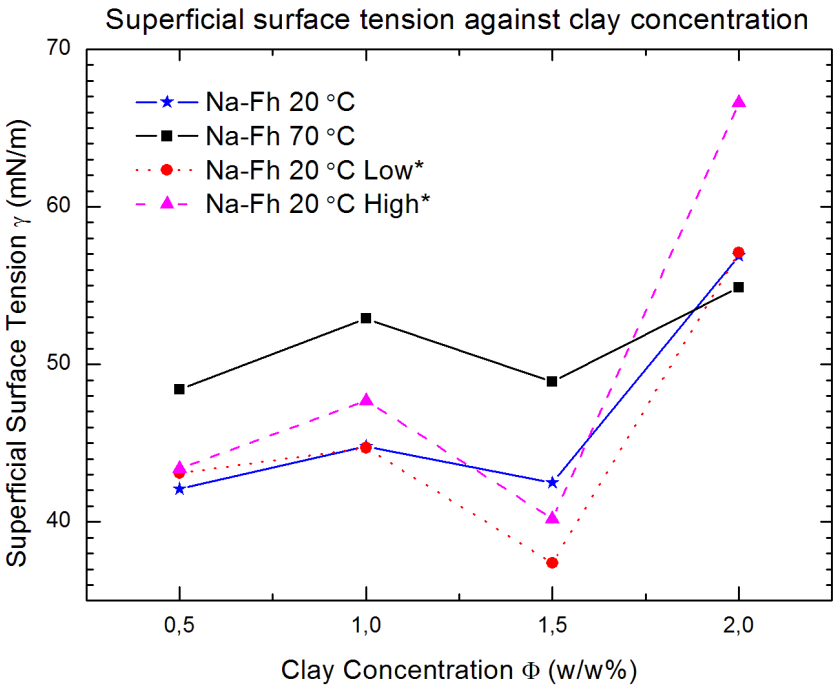

Figure 5.13: Superficial surface tension between air and distilled water with different Na-Fh clay concentrations. * Signifies that the sample has been preheated to 70 °C. γ^*_{20} exhibited time dependence for the preheated samples. High and low denotes the highest and lowest observed γ^*_{20} values.

Similar measurements were performed for distilled water with different Na-Fh clay concentrations and temperatures (figure 5.13). For $0.5\% \leq \Phi_n \leq 2.0\%$, the measured SSTs at both 20 °C γ_{20}[3] (star) and 70 °C γ_{70} (rectangle) are lower than the measured $\gamma_{a,w}$ value (63.7 mN/m). The difference between γ_{20} and γ_{70} for $\Phi_n \leq 1.5\%$ is significant. By heating the sample (water with Na-Fh), γ seems to increase. The minimum SST values are measured for dist. water with low Na-Fh concentrations Φ_n, exept for the preheated samples where γ^*_{min} occur when $\Phi_n = 1.5\%$. Figure 5.13 shows that Na-Fh clay alter γ considerably. γ_{20} ranges between 42 and 57 mN/m, while γ_{70} varies between 48 and 55 mN/n for $0.5\% \leq \Phi_n \leq 2.0\%$.

Samples measured at 70 °C were cooled down before new SST measurements were performed at 20 °C. Unlike previous samples, γ^*_{20} decreased with time during the measurements. The dashed (pink) line in figure 5.13 shows the initial measured SST values, while the dotted (red) line

[2] $\gamma_{a,w}$ was measured to 63.7 mN/m at the lab with the ring method. The tabulated SST value for pure distilled water exposed to air and measured at room temperature is 72.8 mN/m.

[3] The numbers in subscripts denote the sample temperature in celsius degrees, while * indicate that the sample has been preheated to 70 °C.

shows the measured equilibrium SST values after a certain time t. New measurements were performed where the time dependence was studies more in detail. The main result from these measurements is presented in figure 5.14. No apparent time dependency was observed for the samples with other clay types: only variations small enough to be explained by measurement errors were evident.

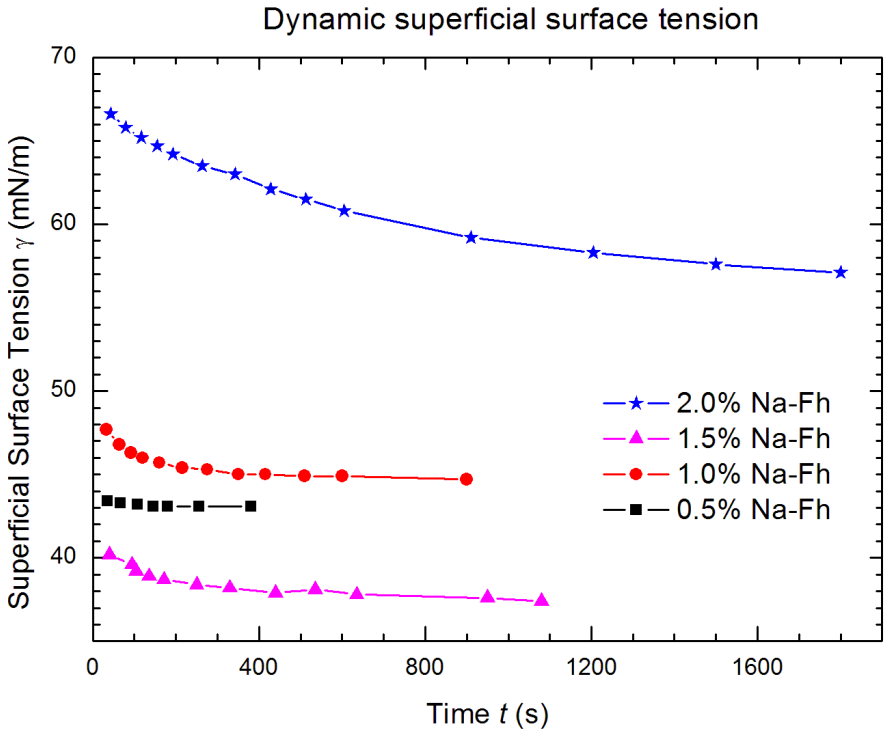

Figure 5.14: Dynamic superficial surface tension between air and distilled water with different Na-Fh clay concentrations.

As seen in the figure above, the decrease in γ^*_{20} with time t is greatest for the sample with Φ_n= 2.0% (star). During 30 minutes, γ^*_{20} decreases with approximately 10 mN/m (67 to 57 mn/m). The decrease in γ^*_{20} for the samples with Φ_n equal to 1.5% (triangle) and 1.0% (circle) is small ($\sim$ 3 mN/m) and less time t is required to reach stable states. For Φ_n = 0.5% (rectangle), the time dependence is too small to be more than measurement errors. The result suggests that Na-Fh concentration Φ_n and time t have a strong influence on $\gamma_{a,n}$. For the preheated samples measured at 20 °C, the difference between the highest(Φ_n = 2.0%) and lowest (Φ_n = 1.5%) measured γ^*_{20} value is 33 mN/m (67 - 34 mN/m). Such a big difference in $\gamma_{a,n}$ should be sufficient to affect the droplet formation in a microchannel T-junction, as we will study later(section 5.9). The measured SST and density values for dist. water with different clays and concentrations are summarized in table 5.1.

Table 5.1: Measured superficial surface tension (SST) and density values. Samples marked with * are preheated to 70 °C before cooled down and measured at room temperature. Samples that are not specifically marked are measured at room temperature (23 °C).

Liquid	Clay concn. (w/w%)	Density (g/ml)	SST (mN/m)
Dist. water w. bentonite	0.5	0.9989	63.5
	1	1.0038	61.2
	1.5	1.0040	47.9
	2	1.0073	42.6
	2.5	1.0047	68.4
	3	1.0167	73.0
	3.5	1.0173	74.3
	4	1.0220	48.6
	5	1.0294	70.7
Dist. water w. laponite	0.1	0.9985	59.6
	0.2	0.9990	54.6
	0.25	0.9993	51.1
	0.5	1.0012	53.9
	1	1.0026	63.1
Dist. water w. Na-Fh (20 °C)	0.5	1.0045	42.1
	1	1.0047	44.8
	1.5	1.0029	42.5
	2	1.0104	56.9
Dist. water w. Na-Fh (70 °C)	0.5	0.9816	48.4
	1	0.9790	52.9
	1.5	0.9822	48.9
	2	0.9930	54.9
Dist. water w. Na-Fh (20 °C)*	0.5	1.0045	46.7
	1	1.0047	47.6
	1.5	1.0029	
	2	1.0104	
Dist. water	0	0.9980	63.7
Tab. value dist. water	0	0.9980	72.8
Ethanol	0	0.8075	22.9
Tab. value ethanol	0	0.7895	22.4

5.8 Surface tension: Pendant drop method

To confirm and better explain some of the superficial surface tension (SST) results obtained with the Du Noüy ring method (section 5.7), new surface tension measurements were performed, this time with the pendant drop method at the Ångström laboratory in Uppsala. The measured SST and interfacial surface tension (IST) against air and hexane oil, respectively, are presented in table 5.2. The tabulated SST values are averages of the 10 first SST measurements (during $\sim$ 2-4 minutes), while the tabulated IST values are single measurements taken right after ($\sim$ 0-30 seconds) the pendant drop was made. Average of the IST values was not calculated since the IST decreased with time and since only a few measurements were performed for each sample. Generally, the pendant drop (surrounded by hexane oil) broke lose from the syringe tip before the IST steadied. The dynamic surface tension measurements will be discussed more thoroughly later in this section.

The SSTs measured with the pendant drop method (table 5.2) differ considerably from the SSTs measured with the Du Noüy ring method (table 5.1). First, let us compare the measured SST value for pure distilled water, $\gamma_{a,w}$. This value was measured to 63.7 mN/m at the laboratory at PUC (Pontificia Universidade Católica) Rio and measured to 72.6 $\pm$ 0.3 mN/m at the Ångström laboratory in Uppsala with the Du Noüy ring and pendant drop method, respectively. The distilled water at PUC was expected to be a bit contaminated, and the measured $\gamma^P_{a,w}$[4] supports this when compared to the standard tabulated value (72.8 mN/m) and $\gamma^U_{a,w}$ (72.6 $\pm$ 0.3 mN/m). $\gamma^P_{a,w}$ was controlled with several SST measurements, all giving the same result. A new pendant drop instrument has been bought and is being installed at PUC while this thesis report is written. It would be interesting to compare the SST measurements presented in table 5.1 with similar measurements performed with the new pendant drop instrument.

It is hard to say if water contamination acts on clay particles in a distinct way so that the SST dependence on clay particle concentration presented in figure 5.12 and 5.13 can be explained. Repeating the SST measurements at PUC with the Du Noüy ring method and pure dist. water without contamination would probably give the answer. It is also possible that the clay particles interacted with the ring during the measurements. This might explain the incoherent SST vs. clay concentration behavior seen in figure 5.12 and 5.13.

Since the distilled water at PUC and Uppsala had different degrees of purity, the two independent SST measurements are difficult to compare. We do not know how the water contamination affects the clay particles and the SST. However, the SST measurements performed at Uppsala with the pendant drop method (table 5.2) indicate that neither Na-Fh, bentonite or laponite clay in *pure* distilled water have any considerable effect on the SST. Measurements with clay and NaCl concentrations in dist. water was also performed, but no big difference in the SST was observed.

[4]The superscripts P and U will hereafter denote the SST (γ) measured at PUC and Uppsala, respectively. As before, the subscripts a, l, b, w, n and o denote air, laponite, bentonite, distilled water, sodium-fluorohectorite (Na-Fh) and OP3 mineral oil, respectively.

Table 5.2: Measured superficial surface tension (SST) and interfacial surface tension (IST) exposed to air and hexane oil, respectively. All measurements are performed at room temperature (23 °C). Samples marked * are preheated to 70 °C before cooled down and measured at room temperature.

Dist. water w.	SST (mN/m)	Error	IST (mN/m)	Error	Theoretic IST
0 % clay (pure dist. water)	72.6	0.3	40.1	0.5	43.7
0.25% laponite	71.7	0.1	40.9	1.0	42.7
0.5% Na-Fh	72.2	0.2	37.9	0.3	43.2
1% Na-Fh	71.2	0.1	42.0	0.2	42.2
1.5% Na-Fh	71.3	0.2	39.3	0.7	42.3
2% Na-Fh	70.4	0.1	38.0	1.3	41.5
2% bentonite	71.2	0.2	-	-	42.3
Triton X-100 $C >$ CMC	31.7	0.1	3.3	0.2	2.8
Triton X-100 $C =$ CMC/100	67.4	0.2	-	-	38.4
1.5% Na-Fh*	70.4	0.1	40.4	0.5	41.4
2% Na-Fh*	69.5	0.3	38.3	1.6	40.5
1 mM NaCl & 0.5% laponite	71.7	0.1	39.4	1.0	42.7
1 mM NaCl w. 1% Na-Fh	70.3	0.2	39.8	0.9	41.4
5 mM NaCl w. 0.5% laponite	71.9	0.1	38.6	0.7	43.0
5 mM NaCl w. 1% Na-Fh	71.0	0.2	37.9	0.8	42.1
Hexane oil	29.0	0.3	-	-	-

Triton X-100 (Delivered by Sigma Aldrich) with critical micelle concentration (CMC) $\sim 2 \times 10^{-4}$ mol dm^{-3} was used as surfactant in some of the experiments. By using surfactant in the dist. water, the SST could be lowered (see section 2.9) in a controlled way. The SST for dist. water with surfactant concentration C above the CMC was measured to 31.7 $\pm$ 0.1 mN/m, which is close to the 31 mN/m value measured by the manufacturer (Dow). Based on the measurements and comparisons with tabulated values, the pendant drop method seems to be more accurate and reliable for SST measurements with water and clay than the Du Noüy ring method .

Interfacial surface tension (IST) measurements against hexane oil were also performed with the pendant drop method. The surrounding liquid was originally supposed to be OP3 mineral oil (which was also used in the microchannel flow experiments at PUC), but logistic problems and limited time excluded the oil from the IST measurements. Hexane oil has many properties (e.g. viscosity, density, transparency and surface tension) which resemble the OP3 mineral oil and was therefore chosen as the surrounding liquid. The ISTs measured right after the pendant drop was made (inside the hexane oil) are presented in table 5.2. One sees that the IST of distilled water with or without clays and/or NaCl in hexane oil, does not differ considerably. The measured ISTs are all close to 40 mN/m. This result was expected since the measured SSTs against air were quite similar as well.

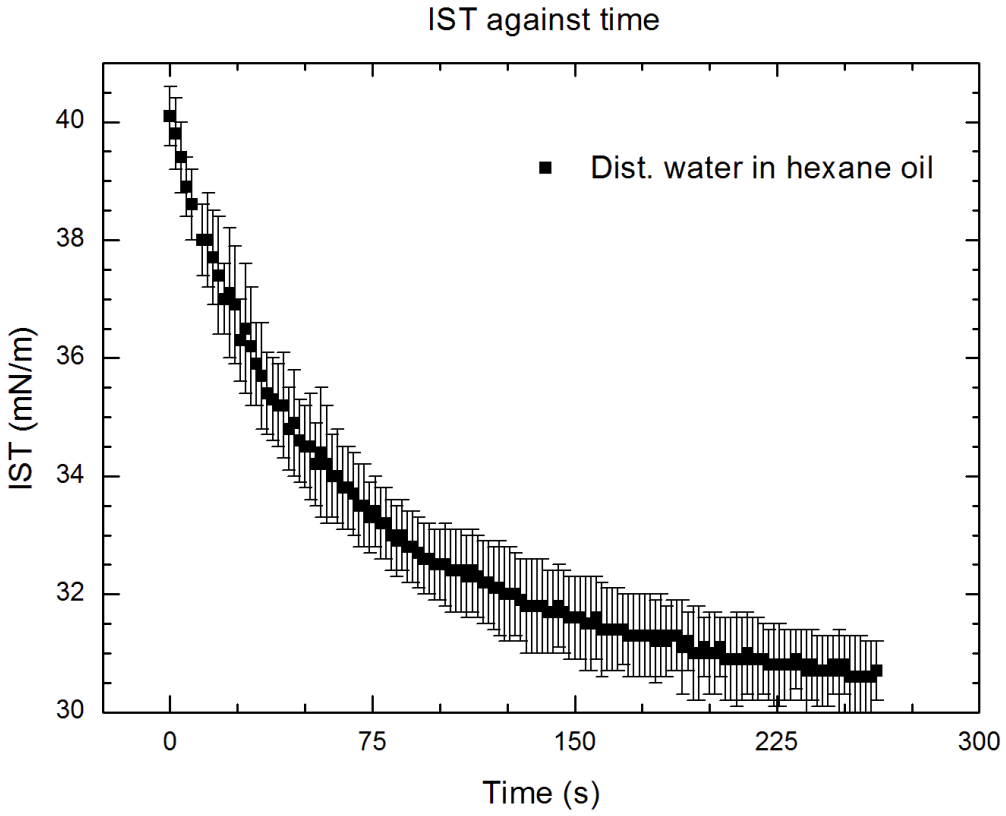

Figure 5.15: Dynamic interfacial surface tension (IST) of a distilled water pendant drop surrounded by hexane oil.

The theoretic IST can be found by using Antonoff's rule (equation 4.1) and by calculating the difference between the individual superficial surface tensions of similar layers when exposed to air. The calculations are performed and tabulated in table 5.2 as theoretic IST. A comparison between the theoretic and measured IST values shows that Antonoff's rule, in this case, is a good estimation. However, the IST against hexane oil is not constant: it decreases with time. Figure 5.15 shows how the IST of a distilled water pendant drop in hexane oil changes with time. Right after the drop was made, the initial IST was measured to 40.1 mN/m (as tabulated in table 5.2). The IST decreases and stabilizes around 30.7 mN/m after $\sim$ 240 seconds. Droplets with clay and/or NaCl experienced the same dynamic time effect. After a certain time and due to gravity, the pendant drop broke loose from the syringe tip, generally before the IST steadied. The measured IST right before the breaking point has been used to calculate the IST decrease rate. The result is presented in table 5.3.

The result (in table 5.3) shows that the IST for all samples decreases with time. An IST equilibrium value for each sample is difficult to estimate, but it should be around the IST equilibrium value for pure dist. water, 30.7 mN/m. The IST decrease rate, V_I, ranges from 0.009 (dist. water w. 5 mM NaCl & 0.5% laponite) to 0.168 mN/m·s (dist. water w. 1% Na-Fh). Some of the measured pendant drops broke loose from the syringe tip after just a few minutes due to a drop density increase as clay from the syringe sank and sedimentet in the drop bottom. This made the measurements challenging and the errors larger than what is tabulated in table 5.3. The measurement errors and the large difference in measurement duration make it difficult to conclude whether V_I is affected by clays or/and NaCL, or not. More data and longer measurement durations are needed. What we can conclude for sure, is that the IST exposed to hexane oil, decreases with time. The behavior was not further examined. There is probably some surface active molecules/particles in the hexane oil that interact with the drop. It would be beneficial to investigate this further by repeating the measurements and using different surrounding liquids. The result also highlights that one has to be careful when calculating IST with Antonoff's rule. The rule does not take surface interactions into account and should only be used as an estimate.

The decrease in SST with time, as seen in figure 5.14, was observed with the pendant drop method as well. Figure 5.16 shows how the SST changes with time for an evaporating pendant drop exposed to air and made of distilled water with and without Na-Fh or Triton X-100 surfactant. Firstly, look at the difference in SST between dist. water with (triangle) and without (rectangle) Na-Fh clay. The SST for the pendant drop with clay decreases much faster than the SST for the drop without clay. The explanation is simple. Clay particles from the syringe sink and sediment to the drop bottom and result in a density (ρ) increase. This was evidently observed on video clips. As presented in equation 4.2, the calculated SST (γ) depends on ρ. The drop shape changes when ρ increases due to gravity. The computer software calculates γ based on the drop shape and ρ. Since the real ρ value is larger than initially defined, the calculated γ becomes smaller than what it really is. Since we cannot measure ρ continuously during the experiments, dynamic SST measurements are not possible for pendant drops with clay particles.

Table 5.3: Measured interfacial surface tension (IST) of a pendant drop in hexane oil right after it was made (IST_i) and right before it broke lose from the syringe tip (IST_e). All samples are measured at room temperature (23 °C). * Indicates that the sample is preheated to 70 °C before cooled down and measured at room temperature.

Dist. water w.	Duration (s)	IST_i (mN/m)	Error	IST_e (mN/m)	Error	Rate (mN/m·s)	Ratio
0% clay (pure dist. water)	240	40.11	0.54	30.72	0.63	0.039	1.00
0.25% laponite	210	40.86	0.98	37.16	0.32	0.018	0.45
1 mM NaCl & 0.5% laponite	150	39.82	1.71	37.17	0.88	0.018	0.45
1 mM NaCl & 1% Na-Fh	90	39.76	0.87	36.84	0.13	0.032	0.83
5 mM NaCl & 0.5% laponite	240	38.64	0.70	36.59	0.45	0.009	0.22
5 mM NaCl & 1% Na-Fh	90	40.20	2.92	35.25	0.59	0.055	1.41
1% Na-Fh	20	42.04	0.23	38.69	0.64	0.168	4.28
0.5% Na-Fh	26	37.89	0.28	35.65	0.39	0.086	2.20
1.5 % Na-Fh	36	39.34	0.70	34.12	0.46	0.145	3.71
2.0 % Na-Fh	30	37.95	1.30	34.93	0.67	0.101	2.57
1.5% Na-Fh*	240	40.44	0.46	34.45	0.43	0.025	0.64
2% Na-Fh*	60	38.31	1.55	37.41	0.41	0.015	0.38

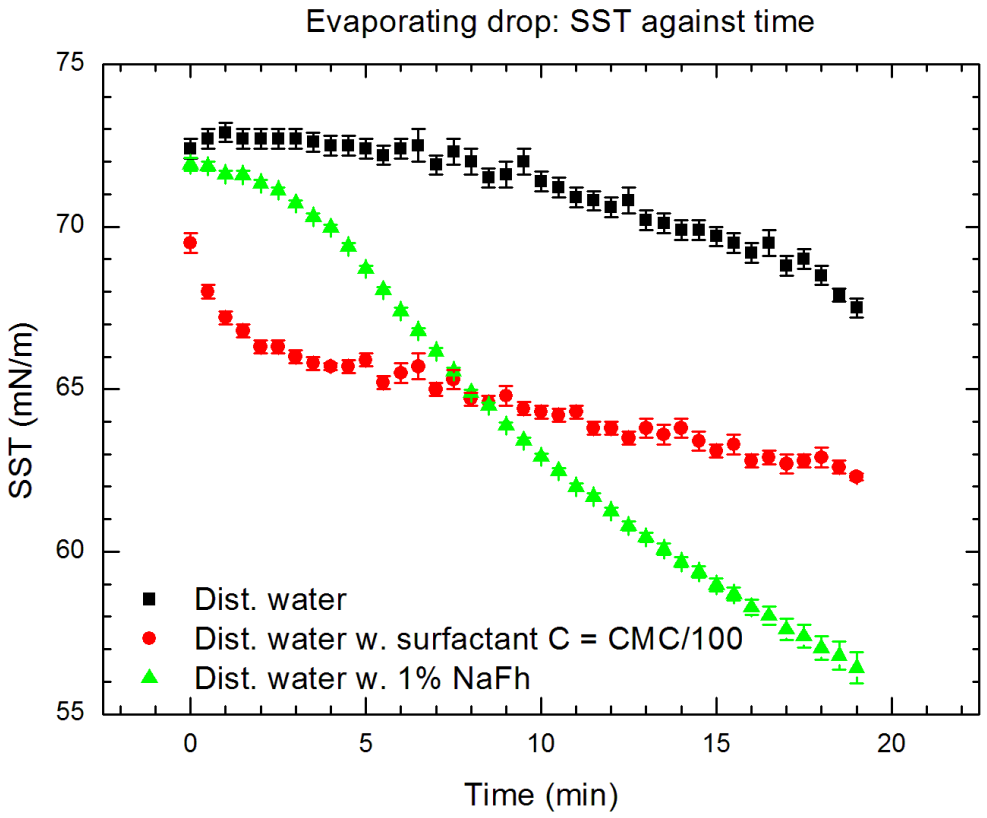

Figure 5.16: Dynamic SST of an evaporating pendant drop exposed to air and made of distilled water with and without Na-Fh or Triton X-100 surfactant.

The distilled water with Triton X-100 surfactant drop (circle in figure 5.16) did not experience any considerable density changes during the measurements. The SST for the pendant drop with surfactant decreases from $\sim$ 70 to 62 mN/m in 20 minutes, while the SST for the drop without surfactant decreases from $\sim$ 73 to 67 mN/m in the same time. Besides the first five minutes, the SST decrease rate is approximately the same for the two drops.

One might ask why the SST of pure distilled water changes with time. The reason is probably small dust particles from the surroundings which settle on and interact with the drop surface. As time goes on, more dust particles are deposited on the drop surface, the volume of the evaporating drop decreases ($\sim$ 25 - 17 μL during 20 min.) and the drop surface area becomes smaller. In other words, the density of dust particles on the drop surface increases with time. Another reason might be that the precision of the pendant drop instrument decreases when the drop becomes smaller and more spherical. An image of the distilled water pendant drop right after and $\sim$ 20 min. after it was made is shown in figure 5.17.

The SST of the pendant drop with Triton X-100 surfactant decreases rapidly the first five minutes after it was made, before it decreases with approximately the same rate as the drop without surfactant. This behavior is peculiar and might be explained by measurement errors. It may also be a surfactant effect since the surfactant concentration inside the drop increases as the drop evaporates. However, this should not result in a fast SST decrease the first five minutes, but rather during the entire experiment. More measurements are needed to understand and explain this behavior. Additional graphs are left for the appendix (section C).

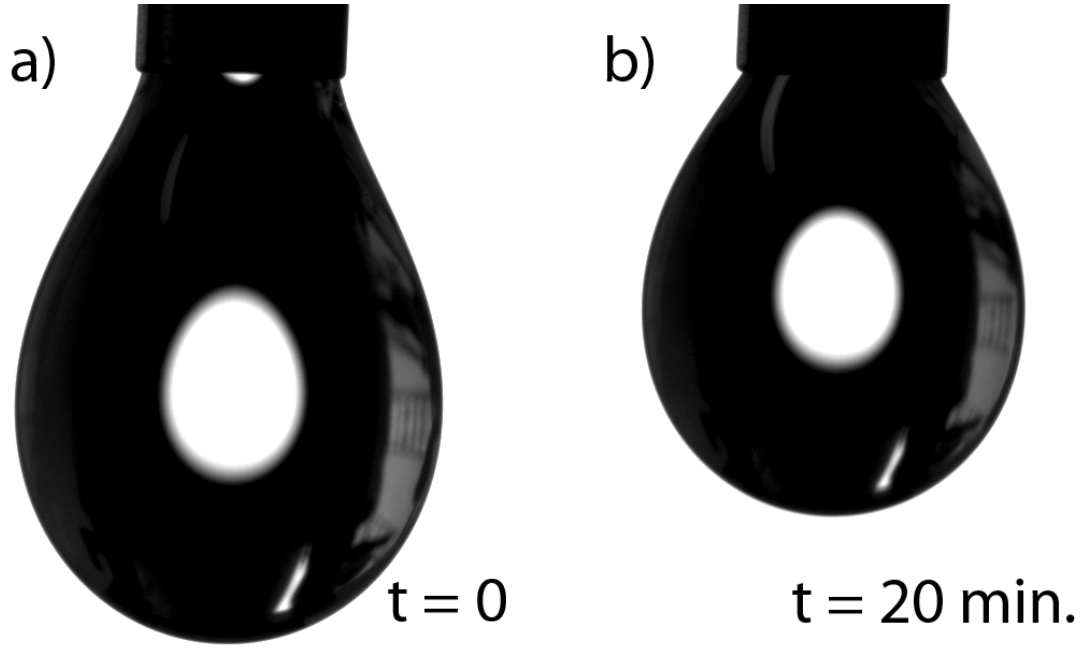

Figure 5.17: An evaporating distilled water pendant drop exposed to air a) right after the drop was made and b) $\sim$ 20 min. later.

5.9 Drop length measurements

The results from the SST measurements at PUC suggest that clay type and concentration (Φ) affect the surface tension of water, while the measurements performed at Uppsala suggest the opposite. Water contamination or interaction with the Du Noüy ring may have been the decisive difference. However, microfluidic flow experiments were performed at PUC based on the SST measurements performed there. The interfacial surface tension (IST), σ, between OP3 mineral oil and water with or without clay is yet to be measured. Antonoff's rule was employed to calculate the different ISTs instead. As highlighted in the previous section, the rule will only serve as a good estimate for the IST.

Seven different systems were chosen for the mirofluidic flow experiments. OP3 mineral oil was selected as the dispersed phase in all systems, while distilled water with different concentrations of clay particles was used as the continuous phase. The selection of clay type and concentration was based on the SSTs measurements presented in section 5.7. The systems and their properties are presented in table 5.4.

As explained in section 2.12, the relative effect of viscous forces to IST forces is given by the capillary number Ca. This important dimensionless number distinguishes the different droplet formation regimes and is given by: $Ca = u\mu/\sigma$, where u is the characteristic velocity (m/s), μ the dynamic viscosity (Pa·s) and σ the IST (N/m) between the dispersed and continuous fluid. The maximal $Q_{\max}$ and minimum $Q_{\min}$ total flow rate used in the flow experiments were 0.21 and 0.07 ml/h, respectively. We know that:

1 ml = 1×10^{-3} l = 1×10^{-3} l · 10^{-3} m^3/l = 1×10^{-6} m^3
1 h = 1 h · 60 min/h · 60 s/min = 3.6×10^{3} s
100 μm = 1×10^{2} μm ·10^{-6} m/μm = 1×10^{-4} m

The maximum and minimum flow velocity are then:

$$v_{\max} = \frac{Q_{\max}}{A} \approx \frac{0.21\text{ ml}}{(100\,\mu\text{m})^2\text{ h}} = \frac{21\times10^{-8}\text{ m}^3}{3.6\times10^{-5}\text{ m}^2\text{s}} = \frac{21\text{ m}}{3600\text{ s}} \approx 5.83\times10^{-3}\text{ m/s} \qquad (5.6)$$

$$v_{\min} = \frac{Q_{min}}{A} \approx \frac{0.07\text{ ml}}{(100\,\mu\text{m})^2\text{ h}} = \frac{7\times10^{-8}\text{ m}^3}{3.6\times10^{-5}\text{ m}^2\text{s}} = \frac{7\text{ m}}{3600\text{ s}} \approx 1.94\times10^{-3}\text{ m/s} \qquad (5.7)$$

where A is the microchannel cross section area. The dynamic viscosity ν_d equals the kinematic viscosity ν_k multiplied by the specific mass ρ. Using $\nu_k = 1$ mm^2/s = 1×10^{-6} m^2/s and $\rho = 1$ g/ml = 1×10^{3} kg/m^3 give $\nu_d = 1\times10^{-3}$ Kg/s·m. The maximum and minimum ISTs from table 5.4 are 38 and 18 mN/m, respectively. It is then easy to calculate the capillary number, which yields: $Ca_{\max} = 3.2\times10^{-4}$ and $Ca_{\min} = 5.0\times10^{-5}$. With the capillary number well beneath 0.01 for all systems and flow rates, the droplet formation is in the squeezing regime (see section 2.12.1).

Table 5.4: Flow systems and their properties. Antonoff's rule are used to calculate the interfacial surface tensions (IFTs). * signifies that the sample has been preheated to 70 °C.

System	Phase	Fluid	Kin. visc. (mm^2/s)	Specific mass (g/ml)	SST (mN/m)	IST (mN/m)
N1	Disp.	OP3 Mineral Oil	3.40	0.7860	24.8	
	Cont.	Distiled water	0.98	0.9980	63.7	38.9
N2	Disp.	OP3 Mineral Oil	3.40	0.7860	24.8	
	Cont.	D. water w. 0.1% laponite		0.9985	59.6	34.8
N3	Disp.	OP3 Mineral Oil	3.40	0.7860	24.8	
	Cont.	D. water w. 0.25% laponite		0.9990	54.6	29.8
N4	Disp.	OP3 Mineral Oil	3.40	0.7860	24.8	
	Cont.	D. water w. 1.0% laponite	1.28	1.0026	63.1	38.3
N5	Disp.	OP3 Mineral Oil	3.40	0.7860	24.8	
	Cont.	D. water w. 2.0% bentonite		1.0073	42.6	17.8
N6	Disp.	OP3 Mineral Oil	3.40	0.7860	24.8	
	Cont.	D. water w. 1.5% Na-Fh*		1.0029	40.2	15.4
N7	Disp.	OP3 Mineral Oil	3.40	0.7860	24.8	
	Cont.	D. water w. 2.0% Na-Fh*		1.0104	66.6	41.8

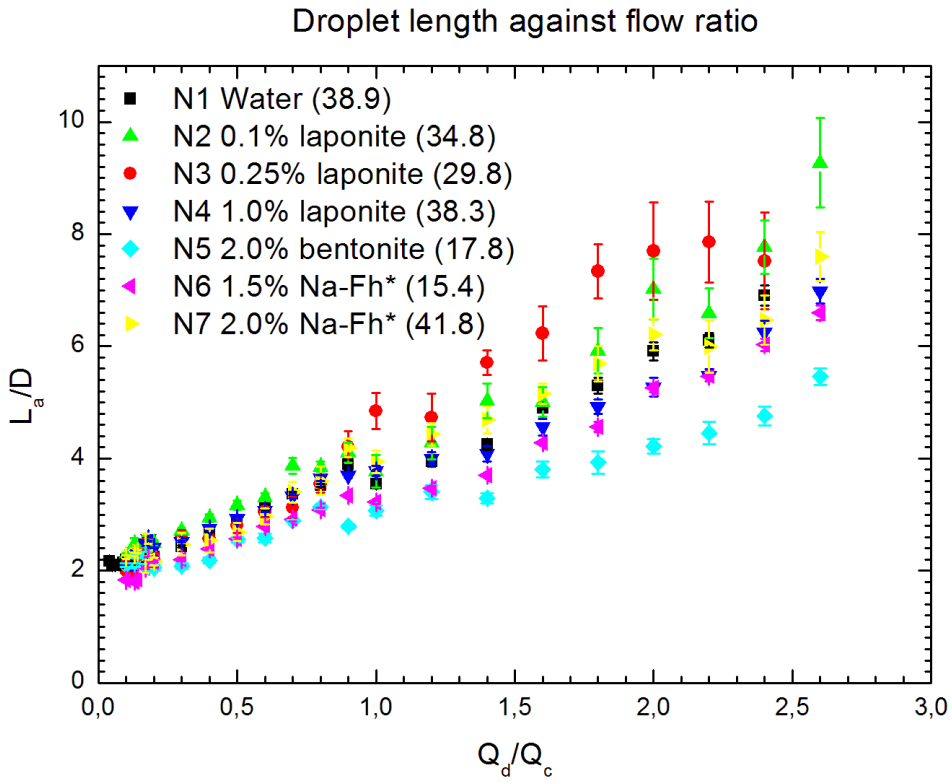

Figure 5.18: Average droplet length L_a divided by the microchannel diameter D against discontinuous/continuous flow rate ratio $Q_\mathrm{d}/Q_\mathrm{c}$ for the different systems. The numbers in the parenthesis are the calculated theoretic interfacial surface tension (ISTs) between the cont. and discont. phase. * Signifies that the sample has been preheated to 70 °C.

The length of droplets formed in the microfluidic T-junction, L, was measured for different discontinuous/continuous flow ratios and fluids. The average droplet length (L_a) against flow ratios $Q_\mathrm{d}/Q_\mathrm{c}$ for the seven systems is presented in figure 5.18. Error bars are calculated from the standard deviation in measured droplet length. The variation in L_a between the seven systems measured at the same flow ratio is large, especially for large $Q_\mathrm{d}/Q_\mathrm{c}$ ratios (> 1).

Systems that contain clay particles seem to form droplets with larger or lower L_a than the system without clay (system N1) when the flow rate ratios are similar. The average droplet lengths produced by system N1 (square), lying in the middle of the data points in figure 5.18, appear to be close to the average droplet length of all the other systems (figure 5.19).

The two figures indicate that clay particles in the continuous phase, depending on concentration (Φ) and clay type, have the ability to increase or decrease the droplet length produced in a microfluidic T-junction. In figure 5.18 and for all measured flow ratios, one sees that the systems with lowest ISTs, N5 (tilted square) and N6 (tilted triangle) produce droplets with shortest L_a. The effect of IST on L_a will be discussed in more detail later in this chapter.

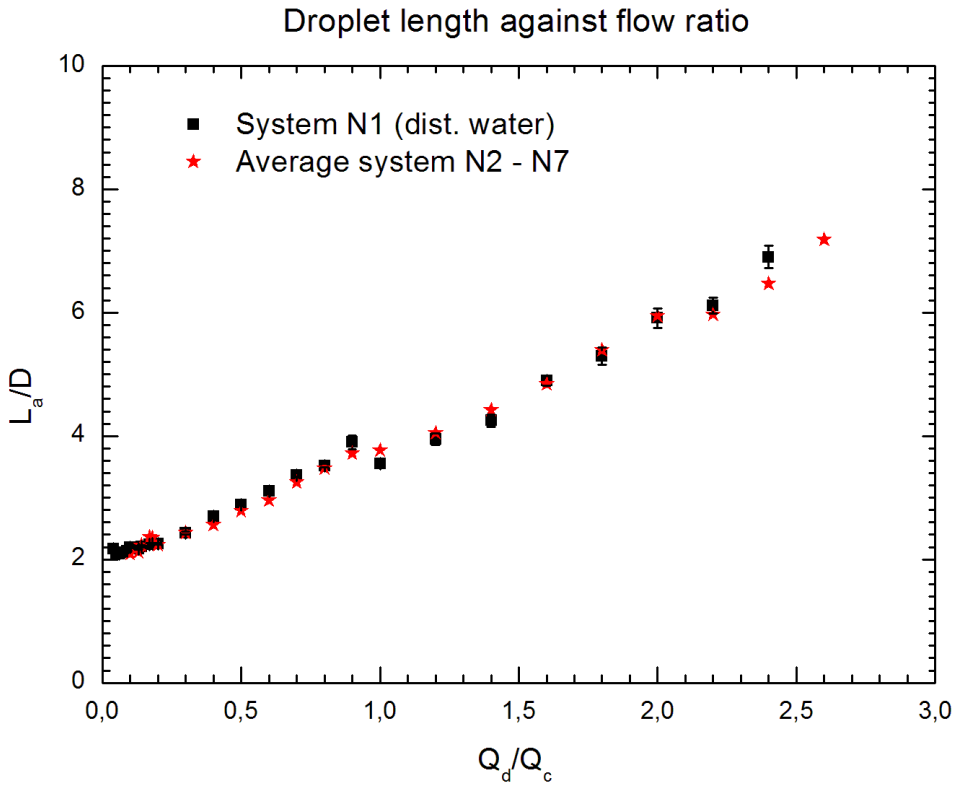

Figure 5.19: Average droplet length L_a divided by the microchannel diameter D against discontinuous/continuous flow rate ratio $Q_\mathrm{d}/Q_\mathrm{c}$ for system N1 and the average of system N2 - N7.

As presented in section 2.13, the scaling law for the droplet size in the squeezing regime predicts that L/D decreases with an increase in Ca and is almost independent of fluids properties:

$$L/D = \epsilon + \delta \frac{Q_d}{Q_c} \tag{5.8}$$

where L is the droplet length, D is the microchannel diameter, ϵ and δ are fitting parameters depending on the geometry of the T-junction, while Q_d and Q_c are the flow rate of the dispersed and continuous phase, respectively. The data points in figure 5.18 are fitted with this model and the result with parameters is presented in table 5.5. Standard errors of the average lengths calculated for each system at the different Q_d/Q_c flow ratios are used to weight the different data points in the fit.

Table 5.5: Linear fit for the different systems: $L_a/D = \epsilon + \delta \cdot \mathbf{Q_d/Q_c}$. R is the correlation coefficient ($R = 1$ indicates a perfect fit between the data points and the model, while $R = 0$ signifies no fit at all) and SD is the standard deviation in L_a from the model.

System	ϵ	ϵ_{Error}	δ	δ_{Error}	R	SD
N1	1.966	0.004	1.810	0.016	0.989	3.433
N2	2.071	0.022	2.162	0.062	0.991	1.065
N3	1.751	0.048	2.556	0.097	0.964	1.671
N4	2.048	0.009	1.710	0.023	0.986	2.809
N5	1.966	0.016	1.205	0.024	0.957	3.328
N6	1.674	0.007	1.687	0.012	0.989	4.711
N7	2.026	0.019	1.962	0.055	0.987	1.297

The high correlation coefficient (R close to 1) and the small errors in ϵ and δ for all the systems indicate that the model fits well to the measured data points. ϵ and δ for the different systems ranges from 1.67 - 2.07 and 1.21 - 2.56, respectively. The standard deviation (SD) represents the spread in L_a from the fitted model. As seen in the table above, the SD between the systems differs much. System N2 and N6 display two extremes in variation from the fit with SD = 4.71 for system N6 (1.5% NaFh*) and SD = 1.07 for system N2 (0.1% laponite). Comparing with literature, Garstecki et al. (2006), Tice et al. (2003) and Xu et al. (2008) reported scaling laws as:

$$L/w = 1 + Q_d/Q_c$$
$$L/w = 1.9 + 1.46Q_d/Q_c$$
$$L/w = 1.38 + 2.52Q_d/Q_c$$

These scaling laws have ϵ and δ values between or close to the geometry fitting parameter ranges presented in the paragraph above. However, these scaling laws were obtained by using rectangular microchannels and dist. water and oil as the continuous and discontinuous phases. For oval microchannels, more of the continuous phase will contribute to the drop neck squeezing and shorter droplets are formed (see section 2.13.4). The large difference in ϵ and δ between the systems indicates that clay type and concentration somehow affect the average droplet length and variation.

5.10 Surface tension effect

Let us now take a closer look at how the interfacial tension between the liquids affects the droplet length and variation. Figure 5.20 shows the average droplet length L_a against different flow rates Q_d/Q_c for continuous phases with or without laponite clay. The x axis in the figure is logarithmic to better present the flow ratio range, and the data points in the figure have error bars based on the SD from L_a. For low flow ratios ($Q_d/Q_c < 1$), the measurement error is low, i.e. the measured drop lengths L does not vary much from L_a. The average droplet lengths for these low flow rate ratios are approximately the same for the systems with laponite (N2-4) and without clay particles (N1). L_a is $\sim$ 2-3 times the microchannel diameter D when $Q_d/Q_c < 1$.

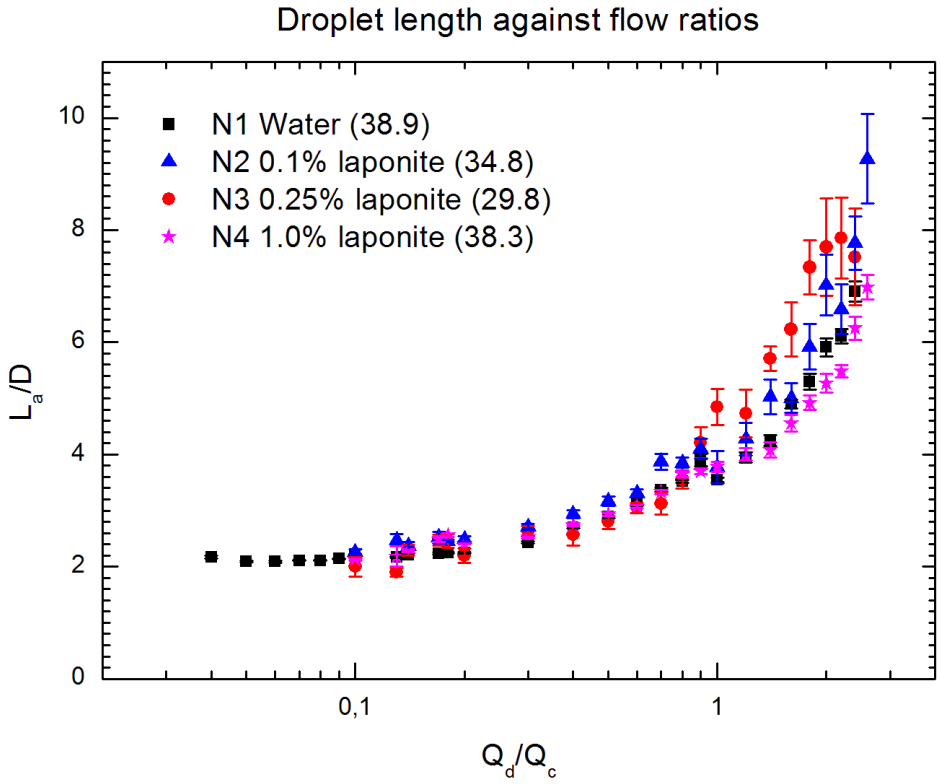

Figure 5.20: Average droplet length L_a divided by the microchannal diameter D against different flow rate ratios Q_d/Q_c for dist. water with and without laponite clay particles. The numbers in the parenthesis are the calculated theoretic interfacial surface tension (ISTs) between the cont. and discont. phase.

When Q_d/Q_c increases, the variation in L from L_a increases drastic for the systems containing water with laponite (N2-4). Displayed in the figure, the error bars for the system with distilled water (square) are much smaller than the error bars for the systems with laponite. These huge variations in measured droplet lengths (L) from L_a make it difficult to draw certain conclusions about how the laponite clay concentration Φ_l affects L. It seems that system with $\Phi_l = 0\%$ (square) and $\Phi_l = 1\%$ (star) produce shorter droplets (in average) than the system with $\Phi_l = 0.1\%$ (triangle) and $\Phi_l = 0.25\%$ (circle). By comparing the theoretic interfacial surface tensions

(ISTs), one discovers that the systems with the highest IST between the liquids are the systems that generate the longest droplets. However, the difference in theoretic IST between the systems is not huge. The difference in La between the systems is therefore not expected to be large. It is also important to remember that the calculated theoretic IST values are only estimates of the real ISTs. We do not know how the OP3 mineral oil interacts with the distilled water drop surface. As mentioned before, there is also doubt about the validity of the surface tension values measured with the Du Noüy ring method.

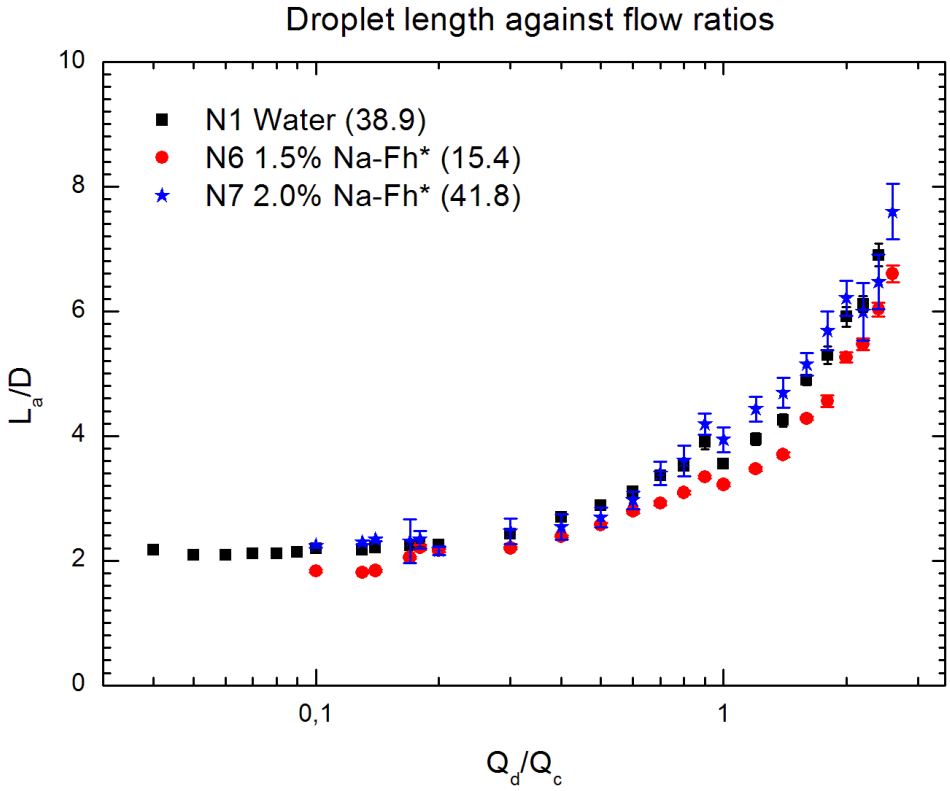

Figure 5.21: Average droplet length L_a divided by the microchannel diameter D against different flow rate ratios $Q_\mathrm{d}/Q_\mathrm{c}$ for dist. water with different Na-Fh concentrations. The numbers in the parenthesis are the calculated theoretic interfacial surface tension (ISTs) between the cont. and discont. phase. * Signifies that the sample has been preheated to 70 °C.

A graph displaying L_a/D against different flow ratios $Q_\mathrm{d}/Q_\mathrm{c}$ for systems with different Na-Fh clay concentrations Φ_n is presented in figure 5.21. System N7 with $\Phi_n = 2\%$ Na-Fh (star) and high IST produce longer droplets (in average) than system N6 with $\Phi_n = 1.5\%$ Na-Fh (circle) and a considerably lower IST. Both system N6 and N7 have a continuous phase that was pre-heated to 70 °C. As discovered and presented in section 5.7, these fluids displayed a decrease in the superficial surface tension (SST) with time (see figure 5.14). The difference in calculated theoretic IST between the two systems is enormous. This huge difference is not reflect in La, which only differs slightly. The difference in L_a for low flow rates ($Q_d/Q_c < 1$) between the systems with Na-Fh (N6 and N7) and the system without clay (N1) is in reality zero.

For increased flow rates, the variation in L from L_a increases slightly for the system containing distilled water with $\Phi_n = 0\%$ (square) and 1.5% Na-Fh (circle), while the variation for system N7 with $\Phi_n = 2.0\%$ (star) is much larger. This might be explained by the SST time dependence presented earlier in figure 5.14. For (pre-heated) dist. water with $\Phi_n = 2.0\%$, the measured SST decreased considerably with time compared to the SST for (pre-heated) dist. water with $\Phi_n = 1.5\%$. However, the time scale for these dynamic effects (minutes) was much longer than the time scale for droplet formation in the microchannel (seconds). One must also consider the fact that this dynamic SST effect was measured when exposed to air, while the droplets make interfacial surfaces in oil. Clay particle sedimentation and error in the flow rates may also affected L_a. Compared to the systems containing dist. water with different laponite concentrations (as shown in figure 5.20), the error bars are lower for the systems containing Na-Fh. This indicates that systems containing Na-Fh produce droplets with less variation in measured droplet lenght L from L_a than systems containing laponite. However, the difference in variation is small.

The system containing dist. water with bentonite (N5) produced the shortest droplets of all systems (figure 5.18). However, the real droplet bentonite concentration Φ_b was not equal to the initial mixed 2% concentration. This is because the bentonite grains were large and heavy, and they sank rapidly the the bottom of the horizontal syringe. These bentonite grains stayed at the syringe bottom while the fluid was pumped to the microchannel. During the measurements, we also had some problems caused by bentonite particles essentially blocking the microchannels at the T-junction. The last problem in particular may have affected the result and shortened the droplets. The standard deviation (SD) values for the system with bentonite (N5) is quite small, so the produced droplets do not vary much in length for the different flow rate ratios.

The results presented in this chapter do not show any evident relationship between the measured droplet length and the interfacial surface tension (IST). The experiments show that clay particles affect the average produced droplet lengths, but it is hard to explain precisely how they do this. If we can trust the SST measurements performed at PUC with the Du Noüy ring method and if Antonoff's rule is accurate, the clay particles may change the IST between the OP3 mineral oil drop and the surrounding water. Water contamination may also play an important role. Another possibility is that clay particles do not alter the surface tension, but somehow stick to the microchannel or droplet wall and thus alter the geometry and pressure. Campos (2011) examined the same system, but without clay. For similar viscosity and flow rates, he observed an increase in droplet length when the IST between the fluids increased. This behavior was also expected by theory and earlier work presented in section 2.13.3. Campos (2011) also found that L/D cannot solely be described by the flow rate ratios $Q_{\mathrm{d}}/Q_{\mathrm{c}}$. The size of the individual flow rates will also affect the droplet length.

5.11 Time effect on droplet length

For some of the systems in table 5.4, L_a/D has been measured at both the T-junction and the microchannel exit (table 5.6). A picture of the droplets at the T-junction was captured every five seconds for one minute, giving 11 pictures. The camera and microchip were then adjusted and 11 new pictures were captured at the exit of the microchip. The flow rate ratio between the continuous and discontinuous phase Q_d/Q_c was equal to 1 for every measured system. The droplet length on the pictures was then measured with the computer program AxioVision. The formed droplets measured at the T-junction are not exactly the same droplets that were measured at the microchip exit. This should not be a problem since the variation in measured droplet length L is quite small (see SD in table 5.6). A picture of the droplets right after they were made in the T-junction and near the microchip exit is displayed in figure 5.22.

The channel length from the T-junction to the chip exit is approximately 278 mm (The Dolomite Centre). With a flow rate equal to 0.05 ml/h for both the continuous and discontinuous phase, the droplet speed is found by using equation 5.6 which relates the flow rate and speed of the droplets in the microchannel: $v \sim 10$ m/3600 s = 0.0028 m/s = 2.78 mm/s. One can then easily calculate the droplet travel time between the T-junction and chip exit; t $\sim$ 278 mm / 2.78 mm/s = 100 s.

The average droplet length divided by the microchannel diameter (L_a/D) for all the measured systems in table 5.6 seems to be smaller at the chip exit than at the chip T-junction. The difference $(L_a/D)_T - (L_a/D)_E$ is considerable for system N2, N4 and N6 with $Q_d/Q_c = 1$. For system N7, the difference is not big enough to exceed the standard error of the mean (SEM). The result suggests that during the approximately 100 seconds during which the droplets are traveling in the microchannel, the average length of the droplets L_a decreases. Unfortunately no similar measurements were performed with system N1 (distilled water without clay particles), so one cannot conclude whether the effect is caused by clay particles in the droplets or something else.

Table 5.6: Average droplet length L_a divided by the microchannel diameter D for different systems measured at the microchip T-junction (T) and exit (E). SD is the standard deviation in measured droplet lengths L divided by D from L_a/D, while SEM is the standard error of the mean. The flow rate ratio is $Q_d/Q_c = 1$ for all systems.

System	$(L_a/D)_T$	SD_T	SEM_T	$(L_a/D)_E$	SD_E	SEM_E
N2	3.72	0.40	0.12	2.90	0.69	0.21
N4	3.70	0.19	0.06	2.60	0.06	0.02
N6	3.15	0.12	0.03	2.43	0.13	0.04
N7	4.05	0.90	0.27	3.95	0.67	0.20

The standard deviation (SD) of the measured droplet lengths divided by D ranges from 0.06 to 0.90 for the various systems when $Q_d/Q_c = 1$, so the variation in droplet lengths differs between the systems. This time effect was just briefly examined, so no major conclusion can be drawn. To achieve better statistics and credibility, the same measurements should be performed at different flow ratios Q_d/Q_c and preferably with a larger selection of measured droplet lengths. Similar measurements should be performed for the distilled water system (N1) as well.

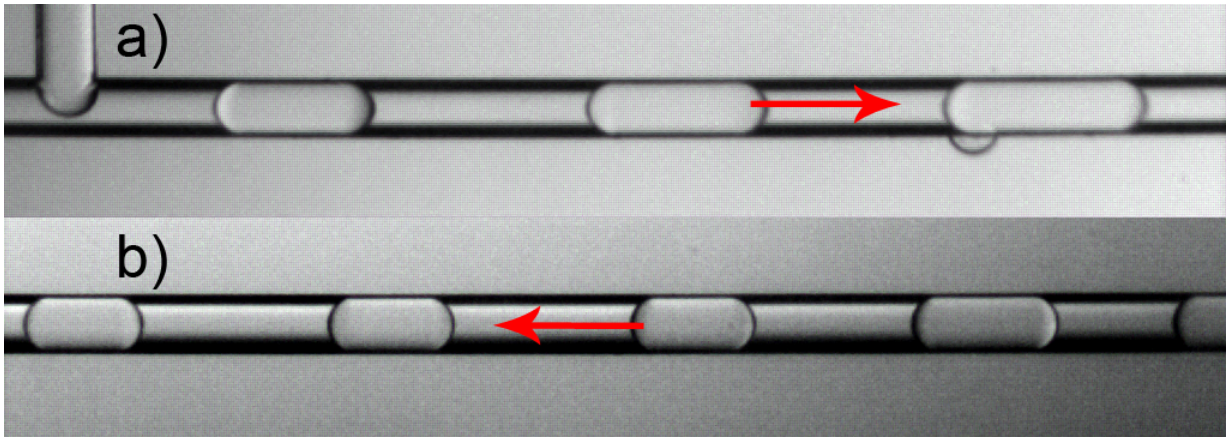

Figure 5.22: System N2: Picture of (a) droplets formed near the T-junction and (b) droplets leaving the microchip.

Chapter 6

Conclusion

6.1 E-field induced formation of chain and ribbon pattern

Droplets made of silicone oil and sodium fluorohectorite (Na-Fh) clay particles suspended in castor oil and affected by various electrical fields (E-fields) have been studied. Zero field experiments showed that the clay particles altered the drop settling velocity. The settling velocity in castor oil for a silicone oil droplet with 1% Na-Fh (w/w%) was approximately 2.3 times faster than the settling velocity for a pure silicone oil droplet. Using Stoke's law and taking droplet radiuses into account, the droplet without clay particles was expected to sink 1.7 times faster than the drop with clay particles. The distinciton may be explained by a difference in the drag force F_d acting on the droplets. If that is the solely explaination, calculations indicate that the stress exerted by the surrounding castor oil on the silicone oil droplet is reduced by a factor $\sim$ 1.8 when 1% Na-Fh clay particles are added.

Two optical microscopes with optical paths normal to one another were used to study the E-field induced structuring from clay particles placed inside the droplet. This configuration allowed for simultaneous observation of the droplet and clay behavior from both a front view (optical path perpendicular to the E-field direction) and a side view (optical path parallel to the E-field direction). Prior to the application of the E-field, the Na-Fh particles are randomly dispersed inside (and on the surface of) the silicone oil droplet. The initial isotropic distribution in zero field was confirmed by adjusting the focus on the microscope and examining the intersection between the clay particles and the focus plane. The application of an alternating current (AC) E-field of 600 V/mm peak to peak (frequency 200 Hz) resulted in a prolate droplet deformation and chain patterns parallel to the E-field direction were formed. Only the E-field strength E was observed to affect the chain formation. Larger E reduced the chain pattern completion time.

Direct current (DC) E-field initiated clay particle movement inside the drop and the formation of a ribbon pattern at the drop surface. The ribbon is composed of short particle chains oriented along the E-field direction. The droplet experienced an oblate deformation and moved slowly and horizontally towards the positive electrode when the DC field was applied. Why the drop is negatively charged is yet not understood, but it may be caused by a very weak droplet

rotation. Droplet rotation was evidently observed when the DC E-field strength exceeded $\sim$ 300 V/mm. This phenomenon was not examined in detail, but it seemed to resemble the rotation described by Quincke (1896) with tilted deformation axes and rotation perpendicular to the E-field direction. Also in accordance with Quincke (1896), the tilt angle of the droplet deformation axes was found to increase with stronger E-field strengths.

As the droplet moved horizontally, the formed ribbon was slightly displaced in the opposite direction of the drop movement. This is likely a drag caused effect. In addition to horizontally drop movement, viscous flow inside and outside the drop was induced when the DC E-field was applied. The induced flow was predicted by Taylor (1966) in his leaky dielectric model to balance the electric force caused by free charges in the droplet (see section 2.4). The flow inside and outside the droplet was traced by capturing video clips and by observing the movement of clay particles or latex beads. Both the flow inside and outside the droplet displayed the same characteristic pattern as Taylor described in his leaky dielectric model (Taylor, 1966). The clay particles and dielectric latex beads used for the tracing produced the same flow lines. The resemblance in flow lines strongly indicates that the induced viscous flow inside and outside the drop is unaffected by the clay particles and their interactions.

A more detailed study of the ribbon formation showed that the clay particles undergo a "V" $\rightarrow$ "Y" $\rightarrow$ "I" transition before completing the ribbon pattern. The transition is probably present due to the settling speed of the drop and gravity effects. By varying the DC E-field strengths, experiments showed that the time for ribbon completion t is proportional to $cE^{-2.4}$, where c is a constant. So a stronger E-field results in less time for clay particles to form the ribbon pattern. Experiments with different droplet sizes were also performed. The results shows that the percentage of droplets to form ribbons in 1 minute has a aE^2 linear dependence, where a is the drop radius. The correlations seems reasonable since the drop deformation and viscous flow are proportional to aE^2 (Taylor, 1966). The ribbon formation is thus assumed to be highly dependent on the induced viscous flow velocity inside the drop.

The application of both an AC and a DC E-field resulted in clay particle movement and formation of chain patterns inside the droplet. As confirmed by (among others) Fossum et al. (2006), the clay particles become polarized and attach to each other when the E-field is applied. The initial isotropic clay distribution ensures that the chains spread evenly throughout the drop. As time evolves, more particles become attached to each other (forming chains). Induced viscous flow inside the drop is the factor that distinguishes the drop and particle behavior in the two experiments. For an AC E-field, the E-field direction changes at a rate given by the field frequency. It has been shown that the viscous flow processes in a droplet are slow compared to the the dielectric polarization of the fluid (Vizika and Saville, 1992).

When the frequency is high enough, the E-field changes too fast for viscous flows to arise. In that case, interfacial tension is the only force to balance the drop deformation caused by induced dipole charges on the drop surface. The dipole charges are pulled towards their respective electrodes and the drop is thus stretched towards the electrodes giving a prolate deformation. As stated in equation 2.15, the drop deformation depends on the squared E-field, so the field direction should not alter the prolate deformation. Inside the droplet, the clay particle attraction is too strong and the frequency of the field is too high for the particles to rotate with the

alternating field and break free from the chain pattern. When there in addition is no viscous flow to break the chains, the patterns stay stable.

When a DC E-field is applied, viscous flow inside and outside the droplet have more than enough time to appear and to balance the electric forces caused by the free charges inside the drop. The induced viscous flow limits the size of the aligned chains and thus prevents the chains from forming throughout the whole drop. Instead, the short chains align in a ribbon pattern. It is not completely understood why the particles move to the drop surface and form the ribbon pattern there. The centrifugal force arising from the circular flow inside the droplet may be one reason. We recall from section 2.4 and figure 2.6 that the tangential electric stress and thus the viscous flow at the droplet equator is zero since no free charges exist there. This explains why a ribbon is allowed to form and stay at the droplet equator without being destroyed.

6.2 Future work

Some suggestions for future studies have already been mentioned earlier in this thesis report. The experiments presented here are mostly performed with Na-Fh clay particles. Other clay types and oils should be tested as well. It was weakly observed and it is expected that droplets with a high clay particle concentration need less time to form a ribbon than droplets with lower clay concentrations. However, there was not sufficient time to investigate this in the present study. The clay concentration effect on ribbon completion time and ribbon width would be an interesting study for future works.

Some of the experiments, such as measurements of the settling velocity, should be repeated with other clay concentrations and types to confirm and control that clay particles reduce the drag force on settling droplets. The sample cell used for the experiments involving E-fields was custom-made and optimized for the set up with two microscopes. An improvement for later experiments would be to increase the sample cell height. A greater height would increase the time before the droplets sink to the sample cell bottom, and would improve the homogeneity of the E-field acting on the droplets[1]. It would also be beneficial to flip the electrodes so that they are in direct contact with the castor oil. This would most likely change/increase the castor oil flow.

It could be advantageous to change the experimental setup. A good idea would be to design a spherical sample cell so that the microscope/s could have any desired optical view between the view parallel and perpendicular to the E-field. Instead of examining the droplets from the sides of the sample cell, a view from above may be a clever solution.

As mentioned earlier, a rotation phenomenon was observed when the applied E-field exceeded a critical value. A detailed study of this phenomenon with clay particles inside the droplet could include: finding the the critical E-field value for Quincke rotation (Quincke, 1896) and comparing it with values and models from the literature, investigating and explaining the drop movement towards the positive electrode, checking if the drop always rotate in a direction perpendicular to the E-field, studying if clays affect the tilt angle and mapping the flow inside

[1]The E-field is only homogeneous in the middle half of the sample cell (Sato et al., 2006).

and outside the drop for different E-fields. New flow measurements could be improved by using a better light source (e.g. a laser sheet) and a dark background. Using μ-PIV (Particle image velocimetry), as described in the report in appendix E, may also be a solution. The experiments presented in this thesis report only studied single droplets. Studying systems with several droplets containing clay particles may be the natural next. The ultimate goal should be to control the clay (alignment and movement) and droplet behavior (deformation, position, rotation, coalescence, etc.) for several drops (forming emulsions) at the same time.

6.3 Two phase flow experiments

The stability and length of oil-water droplets with smectite clay particles formed in an oval microfluidic T-junction and by using the cross-flow shear method have been studied at PUC-Rio[2]. Seven different systems were examined and compared with OP3 mineral oil as the dispersed/discontinuous phase and distilled water with different clay particle concentrations as the continuous phase. The calculated capillary number Ca for the fluids was as expected, well beneath 0.01. The low Ca number places the droplet formation in the squeezing regime, indicating that droplets are sheared off right at the T-junction and that the breakup is dominated by the interfacial tension force.

The length of the droplets formed at the microfluidic T-junction, L, was measured for different dispersed/continuous flow rates and systems. For each flow rate ratio $Q_\mathrm{d}/Q_\mathrm{c}$[3], an average droplet length (L_a) was calculated from 11 measurements. The data points were then plotted and fitted with: $L_a/D = \epsilon + \delta \cdot \mathrm{Q_d/Q_c}$[4], where D is the microchannel diameter and ϵ and δ are fitting parameters depending on the geometry of the T-junction. The measured data points fitted well with the model indicating that the droplet length is proportional to the flow rate ratio $Q_\mathrm{d}/Q_\mathrm{c}$. ϵ and δ for the different systems ranged from 1.67 - 2.07 and 1.21 - 2.56, respectively. The values are in accordance with earlier work in the literature (Tice et al., 2003; Garstecki et al., 2006; Xu et al., 2008).

The large variation in ϵ and δ between the systems indicates that clay type and concentration somehow affect the average droplet length (L_a). For small flow rate ratios ($Q_d/Q_c < 1$), all systems produce more or less equal droplet lengths and the lengths increase linearly with Q_d/Q_c. At these flow ratios, the variation in measured droplet length (L) from the calculated average droplet length (L_a) is very small, i.e. the systems are stable and produce droplets with approximately the same lengths. A difference in the average droplet length L_a between the systems starts to arise when $Q_d/Q_c > 1$. However, the droplet length variation also increases when $Q_d/Q_c > 1$ and the measurement errors almost erase the difference in L_a between the systems. It is thus difficult to conclude whether clay particles in the dist. water systematically affect the formed droplet lengths or not. Anyhow, the droplet length variation is generally observed to increase when clay particles are added to the continuous phase (dist. water).

[2]Pontifícia Universidade Católica do Rio de Janeiro.

[3]Q_d and Q_c are the flow rate of the dispersed and continuous phase, respectively.

[4]This model was proposed by Garstecki et al. (2006) for droplet formation in the squeezing regime.

For four of the systems, droplets were measured both at the T-junction and at the microfluid chip exit for $Q_d/Q_c = 1$. The average droplet length (L_a) for three of the four measured systems was considerably smaller at the chip exit than at the chip T-junction. The result suggests that during the approximately 100 seconds the droplets are traveling in the microchannel, the average length of the droplets decreases. Unfortunately, this time effect was just briefly examined and all of the measured systems contained clay particles, so one cannot conclude whether the effect is caused by clay particles in the droplets or something else. To achieve better statistics and investigate this phenomena, one should perform the measurement at different flow ratios Q_d/Q_c and preferably by measuring a larger selection droplets. Similar measurements should be performed with pure distilled water system as well.

To examine if clay particles can change the surface tension of water, the superficial surface tension (SST) against air for water with different clay types and concentrations was measured with the Du Noüy ring method at PUC-Rio. SST measurements of the distilled water used for the above described experiments revealed impurities in the water. The SST for the water against air was measured to 63.7 mN/m, while pure water has a water/air SST on the order of 70 mN/m. Measurements with the Du Noüy ring method showed that clay particles change the SST of the dist. water, but in an incoherent way. The measurements were therefore repeated, but in another lab (the Ångström laboratory in Uppsala) and by using the pendant drop method. As opposed to the dist. water at PUC, the water at the lab in Uppsala was perfectly pure, i.e. the SST was measured to 72.6 mN/m[5]. The SST measurements performed with the pendant drop method and *pure* distilled water did not show any correlation between clay[6] particle concentration and SST.

Since the distilled water at PUC and Uppsala had different degrees of purity, the two independent SST measurements are difficult to compare. We do not know if the water contamination discovered at PUC affects the clay particles and the SST in a distinct way. Capillary phenomena are very sensitive to impurities. For example, pure water has a water/air SST on the order of 70 mN/m, while ordinary tap water has a SST of no more than 40 mN/m (Tabeling, 2005). Even the presence of a thin layer of impurities can easily alter the energetic properties of the water surface. This was observed when time dynamic SST measurements of a pure dist. water pendant drop were performed. Small dust particles from the surroundings settled on the drop surface and slowly lowered the water/air SST. Repeating the SST measurements at PUC with the Du Noüy ring method and *pure* dist. water without impurities would probably give us some answers about if and how the water contamination interacts with clay particles. It is also possible that the clay particles interacted with the Du Noüy ring during the measurements. This might explain the observed incoherent SST and clay correlation.

The measurements performed with the Du Noüy ring method also revealed some time dynamic effects (the SST was observed to decrease with time, 10-20 minutes), but only for dist. water with Na-Fh that was preheated to 70 C°. Due to problems with clay particles that continuously increased the density of the pendant drop, time dynamic measurements was limited to a few minutes with the pendant drop method and no such effect was observed.

[5]72.8 mN/m is the tabulated water/air SST measured at room temperature.
[6]Laponite, bentonite and Na-Fh.

6.4 Future studies

As described above, the results presented in this thesis report are not evident enough for us to point out any systematic correlation between clay concentration and the length of droplets formed in the microfluidic T-junction. However, this does not mean that clay particles cannot affect the droplet length. There might be a question about time. The droplet lengths were mainly measured a second or less after the droplets were made at the T-junction. Similar measurements should be performed at the exit of the microfluidic chip to see if the clay particles need more time to affect the droplets. It takes $\sim$ 100 seconds from a droplet is formed till it exits the microfluidic chip. It could be advantageous to increase this time by using a chip with longer channel length.

For future work, it is highly recommended that the interfacial surface tension (IST) between the oil and water with clays is measured. We do not know how the surface tension of distilled water with clays behaves when exposed to oil instead of air. IST measurements between the OP3 mineral oil and water with clay particles was planned with the pendant drop method at Uppsala, but time and logistic problems forced us to use hexane oil instead. Hexane oil has many properties (e.g. viscosity, density, transparency and surface tension) which resemble the OP3 mineral oil, but there are probably some important differences at the molecular scale which we cannot predict. The pendant drop measurements showed that the IST between hexane oil and water with or without clay particles decreased with time. The behavior was not examined further, but the result shows that oil can contain surface active molecules/particles that interact with the drop and make the IST behavior too complex for it to be compared with the water/air SST. Future studies should also investigate whether water with different clay types and concentrations display some time dynamic SST or IST effects.

The set up and method used for the flow experiments worked well, but using syringe pumps with smaller injection rates would be an advantage for future studies. It is also suggested that a high speed video camera is used to record the droplets instead of capturing single images. In this experiment, mainly 11 droplet lengths were used to calculate the average droplet lengths at each flow rate. To achieve better statistics, the number of measured droplets should be increased significantly. For future work, it would also be of great interest to make emulsions with the T-junction geometry and study how the clay concentration affects the emulsion stability. It is expected that this method will produce stable pickering emulsions. One should also repeat the experiment with different fluids, T-junction geometries, and instead of varying the flow rate ratio Q_d/Q_c, one should investigate how the individual cont. and discont. fluid flow rates affect the droplet behavior.

Appendix A

Solution of the Laplace equation for a dielectric sphere

The derivation of a solution to the Laplace equation for a dielectric sphere follows Griffiths (1999) and Hersvik (2010). In spherical coordinates with a symmetry axis, the Laplace equation of equation 2.3 can be written:

$$\frac{\partial}{\partial r}(r^2\frac{\partial V}{\partial r}) + \frac{1}{\sin\theta}\frac{\partial}{\partial\theta}(\sin\theta\frac{\partial V}{\partial\theta}) = 0. \tag{A.1}$$

By separating the variables, we can express the potential as a product of two functions:

$$V(r,\theta) = R(r)\Theta(\theta). \tag{A.2}$$

Combining the two equations above and dividing by V, give:

$$\frac{1}{R}\frac{d}{dr}(r^2\frac{dR}{dr}) + \frac{1}{\Theta\sin\theta}\frac{d}{d\theta}(\sin\theta\frac{d\Theta}{d\theta}) = 0. \tag{A.3}$$

Since each term is independent of the other (ie. the first term depends on r while the second on θ), each term must be constant to satisfy the equation. We can therefore separate each term into two equations. The first term can be written:

$$\frac{1}{R}\frac{d}{dr}(r^2\frac{dR}{dr}) = l(l+1), \tag{A.4}$$

which has a solution

$$R(r) = Ar^l + \frac{B}{r^{l+1}}, \tag{A.5}$$

where A and B are arbitrary constants. The second equation becomes:

$$\frac{1}{\Theta\sin\theta}\frac{d}{d\theta}(\sin\theta\frac{d\Theta}{d\theta}) = -l(l+1), \tag{A.6}$$

which has one solution equal to the l'th Legendre polynomial in $\cos\theta$:

$$\Theta(\theta) = CP_l(\cos\theta), \tag{A.7}$$

where C is an arbitrary constant. The other solution to eq. A.6 for each l turn out to blow up at $\theta = 0$ and/or $\theta = \pi$. These components of the solution must always be set to zero when the z-axis is accessible (Griffiths, 1999). Combining the two solutions and absorbing constant C into A and B, the most general separable solution to the Laplace equation is:

$$V(r,\theta) = (Ar^l + \frac{B}{r^{l+1}})P_l(\cos\theta). \tag{A.8}$$

This yields an infinite set of solutions, one for each l. The general solution to the Laplace equation is a linear combination of the separable solutions:

$$V(r,\theta) = \sum_{l=0}^{\infty}(A_l r^l + \frac{B_l}{r^{l+1}}P_l(\cos\theta). \tag{A.9}$$

Inside the sphere, the sum over separable solutions that do not diverge is:

$$V_{in}(r,\theta) = \sum_{l=0}^{\infty} A_l r^l P_l(\cos\theta). \tag{A.10}$$

Outside the sphere we have a uniform field, boundary condition 2.6 and separable solutions that converge to zero at infinity which give us:

$$V_{out}(r,\theta) = -E_0 r\cos\theta + \sum_{l=0}^{\infty}\frac{B_l}{r^{l+1}}P_l(\cos\theta). \tag{A.11}$$

The boundary condition for continuous potential, eq. 2.4, requires that:

$$A_l a^l = \frac{B_l}{a^{l+1}}, \quad \text{for } \ l \neq 1, \tag{A.12}$$

$$A_1 a = -E_0 a + \frac{B_1}{a^2}, \quad \text{for } \ l \neq 1. \tag{A.13}$$

However, the boundary condition for the electric field perpendicular to the sphere surface, eq. 2.5, requires that

$$\epsilon_{in} l A_l a^{l-1} = -\epsilon_{out}\frac{(l+1)B_l}{a^{l+2}}, \quad \text{for } \ l \neq 1, \tag{A.14}$$

$$\epsilon_{in} A_1 = -\epsilon_{out}(E_0 + \frac{2B_1}{a^3}), \tag{A.15}$$

which give us the following constants:

$$A_l = B_l = 0, \quad \text{for } l \neq 1, \tag{A.16}$$

$$A_1 = -\frac{3E_0}{\epsilon_{in}/\epsilon_{out} + 2}, \tag{A.17}$$

$$B_1 = \frac{\epsilon_{in} - \epsilon_{out}}{\epsilon_{in} + 2\epsilon_{out}} a^3 E_0, \tag{A.18}$$

which give us the potential inside the sphere:

$$V_{in}(r,\theta) = -\frac{3E_0 r\cos\theta}{\epsilon_{in}/\epsilon_{out}+2}, \tag{A.19}$$

and outside the sphere:

$$V_{out}(r,\theta) = -E_0 r\cos\theta + \frac{\epsilon_{in}/\epsilon_{out}-1}{\epsilon_{in}/\epsilon_{out}+2}\frac{a^3 E_0,\cos\theta}{r^2} \tag{A.20}$$

where the second term in eq. A.20 is the potential from the induced dipole.

Appendix B

Ribbon formation plots

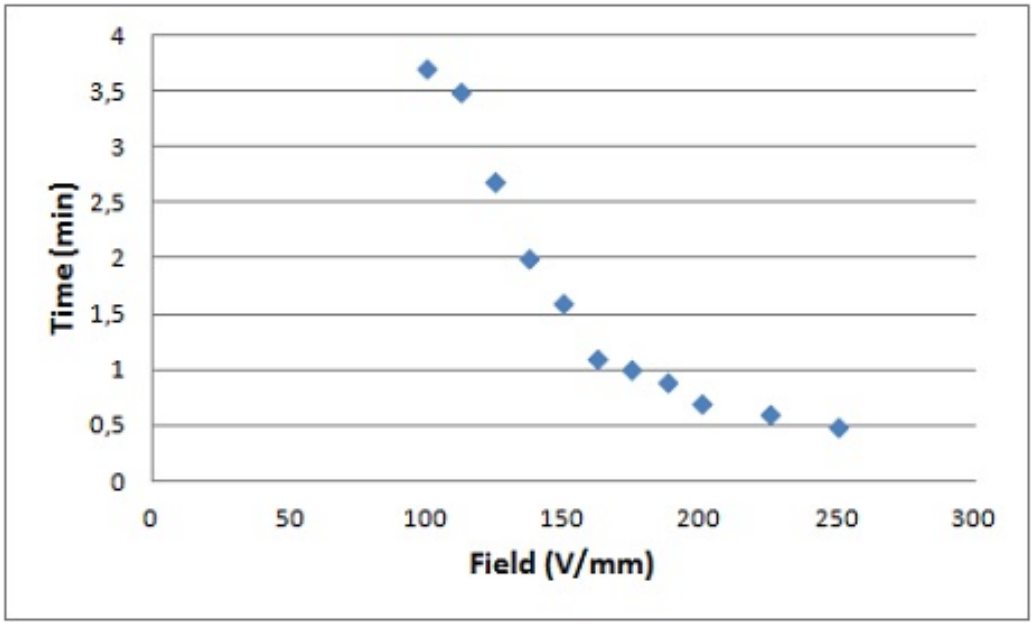

Figure B.1: Average time for ribbon to complete plotted agains different E-field strengths. Graph made by Knut Kjerstad.

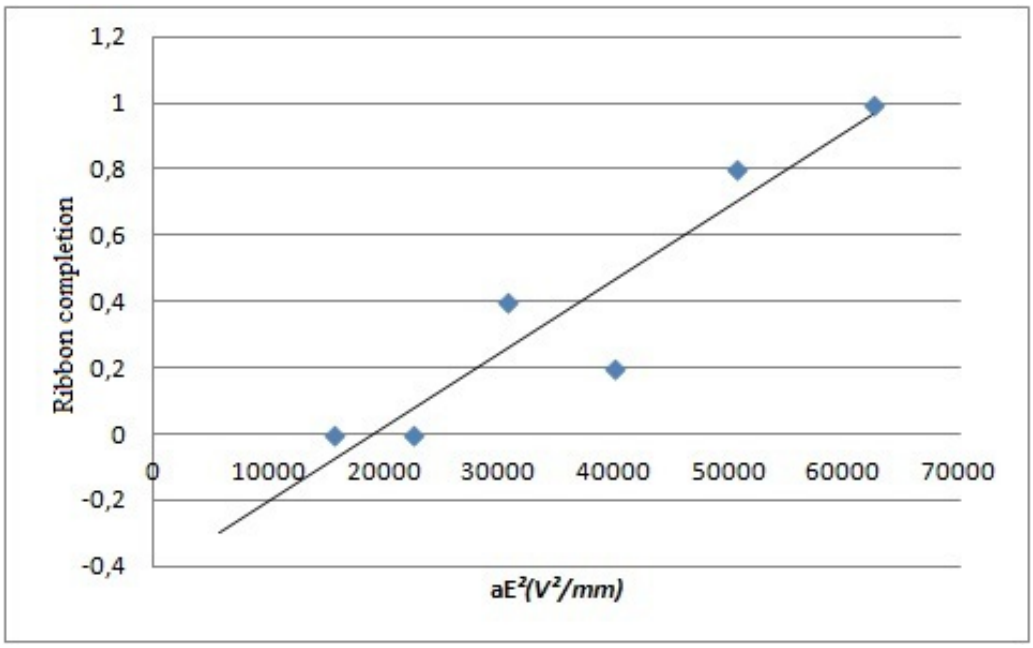

Figure B.2: Fraction of measured droplets to complete ribbon pattern in 1 min. plotted against aE^2. Drop size $\sim$ 0.5 μL. Graph made by Knut Kjerstad.

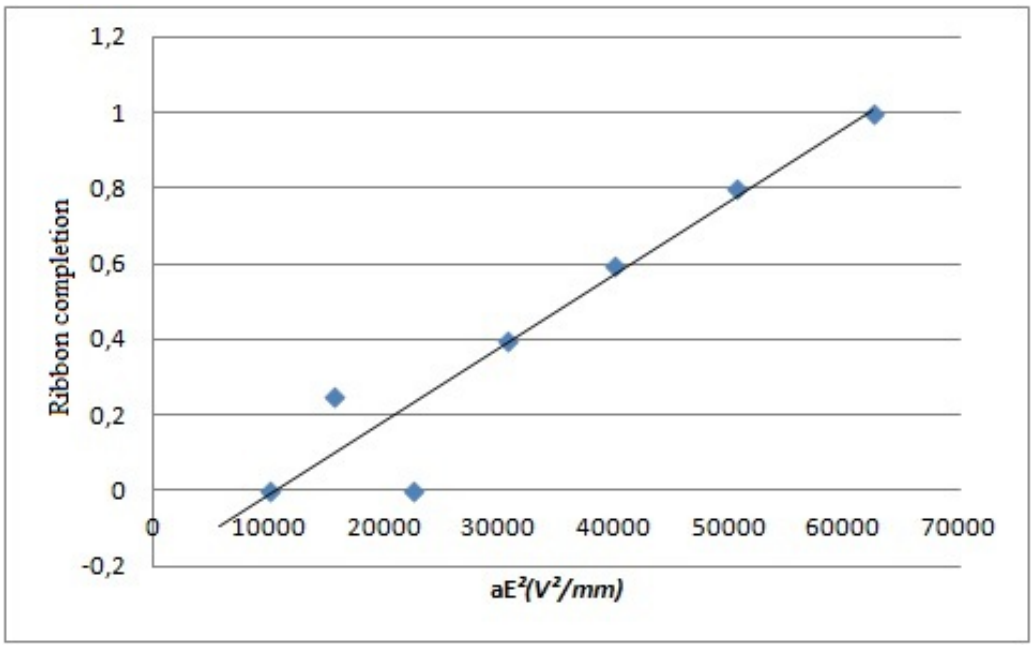

Figure B.3: Fraction of measured droplets to complete ribbon pattern in 1 min. plotted against aE^2. Drop size $\sim$ 1.0 μL. Graph made by Knut Kjerstad.

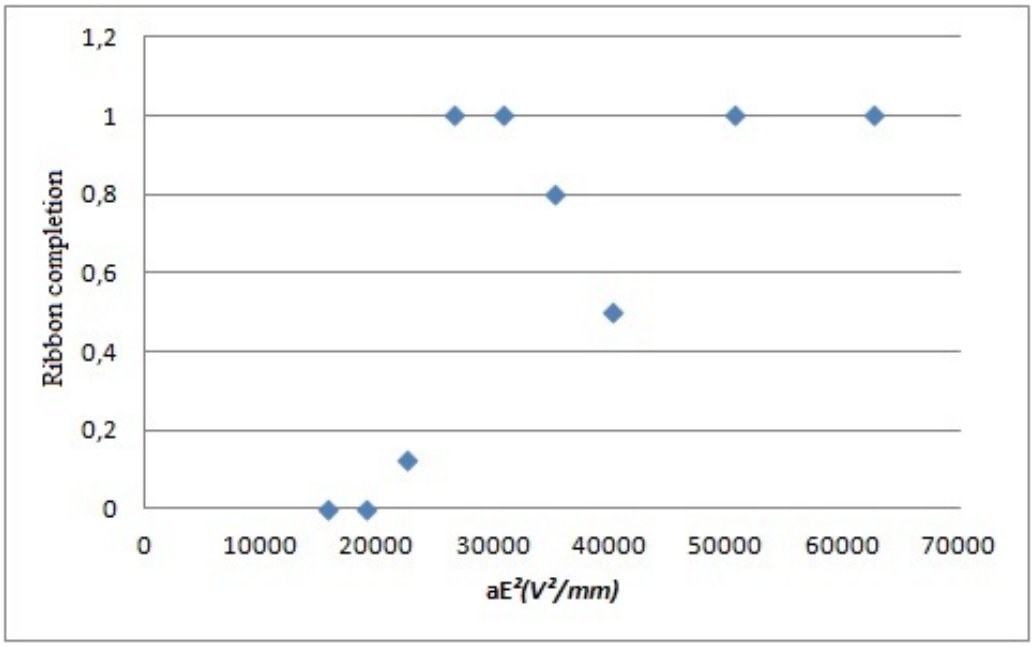

Figure B.4: Fraction of measured droplets to complete ribbon pattern in 1 min. plotted against aE^2. Drop size $\sim$ 2.0 μL. N.B, these data points have a larger source of error than the other plots presented here due to poor mixing of the clay particles in the silicone oil. The particle distribution around the ribbon was not even, and the particle size varied more than it should. Graph made by Knut Kjerstad.

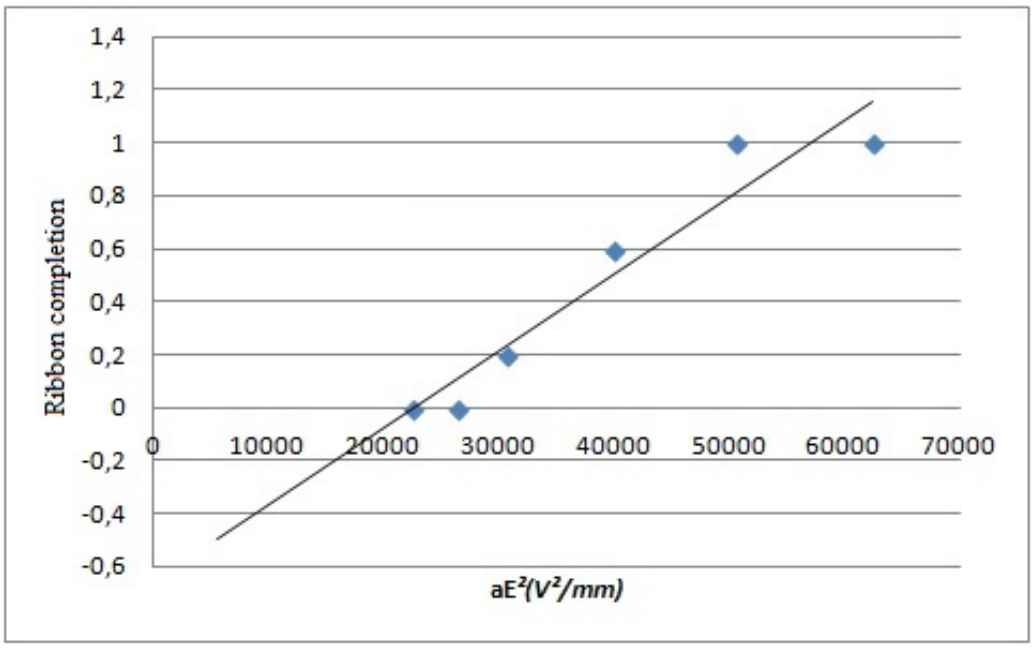

Figure B.5: Fraction of measured droplets to complete ribbon pattern in 1 min. plotted against aE^2. Drop size $\sim$ 3.0 μL. Graph made by Knut Kjerstad.

Appendix C

Additional graphs

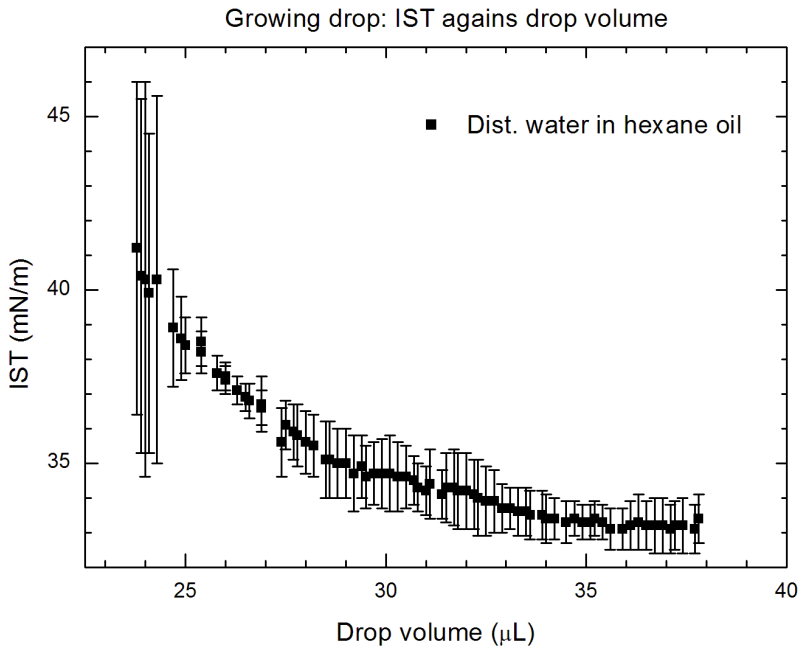

Figure C.1: Interfacial surface tension (IFT) of a distilled water pendant drop in hexane oil. The IST is measured while the drop is growing with approximately 0.1 μL/s till the breaking point is reached.

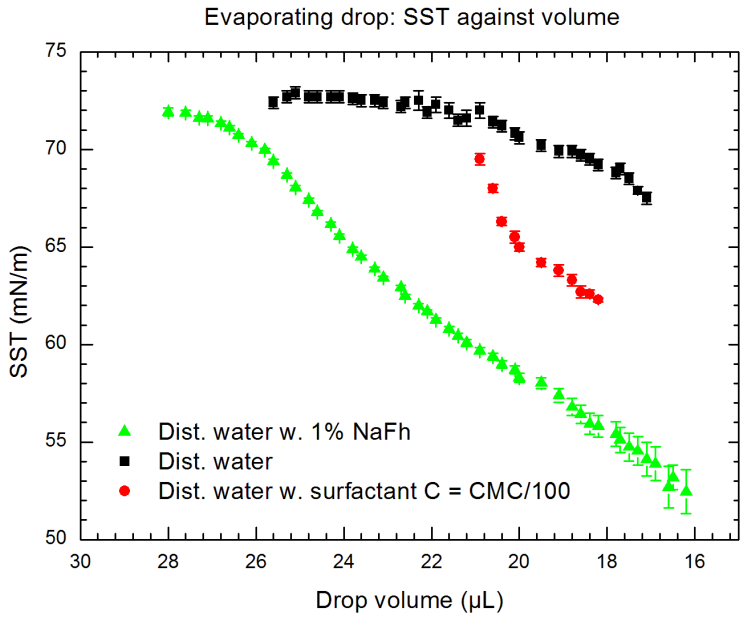

Figure C.2: Superficial surface tension (SST) of an evaporating pendant drop exposed to air and plotted against drop volume. Drop is made of distilled water with and without Na-Fh or Triton X-100 surfactant.

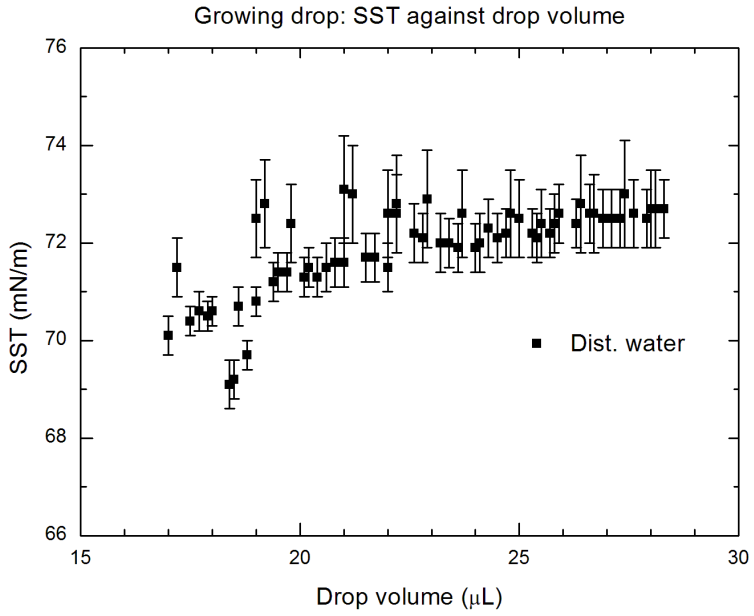

Figure C.3: Superficial surface tension (SST) of a distilled water pendant drop exposed to air. The SST is measured while the drop is growing with approximately 0.1 μL/s till the breaking point is reached.

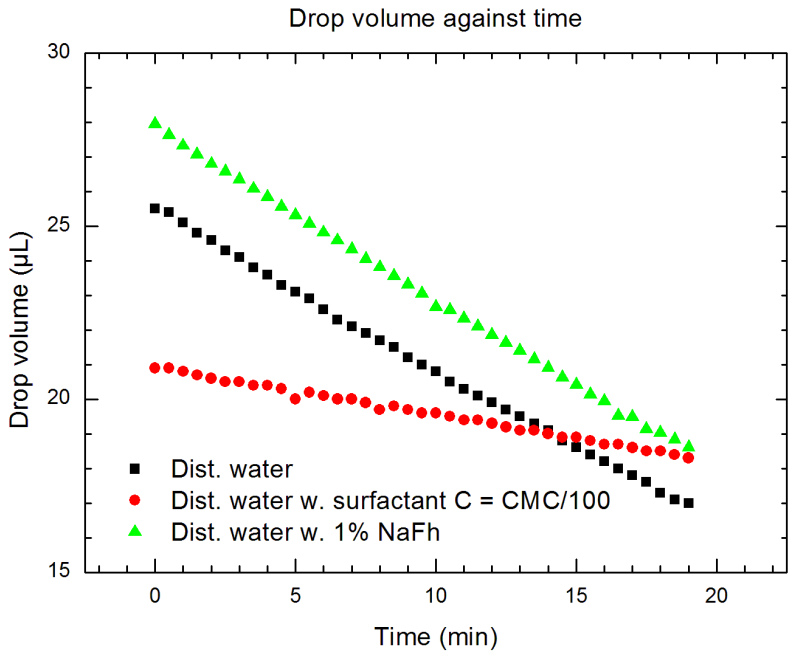

Figure C.4: Measured drop volume plotted against time for an evaporating pendant drop exposed to air and made of distilled water with and without Na-Fh or Triton X-100 surfactant.

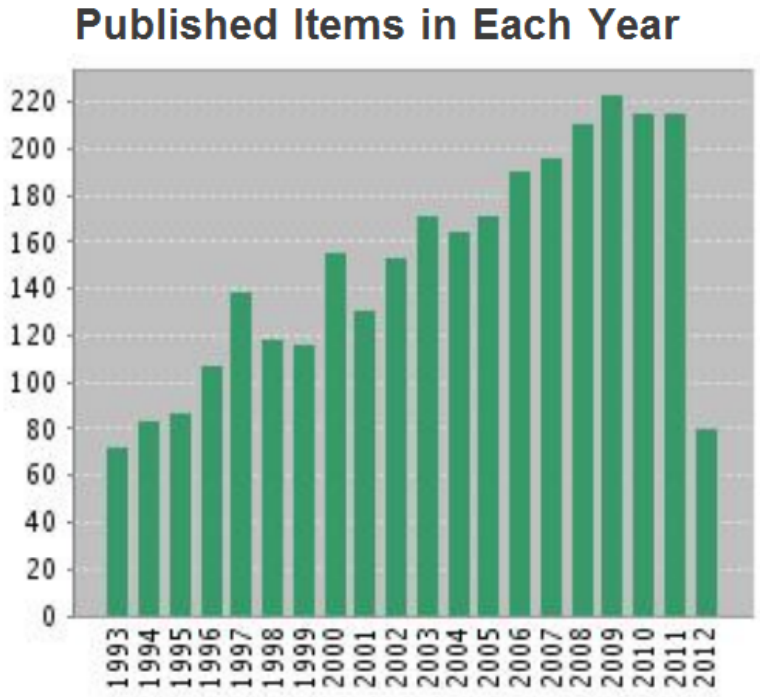

Figure C.5: Graph displaying number of "clay suspension" publications in each year. Graph from (of knowledge).

Appendix D

Contact angle measurements

In addition to the pendant drop surface tension measurements performed at the Ångström laboratory in Uppsala and described in section 4.4, droplet contact angles were measured as well. Samples were prepared by mixing Na-Fh powder with solutions of 1 mM NaCl before they were shaken in a mechanical shaker for about 80 minutes. With a uniform Na-Fh distribution, the samples were stored for several weeks to obtain a phase separation. The samples separated into an isotropic, a nematic and a sediment phase. After separation, the nematic and isotropic phases were extracted and stored in separate containers.

A OCA pendant drop tensiometer and the sessile drop method (see figure 4.6 a) were used to measure the contact angles. A 22 μL droplet was made and placed on a transparent glass plate on the sample stage. The camera and software settings were optimized before initiating the measurements. Pictures were captured and the dynamic contact angle measured every 30 seconds while the drop was evaporating. Figure D.1 and D.2 show the contact angles for different evaporating droplets plotted against time. It is important to highlight that the determination of contact angle is subjective since it is analyzed by human deduction or a software's own set of detection rules.

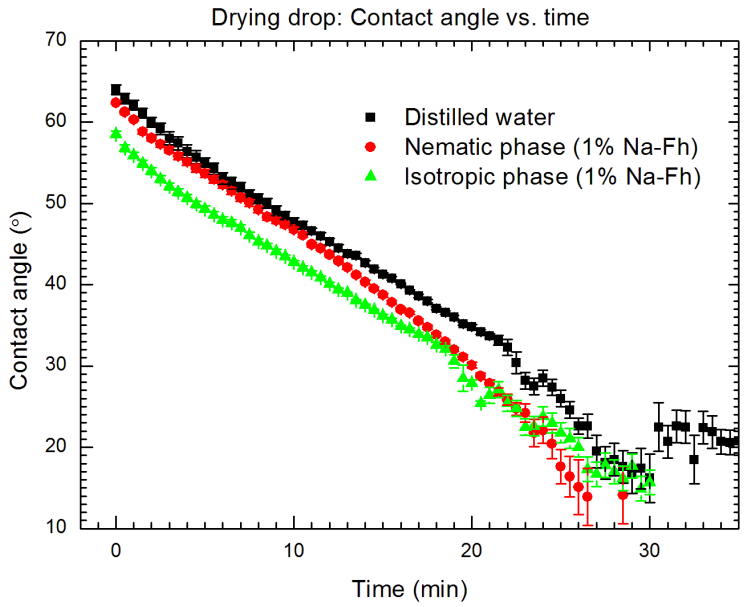

Figure D.1: Measured contact angle (CA) for an evaporating droplet made of distilled water and a nematic and an isotropic phase extracted from sample with 1% Na-Fh in a 1mM NaCl solution. The CA is a mean of the CA on the left and right side of the droplet.

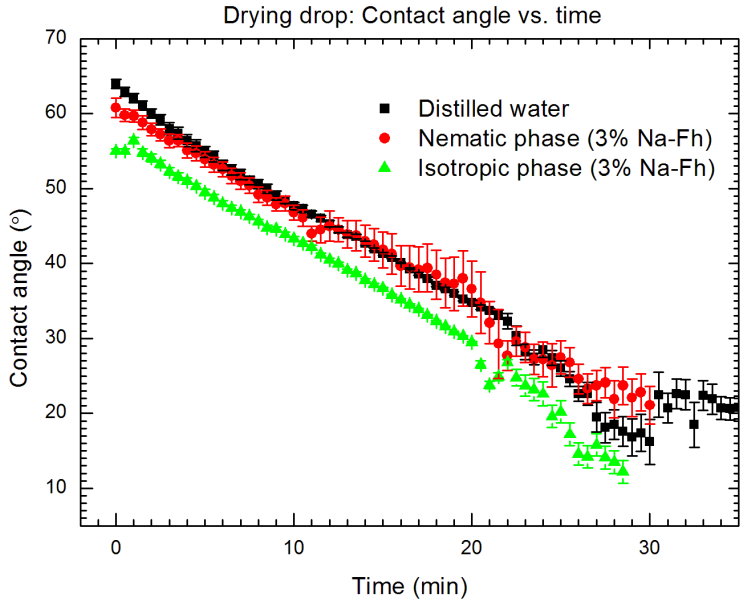

Figure D.2: Measured contact angle for an evaporating droplet made of distilled water and a nematic and an isotropic phase extracted from sample with 3% Na-Fh in a 1mM NaCl solution. The CA is a mean of the CA on the left and right side of the droplet.

Appendix E

Report: Micro-PIV Study

The two phase water-oil flow was studied with micro-PIV (particle image velocimetry) at PUC-Rio. The experiment is described and the results presented in the report on the following pages.

Pontifícia Universidade Católica
do Rio de Janeiro

μ-PIV study of oil-water droplet formation in microfluidic T-junction

Alexander Mikkelsen

May 15, 2012

Abstract

The report presents measurements of the flow field during the formation of oil droplets in a microfluidic T-junction together with detailed method and parameter description for optimizing a micro-PIV experiment. Using micro-PIV, velocities in an 100 μm elliptical T-junction were measured with a spatial resolution of 13 $\times$ 13 μm^2. An untraditional manual image selection technique and advanced processing parameters were used to analyze and measure velocity fields for different droplet grow stages. The report is written both to present the obtained result and also to help use the micro-PIV instrument and optimize the settings and setup in order to generate better velocity fields.

Contents

1 Theory

1.1 About Micro-PIV

Particle Image Velocimetry (PIV) is a well-known technique for measuring macro flow fields (field of view between 10 $mm \times 10$ mm - 1 $m \times 1$ m). In most applications, tracer particles are added to the flow and are small and light enough so that gravity effect can be neglected. For standard PIV experiments, laser light and optics are used to illuminate a plane in the fluid. The particles need to be illuminated and recorded at a short time interval. The displacement of the particles between the light pulses can be determined by evaluation of the PIV recordings (images). By making the laser light sheet very thin and by choosing a camera with adequate depth of field, all tracer particles will be in focus. All the other particles outside the light sheet are not illuminated and will thereby not scatter light and be seen in the recorded images.

This technique works well for studying macro flows, but when it comes to micro fluid flows, using the light sheet technique is impractical. The challenge is to make the light sheet thin enough relative to the small flow channel. In addition, the tracer particles are small compared to the wavelength of the illuminating light and will scatter less light. Episcopic illumination with fluorescent seed particles is a much better solution that overcomes the problems with the small scale. Episcopic illumination is reflected light imaging where the illumination light is transmitted through the objective. Instead of using a light sheet, a bigger volume of the flow is illuminated. The flow is seeded with fluorescent particles which absorb light at one wavelength and then emit light at a longer wavelength. The illumination light and its reflections from the particle's fluorescent emission are effectively removed by a dichroic mirror and barrier filter so that only the fluorescent emission of the particles reaches the camera.

1.2 Depth of Field

Depth of field is the range of distances through which objects may extend yet still remain well focused and form an acceptable image. In micro-PIV experiments the depth of field can drastically alter the image quality. High magnification and large lens apertures both decrease the depth of field. A decrease in the depth of field decreases the number of seeded particles in focus, but also increase the number of unfocused particles contributing to the background noise. Thus when decreasing the depth of field, one also has to decrease the number of seeding particles to maintain the same emitted fluorescent light to background noise ratio. However, in most cases increasing the magnification (and thereby decreasing the depth of field) is required to obtain the needed image. A compromise between desired magnification and degree of background light has to be made.

1.3 Fluorescent particles

Fluorescent particles undergo a fluorescent process where a fluorophore (or fluorescent dye), absorbs light at one wavelength and emits light at a longer wavelength. In this experiment powerful laser light emits photons (with wavelength 542 nm) that are absorbed by the fluorophore in the particles (micro spheres). The electronic state of the fluorophore is raised due to the absorbed energy. The excited state typically lasts for 1-10 nanoseconds. Within this time, some of the absorbed energy is dissipated due to some conformational changes happening in the fluorophore. Afterwards, the fluorophore returns to its base energy level by emitting a photon with less energy and therefor longer wavelength (612 nm). The whole process can be repeated unless the fluorophore has been damaged by photobleaching. Photobleaching happens when the fluorophore is exposed to high-intensity illumination over a long period and prevents the fluorophore from emitting light. However, the fluorescent particles may be run through the flow model many times before degradation is noticeable. According to the manufacturer sheet, the fluorescent particles should be stored in a refrigerator and not allowed to freeze. Keeping the fluorescent particles away from light will help preserve them.

Figure 1 shows the excitation and emission spectra for the fluorescent micro spheres used in the experiment. The excitation maximum is 542 nm and the emission maximum is 612 nm. The particles will be illuminated with 532 nm Nd:YAG lasers where the absorption efficiency is within 10 % of the 542 nm peak. The emission wavelength is between 545 and 780 nm. Fluorophore concentration, particle size,

illumination wavelength, pulse energy, pulse duration, filters and light environment will all affect the emission light level. In this micro PIV experiment, micro spheres with a maximized concentration of dye are being used. The pulse duration of the Q-Switched Nd:YAG lasers used for the experiment are fixed with a value between 3 and 10 *ns*. A fluorophore will then be able to go through 1-10 absorption-emission cycles during the laser pulse. This puts a maximum limit of fluorescent emission that can be realized from a laser pulse.

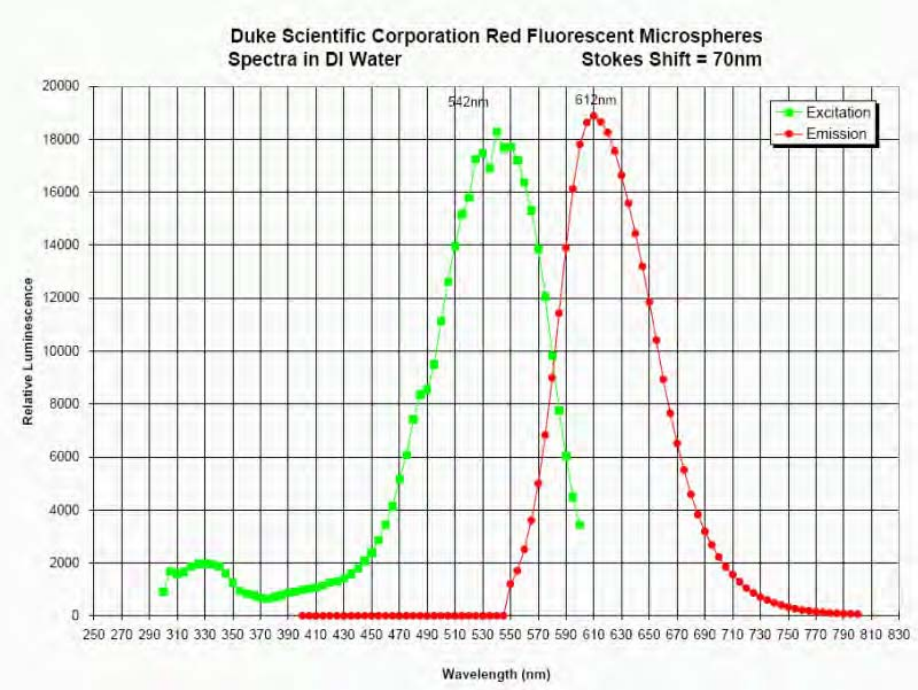

Figure 1: Figure of absorption - (green) and emission spectra (red) for the fluorescent micro spheres.

1.4 Filter Cube

For the micro-PIV experiment, a filter cube is needed to separate the scattered fluorescent light from the illuminating laser light. There are three light paths that can be traced through the filter cube: illumination light (2a), reflected light (2b) and fluorescent emission light (2c). The reflected laser light and the illumination light have the same wavelength (532 *nm*), while the fluorescent emission light has a longer wavelength (about 600 *nm*). The filter cube consists of a dichroic mirror that has a coating that reflects the laser wavelength and transmits the fluorescent emission wavelengths. For the illumination light it is a mirror and for the fluorescent emission it is a clear glass plate. Figure 3a shows an image of the filter cube used in the microscope.

1.5 White light illumination

In order to align the experiment with the filter cube in place, white light illumination is needed. The filter cube will only pass emitted fluorescent light with wavelengths in the orange specter, so by using the laser light (with wavelength 532 *nm*), an image will only be visible if there are fluorescent particles in the field of view. By using white light illumination, orange light can be imaged in reflection from the micro-capillary and setting up the experiment will be easier and safer. The micro-capillary can be seen even when fluorescent particles are not in place.

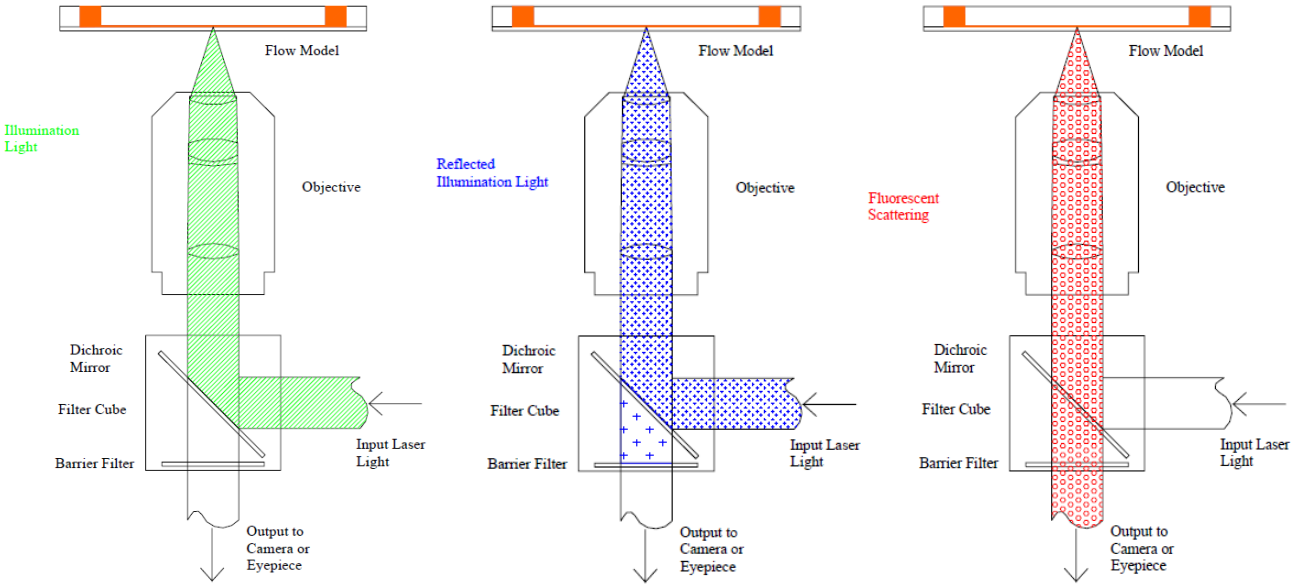

(a) Incoming laser light. (b) Reflected laser light. (c) Fluorescent scattering

Figure 2: The three different light paths traced through the filter cube: a) illumination light , b) reflected light and c) fluorescent emission light.

(a) Filter cube. (b) Microscope lens.

Figure 3

1.6 Image processing

1.6.1 Background subtraction

After the particle displacements are captured on images, processing is needed in order to produce vector fields. In this experiment the processing and evaluation was done with the computer software Insight 3G. Before evaluating and generating the correlation maps and vector fields from the captured images, a background subtraction may be performed to increase the signal to noise ratio and thereby the image quality. Two estimates of the background light level in the images are the generated minimum and average intensity images. The minimum intensity in the seeded area of the flow will be when a particle is not at a pixel location. When many images contribute to the minimum intensity image, an image without

seed particles will be generated. The minimum intensity image will not remove any of the intensity, but will allow some noise in the image. For the average intensity image, the opposite effect will occur. Both images are effective at finding stationary particles, walls, scratches and smudges in the micro-capillary contributing to the background noise.

1.6.2 Evaluation

The evaluation is initiated by dividing the digital image in small subareas named "interrogation areas". The smaller the size of the subareas, the better the vector field resolution. From the captured images of the tracer particles of the first and second illumination, statistical methods (auto- and cross-correlation) are used to calculate the local displacement vector for each interrogation area. In micro flows, the number of seed particles in each interrogation area is not sufficient for good correlation results using standard processing methods. In each recorded images there may be only a few or even no particles at an interrogation spot. To overcome this problem, ensemble correlation processing has to be used. Ensemble correlation processing takes advantage of the steady flow nature and uses many images to create a vector field. Instead of combining images as in standard PIV processing, the combination happens in the correlation maps. For the first image, the few particles present at the interrogation spots will correlate and contribute to the displacement peak, but the noise peak will be quite large. However, the signal to noise ratio in the correlation peak will increase as the correlation maps from more images are summed.

A more advanced and time consuming method is recursive ensemble processing. With recursive ensemble processing all of the images are processed with each processing pass. During the first pass, image displacements are measured and used to optimize the spot offsets. The first pass ensemble vector file is then used to optimize the spot offsets for the next processing pass. With a more precise spot offset, more particle pairs will be found and correlated, and recursive ensemble processing will thus be able to go to smaller spot sizes than classic PIV processing and increase the vector field resolution.

1.6.3 Post Processing

After the vectors have been extracted from the PIV images, post processing may be performed to edit vectors and compute flow properties. In most cases, vector editing is crucial since some vectors are generated from the wrong displacement peaks. By performing post processing, the different vectors can be considered valid or not by comparing the peak signal-to-noise ratio at each spot to defined threshold values. Selecting good threshold values are important to remove most of the bad points without eliminating too many of the good points. In post processing, the vectors are compared against the neighboring vectors. Vectors that vary by more than the validation tolerance from the neighborhood average are removed. Points that are empty can later be filled in by interpolating the neighboring vectors. With all the vectors in place, flow properties like vorticity, strain rates and velocity magnitude can be computed.

2 Experiment

2.1 Experimental setup

Figure 4 shows the experimental setup. The setup is composed of two systems: The liquid injection system and the μ-PIV system which includes the lighting equipment, visualization, image acquisition and the tracer particles.

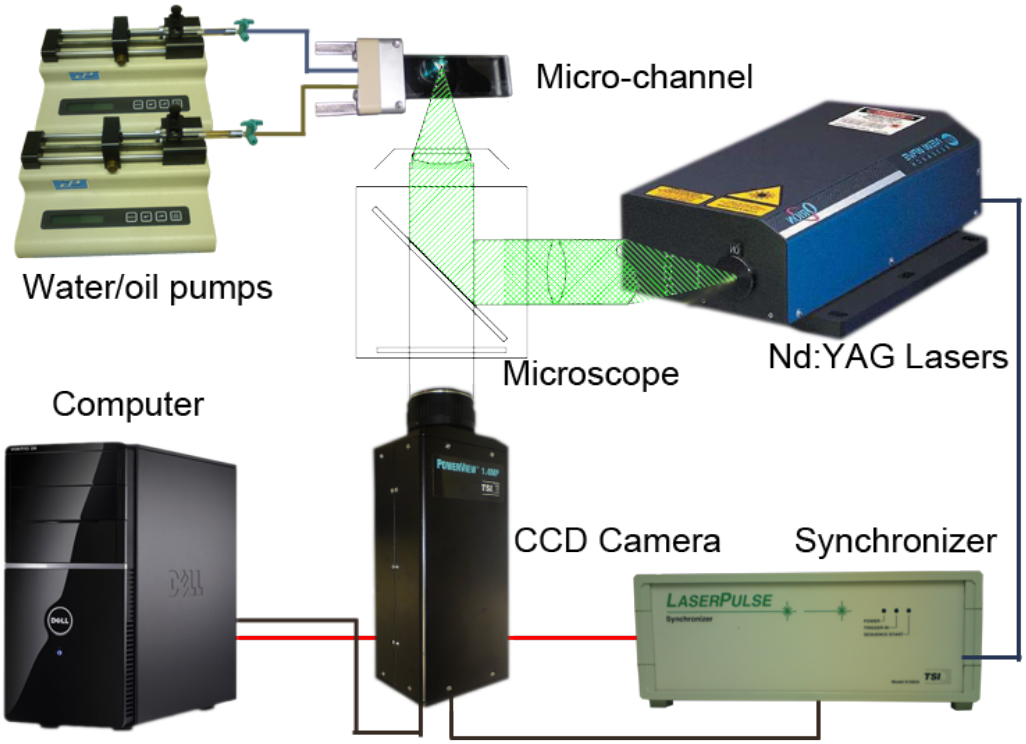

Figure 4: Experimental setup.

2.1.1 Injection system

The injection system consists of a syringe, a syringe pump and a micro-capillary together with accessories used for mounting the circuit. The fluids were injected with two *COLEPALMER 78-0100C* syringe pumps. The pumps have stepper motors where the gears can be controlled by a microprocessor, which provide volumetric injection rates with $\pm$ 0.5 % accuracy and $\pm$ 0.2 % reproducibility of measurements [2]. The minimum flow injection supplied by the pumps is 0.01 ml/hr.

Two glass syringes (figure 5a) containing 10 ml each were used and connected to the micro-capillary via a three-way *embramed* plastic tap and plastic/rubber tubes (figure 5b). The syringes have a metal plunger tip coated with teflon which ensures dimensional stability and does not allow leakage of liquid or gas even at high pressures (up to 200 psi). A "luer lock" connection allowed a tight connection between the three-way *EMBRAMED* plastic tap and syringes/pipes. The connections and tubes between the syringes and micro-capillary were designed to contain the smallest number of elements and volume to accelerate the work done by the pumps, and to be as strict as possible in order to minimize the risk of leaks and transition effects due to deformation of the tubes.

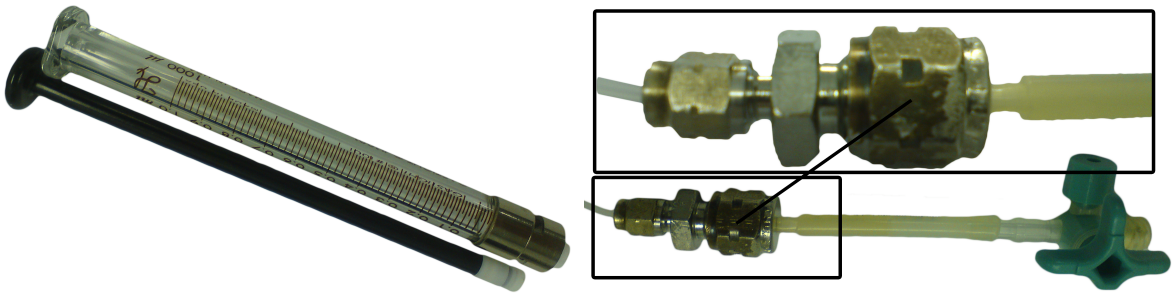

(a) Hamilton Gastight 1000 syringe. (b) *Embramed* plastic tap with tubes and connections.

Figure 5

The capillary used for this experiment is a micro-fluidic T-junction (The Dolomite Centre Ltd, UK). It is made of glass and designed for a wide range of applications, including fluid mixing, micro-droplet formation and reactions. The capillary has a high visibility, excellent chemical compatibility, the surface is extremely smooth and it can function in a wide temperature and pressure range. According to the information sheet from the manufacturer[8], the device has been made by Hydrofluoric Acid (HF) etching and thermal bonding. The geometry of the channels presents an oval cross-section with the same size throughout the whole length of the channels. Figure 6 shows the micro-fluidic device and some of its features.

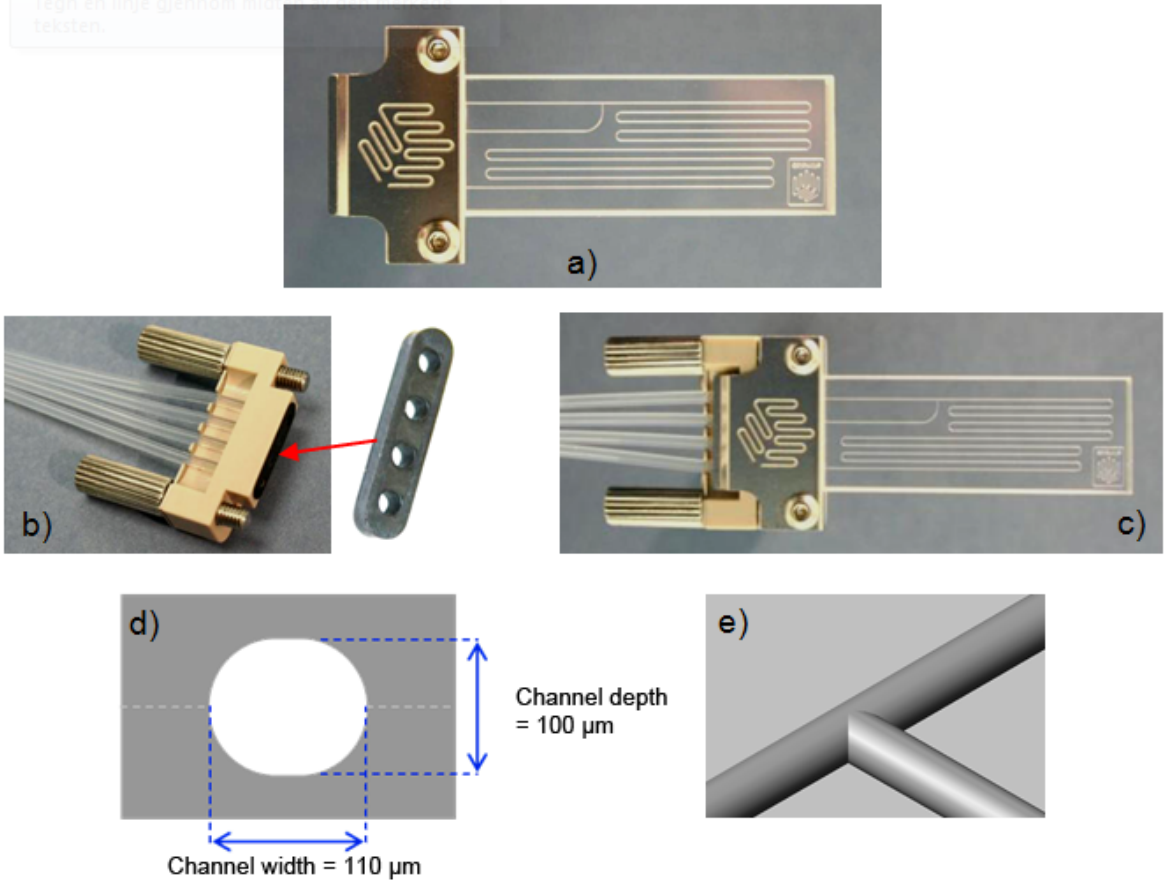

Figure 6: a) Micro fluidic T-junction, b) connector and seal, c) T-junction mounted with tubes, d) channel cross-section profile and e) 3D image of T-junction.

2.1.2 μ-PIV system

The μ-PIV system is manufactured by TSI and consists of a CCD camera, Nd:YAG lasers, microscope, tracer particles and software used for processing acquired images. The microscope (*Olympus Mod.IX71S1F-3*) was used with a *OLYMPUS UPlanFLN 10 × 0.30* (figure 5b) lens and a filter cube (figure 3a). The microscope is shown in figure 7a.

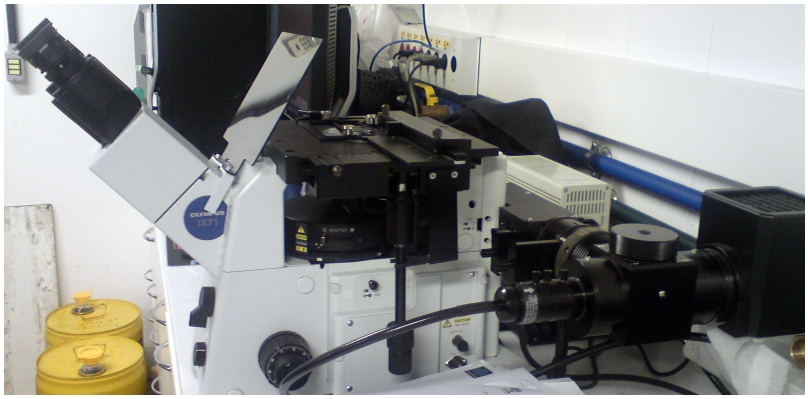

(a) Microscope.

(b) Micro spheres.

Figure 7

The distilled water was seeded with polystyrene micro-spheres (*Thermo Scientific Fluoro-Max Fluorescent Particles*) with diameters equal to 1 μm. These micro-particle tracers emit orange light with peak fluorescence absorption and emission of 542 nm and 612 nm respectively. The Firefli process are used to hard-dye the fluorescent particles throughout the matrix. This method produces bright fluorescent colors, minimizes photobleaching, and prevents dye leaching into aqueous media. The particles are made of polystyrene (PS), which has a density of 1.05 g/cm^3 and a refractive index of 1.59 at 589 nm ($25° C$).[11] The micro-spheres can faithfully follow the flow without disturbing the fields and without changing the speed and fluid properties. Figure 7b shows the micro-spheres.

The flow through the T-junction was illuminated with two Nd:YAG (Neodymium: Yttrium -Aluminium - Gallium) *PIV SOLO - SOLO Mod III* lasers, manufactured by *NEW WAVE* with a wavelength of 532 nm and 50 mJ per energy pulse. The energy sources of the lasers are composed of three distributed systems: the logical electronic control, the high voltage electrical and the cooling system. The Nd:YAG lasers uses a flash lamp to produce the energy that is converted into the laser beam. When operated at maximum frequency (15 Hz), the model allow for a time interval of the order of microseconds between laser shots. The model has a two laser configuration where one laser is fired, and then the other. The beams from the two lasers are combined into a collinear beam. This configuration allows any pulse separation from very short to long with the full power of each laser.

A POWERVIEM CCD 1.4MP Sensicam Mod-630066 camera was used to capture images of the illuminated tracer particles. The camera was connected to the fluorescence microscope in such a way that no unwanted light besides the emitted light from the fluorescence particles entered the camera. The resolution equals 1376 × 1040 pixels with a pixel size 6.45 μm × 6.45 μm and a 12 bits gray intensity.

In a PIV-system, synchronization between the lasers, the CCD camera and the computer is necessary to control image exposure, laser pulse delays and separation. The *LASERPULSE - Mod 610034 synchronizer* takes care of this and was used to control the timing sequence of shots of the laser pulse (trigger) and exposure of the camera. The figure (4.8) shows the synchronizer used in this system.

The whole μ-PIV system was controlled by a computer using the software *INSIGHT 3G*. This software, as well as controlling the image acquisition, was used to adjust and calibrate the system (timings, exposure, etc.) and process the images to calculate the velocity fields of the flow.

2.2 Fluids

Distilled water with and without fluorescent particles and OP3 mineral oil were used in this experiment. The OP3 mineral oil was chosen because it has low viscosity at room temperature, it is insoluble in water and also because it is well known as a standard for calibrating instruments. In addition, the oil is colorless, odorless and soluble in most organic solvents. At room temperature ($23^\circ C$), the viscosity of the oil and water equals 3.40 and 0.94 $mPa{\cdot}s$ respectively, while the surface tension equals 22.0 and 72.3 mN/m.[3]

2.3 Seeding concentration

Before the experiment could be performed, a proper fluorescent particle concentration needed to be established. The tracer particle selection criteria are: particles must be small enough to follow the flow, particles must scatter enough light to be detected and particle concentration must be high enough to give reliable velocity measurements. Since some of the criteria conflict, some compromise had to be made. If the fluid is seeded with too many particles, the background illumination consisting of the reflection of particles out of focus will be too intense and blur the emitted light from the in focus particles. For the opposite case, too few particles will lower the vector field resolution and a larger amount of images are needed to generate good vectors. Many different concentrations were tested and used before a 0.1 % concentration of seeded fluorescence particles in distilled water was found to be the optimal concentration. Since the number of seeding particles depends on the velocity of the flow and magnification, these values were determined early and used from the start of the concentration testing to the very end of the experiment.

2.4 Laser power measurements

Since the Nd:YAG lasers used for this experiment are very powerful and the fiber optics used to guide the laser beam from the laser to the microscope can be destroyed by to high light intensity, some power measurements had to be done. Both lasers were turned on and both the flash lamp and frequency were set to maximum. The CCD camera and synchronizer were then switched on before the *Insight 3G* software was started. In the capture settings, the Q-switch delay was changed for each laser during the measurements. A power/energy meter was used to measure the work done by the lasers. The camera limited the maximum frequency to 4.83 *Hz*. Using the equation below, the energy was calculated and plotted against the Q-switch delay time (figure 8).

$$\frac{E}{puls} \cdot f = W$$

E is the laser light energy, f the frequency and W the measured work. To limit the maximum laser light energy and securing the fiber optics, the following values for the q-switch delay were used (in the laser power settings in *Insight 3G*):

Table 1: Capture settings and measured energy.

	High (μs)	Medium (μs)	Low (μs)
Laser A	280	300	420
Energy (mJ)	35.2	24.8	0.6
Laser B	330	350	460
Energy (mJ)	35.2	24.8	0.8

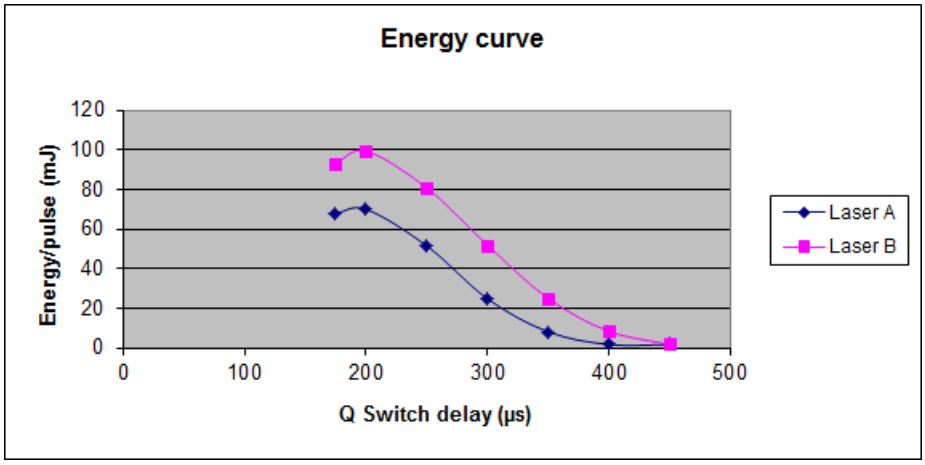

Figure 8: Laser pulse energy plotted against Q-switch delay time.

2.5 Method

After the seeding concentration and laser Q-switch delay settings were decided, the experiment could be initiated. Both lasers were switched on (flashlamp was set to minimum for the lasers to start) and when ready, the frequency and flash lamp were set to maximum and the laser trigger to external. The CCD camera and synchronizer were turned on before the *Insight 3G* software was initiated. While waiting for the lasers to warm up, the pump system and fluids were prepared. Distilled water seeded with 0.1 % fluorescent microspheres was placed in one of the syringes and connected to the main entrance in the micro-capillary. Mineral OP3 oil was put in the other syringe and connected to the second entrance of the micro-capillary. Before the connection was done, all remaining air bubbles inside the syringes were squeezed out.[1]

Each of the syringes was then mounted on a pump while the micro-channel was mounted on the microscope. White light illumination was used to adjust the position of the micro-channel and the focus. With the T-junction in center of the image and in focus, the pumps were started with flow rates equaling 0.15 and 0.10 ml/h for the continuous (Q_c) and discontinuous phase (Q_d), respectively. The flow rates were maintained for some minutes until the oil droplet formation in the T-junction was initiated and stable. From experience, the flow rates need to be as low as possible to get good images and vector fields due to the low camera frequency (4.83 Hz). There is also a lower limit for the flow where the drop formation in the T-junction becomes unstable. $Q_c = 0.03$ and $Q_d = 0.01$ ml/h were found to be the best suited flow rates for this experiment. Inertia is present in the system due to the length of the tubes so the system needed 5-10 minutes before the flow was stable and with the proper speed.

Back to the *Insight 3G* software in the capture timing setup, the PIV frame mode was set to *straddle*, pulse repetition rate to *4.83 Hz*, laser pulse delay to *200 µs* , laser pulse separation (Delta T) to *1200 µs* and PIV exposure to *1000 µs*. In the Laser A and Laser B boxes on the Capture tab control panel, the laser power level was set to *high* for both lasers. Before the lasers were fired and capturing initiated, exposure mode was set to *synchronized* and capture mode to *continuous*. The focus was then adjusted to sharpen the emitted light from the fluorescent micro spheres and to adjust the micro-channel position. With the focus and position optimized, the continuous capture mode and lasers were stopped. Thereafter, capture mode was changed to *single* before again firing the lasers and start capturing . A 32×32 pixel grid was applied and the displacement of the particles between the two laser pulses was measured. The rule of thumb suggests a displacement equal one quarter of the desired interrogation area, in this case, 8 pixels. A pulse separation time equal *1200 µs* gave a pixel displacement around 6-8 pixels, which was considered optimal for the flow.

[1] From now on the dist. water with the microspheres and the oil will be referred to as the continuous phase and discontinous phase, respectively.

The capture mode was changed to *sequence* with 200 images to capture. Again, lasers were fired and images were captured and saved. In order to process the images, sorting was necessary since the droplet in each image was on a different stage in the formation. Ensemble correlation processing will only work and generate good vector fields with images containing image pairs contributing in the same manner in each interrogation area. The sorting was done manually by comparing images. First, each one of the images was imported in the computer software *Adobe Lightroom 3.2* where exposure, contrast, sharpening, brightness and detail were adjusted. The before and after image are compared in figure (9a). 9 different stages were then defined and all images were sorted into one of the 9 stages by comparing them to a master image with scale (figure 9b).

With the images sorted, each stage (consisting of unique images) was selected and processed in *Insight 3G*. A pre-processing including background subtraction using minimum/average intensity was initiated, but too much intensity was lost or too much noise was introduced in the process for it to enhance the images. Further, a processing mask was defined for each of the stages excluding everything in the images except the fluorescent particles. Also, the length scale was calibrated by measuring the width of the micro-channel, giving the ratio $\mu m/pixel = 0.41$.

Different processing parameters in the *PIV processor setup* were tried and optimized for each stage before choosing the following parameters: PIV Algorithm: Ensemble PIV, Grid Engine: Recursive Nyquist Grid, Spot Mask Engine: None, Correlation Engine: FFT Correlator, Peak Engine: GaussianPeak, Starting Spot Dimensions: 64×64, Final Spot Dimensions: 32×32 and Maximum Displacement: 0.25. Depending on the droplet stage to be processed, in the Plugin Settings, the X-offsett pass 1 ranged from 3-6, while the PeakToNoisePeak was set to 1.4. In the Pass Validation Settings, both vector and local validation were chosen. At last, in the PIV Advanced Settings dialog, Rohaly-Hart Analysis with 3 passes and export of one secondary peak were enabled. The number of good vectors created after the processing ranged from 95-98 % of the total vectors, while the number of images processed varied between 9 and 36, depending on the evaluated stage.

Before the final vector field was created and exported to the software *Tecplot* for velocity computation, the vector field was post-processed with local and vector validation to remove bad vectors, fill empty holes and to smooth the vectors.

(a) Image before and after *Adobe Lightroom 3.2* adjustments. (b) Master image.

Figure 9

3 Results and discussion

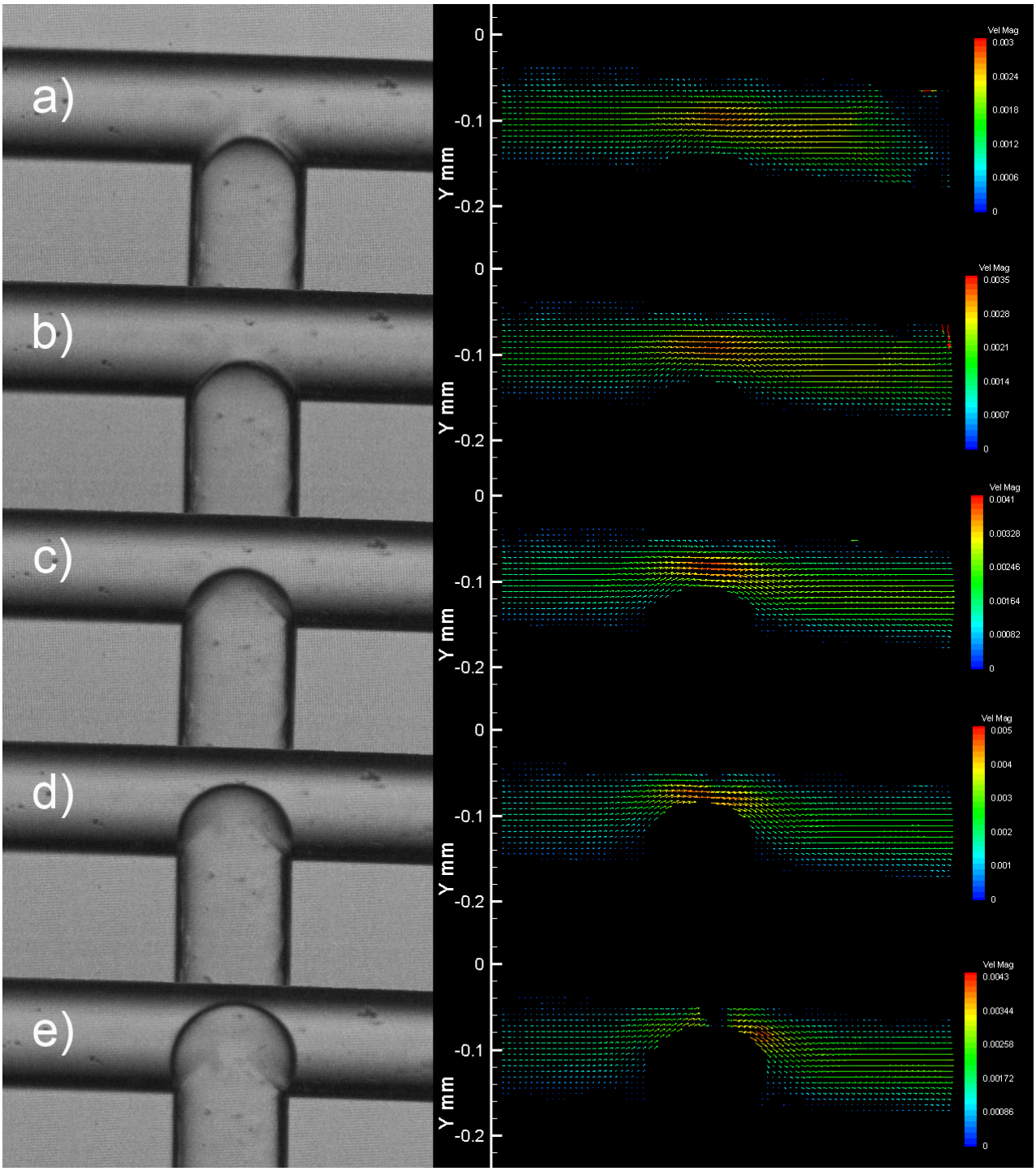

Figure 10: Velocity field for the formation of an oil droplet in water for the 5 first growth stages, a) - e).

Figure 10 and 11 show 9 different velocity fields illustrating the oil drop growth process during one period in the micro-fluidic T-junction. To the left in the figures, the drop formation is captured as seen through the microscope with normal light. The black color on the generated vector fields (right part

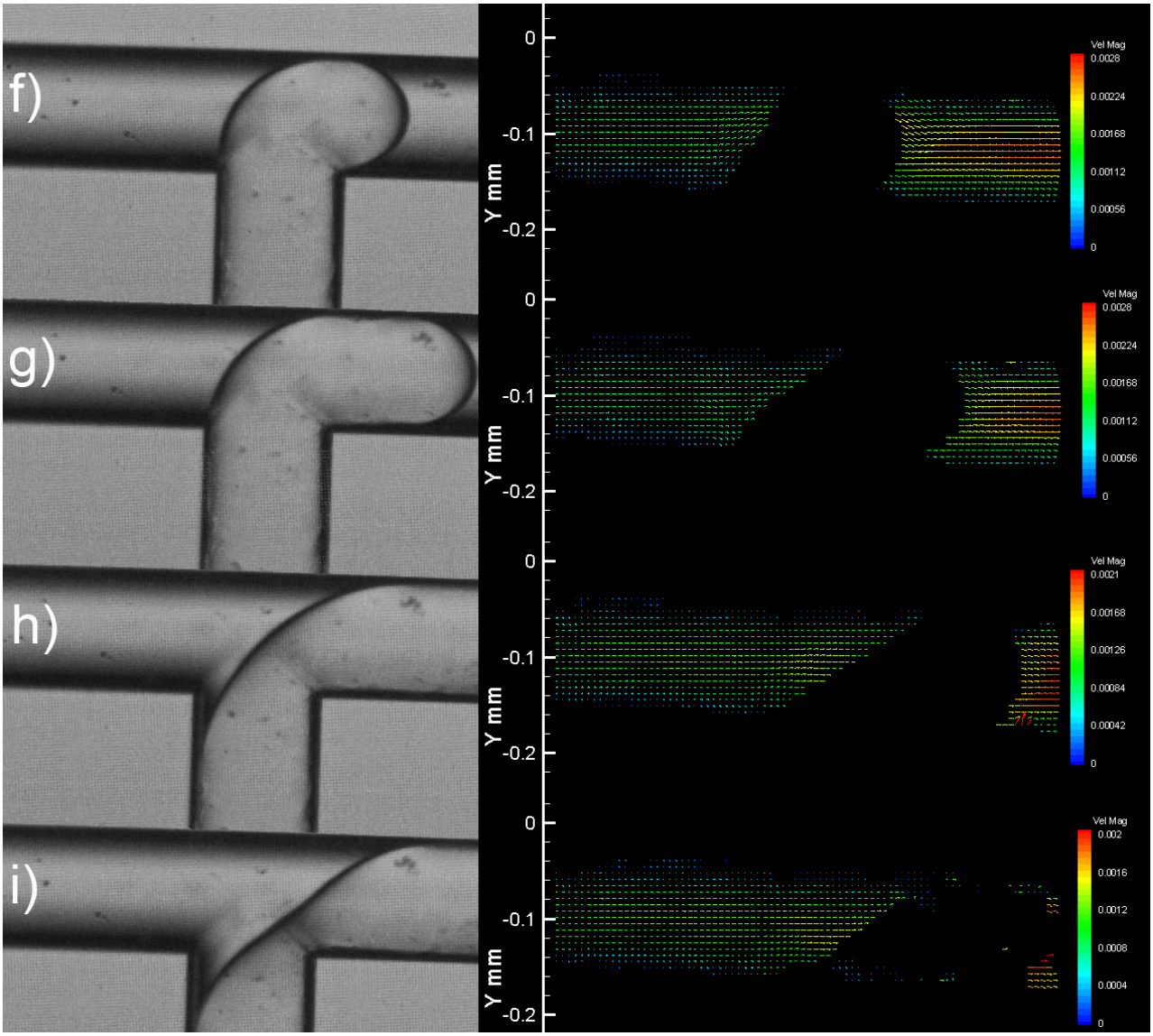

Figure 11: Velocity field for the formation of an oil droplet in water for the 4 last growth stages, f) - i).

figures) indicates no fluorescent particles present, while the colored arrows show the tracer particles velocity and thereby flow through the channel. The oil drop in the generated velocity field images is black since no fluorescent micro-spheres particles were added to the oil.

In order to check the validity of the obtained velocity values, a comparison with the expected average flow velocity values has to be made. The calculation is easily performed by using;

$$1\,ml = 1 \times 10^{-3}\,l = 1 \times 10^{-3}\,l \cdot 10^{-3}\,m^3/l = 1 \times 10^{-6}\,m^3$$
$$1\,h = 1\,h \cdot 60\,min/h \cdot 60\,s/min = 3.6 \times 10^3\,s$$
$$100\,\mu m = 1 \times 10^2\,\mu m \cdot 10^{-6}\,m/\mu m = 1 \times 10^{-4}\,m$$

The calculation of the expected average flow velocity is then:

$$v_c = \frac{Q_c}{A} \approx \frac{0.03\,ml}{(100\,\mu m)^2\,h} = \frac{3 \times 10^{-8}\,m^3}{3.6 \times 10^{-5}\,m^2 s} = \frac{1\,m}{1200\,s} \approx 0.00083\,m/s$$

$$v_d = \frac{Q_d}{A} \approx \frac{0.01\,ml}{(100\,\mu m)^2\,h} = \frac{1 \times 10^{-8}\,m^3}{3.6 \times 10^{-5}\,m^2 s} = \frac{1\,m}{3600\,s} \approx 0.00028\,m/s$$

where A is the cross section area, Q_c and Q_d is the flow rate of the continuous and discontinuous fluids, respectively.[2] The flow in the channels exhibit a parabolic velocity profile with maximum velocity magnitude in the middle of the channel. In figure 10 a), the velocity magnitude varies between 0 *m/s* at the wall to around 0.0016 *m/s* at the middle of the channel (before the T-junction). The calculated average velocity equal 0.00083 *m/s* and verify the obtained velocity magnitude range. To calculate the actual average flow velocity crossing the elliptical cross section of the channels, the velocity of all individual vectors at each cross section have to be integrated from wall to wall. Unfortunately, this was not done due to insufficient time and knowledge about the software.

As time passes, the oil droplet grows in the T-junction and less area is left for the water to flow through the channel above the droplet. This leads to an increase in the flow velocity above the droplet since the average flow rate is constant through the channel per cross section. The velocity magnitude bars in figure 10 a) - e) confirm this. After the oil droplet fills the entire T-junction, water pulls the droplet interface through the channel until pinch-off (11 f) - i)). The velocity profile for the flow is still parabolic through the channel and the maximum velocity magnitude around 0.0016 *m/s*. The figures above also compare the droplets seen with normal light (without the cube) with the black colored droplets seen in the generated velocity field images. The conformity is excellent for all the stages.

By the experiments presented in the report, the methods, parameters and obtained experience is at least as important as the attained result. After becoming familiar with the micro-PIV instrument, procedures, techniques and software, some experience and key factors to optimize an micro-PIV experiment will be presented and shared for helping future experiments. Before starting the experiment, the velocity range of the flow and the desired magnification are the first two things that should be decided. The lens magnification will alter the field of depth and the velocity will change the number of seeded particles passing by the cross section in a certain time. With these parameters in place, the right type of tracer particles and concentration has to be found. There is no answer book here, one just has to try with different concentrations in order to find which concentration is the best and gives sufficient particles without having too much background light scattering from unfocused particles. In this experiment the number of particles per interrogation window of size 32×32 was around 3-4, but it was less at spots where the flow velocity was faster. The next parameter to optimize is the laser pulse separation (dT) value. This parameter is a key parameter for matching the micro-PIV system to the flow velocity. The rule of thumb is that maximum in-plane displacements should be less than 1/4 of the interrogation spot size and the minimum in-plane displacement should be at least two particle-image diameters.

With quality images captured and saved on the computer, the most important and difficult job is done. Depending on the experiment and desired resolution, the processing parameters and the number of images needed for good velocity fields vary. More images and advanced processing techniques give a higher percentage of good vectors, but also increase the processing time. Before post-processing, the portion of good vectors should be over 95 %.

The result presented in this report can be improved in many ways. A triggering system would increase the likeness of the captured droplets at their different stages compared to a manual selection and remove the work and time spend on the selection process. The correlation will then become more accurate and thereby improve vector resolution and amount of good vectors. A trigger system would also measure the time between the different droplet growth stages. Also the number of captured images for each droplet stage should be increased to improve the results and it is recommended to increase the microscope magnification as well so that a larger portion of the pixels on the camera are being used.

[2] To ease the calculations, the cross section area is chosen to be squared.

Other improvements include a more powerful and faster laser together with a highspeed camera. Future experiments should study the velocity field for different fluids and flow rates for both the continuous and discontinuous fluid. It would be interesting to calculate the average flow rates through different cross sections (with integration) for different droplet grow stages, measure the velocity of the droplet in the T-junction, measure the time between the different stages and also validate the parabolic velocity profile.

4 Conclusion

In this experiment micro-PIV is used to study the velocity field around a growing oil droplet in a T-junction with water as the continuous fluid. Velocities in a 100 μm elliptical T-junction were measured with a spatial resolution of 13 $\times$ 13 μm^2. The flow velocities exhibit parabolic profiles and the velocity magnitudes increase as the droplet grows in the T-junction. Calculated values of the expected average flow velocity validate the obtained velocity magnitudes and the calibration. The experiment and report both focus on methods, parameters and setup used to optimize the velocity fields and generating them without using any triggering mechanism. An untraditional manual image selection technique and advanced processing parameters were used to analyze and measure velocity fields for 9 different droplet grow stages.

The results indicate that manual selection of images gives satisfactory velocity fields, but a triggering system can easily improve the resolution and remove the time consuming work spent on the selection process. Other improvements include a more powerful and faster laser together with a camera with higher frequency. It is also recommended to use a higher number of captured images for each droplet stage and increase the microscope magnification. Interesting experiments for the future include changing the fluids, flow rates and perform droplet velocity and time measurements together with validation of the parabolic velocity profile and average flow rates.

References

[1] M. Raffel, C. Willert, S. Wereley and J. Kompenhans, PIV - A Practical Guide, Second Edition, Springer (2007)

[2] Accessed November 2011: `http://www.coleparmer.com/catalog/product_view.asp?sku=7490300`

[3] D. E. G. Campos, Formao de emulses em uma juno de micro canais em T, PUC (2011)

[4] O. . F. R. Castillo, Anlise Experimental do Escoamento de Emulses leo em gua atravs de Micro-capilares com Garganta, PUC (2011)

[5] TSI®, Micro Particle Image Velocimetry - Operation Manual, P/N 1990062 Revision C (Aug. 2006)

[6] TSI®, Insight 3G Users Guide, P/N 1980511, Revision G (2008)

[7] TSI®, PIV Theory of Operation, P/N 1990755A, Revision A (1999)

[8] The Dolomite Centre Ltd, Information Sheet Mitos Thin Layer T-Junction Chip with Header

[9] The Dolomite Centre Ltd, Information Sheet Micro Spheres

[10] V. v. Steijn, M. T. Kreutzer and C. R. Kleijn, μ-PIV study of the formation of segmented flow in microfluidic T-junctions, Chemical Engineering Science 62 (2007)

[11] Thermo Scientific Particle Technology, Product Catalog and Technical Reference Guide: Fluoro-Max Fluorescent Particles Dyed Red Aqueous (for contamination control and flow tracing) (2011)

Appendix F

Manuscript: Characterization of Paraffin/Clay Nanocomposites

This chapter presents a manuscript for an article which soon will be submitted to a scientific journal (Material Science and Engineering A. or Langmuir).

Characterization of Paraffin/Clay Nanocomposites

Zbigniew Rozynek[1], René C. Castberg[2], Alexander Mikkelsen[1] and Jon Otto Fossum[1,3]

[1] Department of Physics, NTNU, Høgskoleringen 5, NO-7491 Trondheim, Norway
[2] Physics Department, University of Oslo, Postboks 1048, NO-0316, Oslo, Norway
[3] Center for Advanced Study – CAS at Norwegian Academy of Science and Letters, Drammensveien 78, NO-0373 Oslo, Norway

Abstract

We are concerned here with the behavior of fluorohectorite synthetic clay particles dispersed in paraffin-wax. First, the characterization of the pure paraffin-wax by means of rheometry and X-ray diffraction is reported. Next, the time evolution of the one-to-zero/zero-to-one water layer transition in fluorohectorite clay galleries is presented. We then report Wide angle X-ray scattering (WAXS) as related to electric field (*E*) induced alignment of clay particles as a function of electric field. Finally, we provide observations of system anisotropy during melting and crystallization of clay/paraffin nanocomposites.

Keywords: Clay, alignment, electric field, paraffin, composite

1. Introduction

Clay particles often change and improve many physical properties, e.g. mechanical strength, thermal stability, conductivity, etc. of the medium in which they are suspended.[1,2,3] Some of these properties can be directionally enhanced if the particles are deliberately orientationally aligned in the host medium. For example, such particle organization can be utilized as a molecular barrier, i.e. the permeability of gas molecule in polymer/clay composite is significantly reduced in direction normal to clay's platelet surfaces, whereas no change is expected for molecules propagating along the clay surfaces. Yano et al.,[4] found that only 2 wt.% addition of montmorillonite clay particles into polyimide may bring gas permeability down to a value less than half of that of polyimide alone. Alignment of clay particles can be induced by planar shearing,[5] extrusion,[6] gravity,[7] magnetic[8] or electric fields.[9]

[1] H. J. Walls, M. W. Riley, R. R. Singhal, R. J. Spontak, P. S. Fedkiw and S. A. Khan, *Adv. Funct. Mater.* **13**, 710-717 (2003).
[2] S. H. Kim, J. Eun-Ju, Y. Jung, M. Han and S. J. Park, *Colloid. Surface.* **313**, 216-219 (2008).
[3] D. Ratna, S. Divekar, A. B. Samui, B. C. Chakraborty and A. K. Banthia, *Polymer* **47**, 4068-4074 (2006).
[4] K. Yano, A. Usuki, A. Okada, T. Kurauchi and O. Kamigaito, *J. Polym. Sci. A* **31**, 2493–2498 (1993).
[5] M. Okamoto, P. H. Nam, P. Maiti, T. Kotaka, T. Nakayama, M. Takada, M. Ohshima, A. Usuki, N. Hasegawa and H. Okamoto, *Nano Lett*. **1**, (2001).
[6] X. He, J. Yang, L. Zhu, B. Wang, G. Sun, P. Lv, I. Y. Phang and T. Liu, *Appl. Polym. Sci*. **102**, 542–549 (2006).
[7] H. Hemmen, N. I. Ringdal, E. N. De Azevedo, M. Engelsberg, E. L. Hansen, Y. Méheust, J. O. Fossum and K. D. Knudsen, *Langmuir* **25**, 12507–12515 (2009).

An electric field is often used to produce anisotropic structures in order to obtain desirable physical properties. When coupled with the field or field gradient of either alternating-current (AC) or direct-current (DC), induced dipoles will result in a rotational or translation force on the particles in accord with the Clausius–Mossotti relation.[10] The alignment of particles can be monitored by means of electron or neutron diffraction[11,12], and the degree of anisotropy can be quantified and expressed in terms of an order parameter (S_2) (see Section 3.3). In previously studied clay/silicone oil suspensions, Rozynek et al.[11] showed that the values of the S_2 order parameter did not depend on the *E*-field strength (within measured range of *E*-field strengths, namely 350-750 V/mm). Since the silicone viscosity was low (100 mPa·s) and the electric field high, the clay alignment was very rapid and its development was thus difficult to monitor.

In the present work, the average orientational clay distribution is measured in a melted paraffin-wax. There are few major differences between these two types of systems. The viscosity of paraffin-wax is significantly higher, its molecules are longer and the clay alignment is achieved at higher temperatures, i.e. between 65 and 100 ºC.

The layout of this article is as follows. First, the sample preparation is explained in section 2 together with characterization of the pure paraffin-wax. The wide angle X-ray scattering results are presented in section 3 and these include: time dependent one-to-zero water layer transition (section 3.1); zero-to-one water layer transition (section 3.2); alignment of clay particles as a function of both the *E*-field strength and polar angle (section 3.3); and finally, the development of the system anisotropy during melting and crystallization (section 3.4). Conclusions and suggestions for further work are presented in the final section, 4.

[8] E. N. de Azevedo, M. Engelsberg, J. O. Fossum and R. E. de Souza, *Langmuir* **23**, 5100 (2007).
[9] J. O. Fossum, Y. Méheust, K. P. S. Parmar, K. D. Knudsen, K. J. Måløy and D. M. Fonseca*, Europhys.Lett.* **74**, 438-444 (2006)
[10] Y. P. Huang, M. J. Lee, M. K. Yang and C. W. Chen, *Appl. Clay Sci.* **49**, 163-169 (2010).
[11] Z. Rozynek, K. D. Knudsen, J. O. Fossum, Y. Méheust, B. Wang and M. Zhou*, J. Phys.: Condens. Mat.* **22**, 324104 (2010).
[12] K. D. Knudsen, J. O. Fossum, G. Helgesen and M. W. Haakestad, *Physica B: Condens. Mat.* **352**, 247 (2004).

2. Sample preparation and characterization

In this work we have chosen to work with the synthetic clay fluorohectorite. There are several reasons for this choice. Firstly, in terms of structure, fluorohectorite is virtually identical to natural smectite clays such as montmorrillonite.[13] Secondly, our group has studied fluorohectorite as a model system for clays[14,15] for many years now, and we know and understand many details of this system.

Lithium fluorohectorite (Li-Fh) was purchased from Corning Inc., New York in the form of a white powder. Li-Fh is a synthetic 2:1 smectite clay having the nominal chemical formula $Li_{0.6}[Mg_{2.4}Li_{0.6}]S_4O_{10}F_2$ per half unit cell, where Li^+ is an interlayer exchangeable cation. Li-Fh has a surface charge of 1.2 e^-/unit cell and is a polydisperse clay with platelet diameters ranging from a few hundred nm up to a few μm.[15] A *single* particle consists of about 80–100 platelets (crystalline sheets)[16,17] that stack on top of one another forming a "deck of cards" structure. Since the thickness of such a stack is approximately 0.1 μm, the resulting particle has a diameter-to-height ratio close to 20:1 on average. However, the *single* particle tends to agglomerate when dispersed into a non-polar medium (e.g. oils, polymeric matrices), unless chemically treated.[18] Both the shape and size of aggregated structures may vary, and in general they depend on clay type and sample preparation.[19,20] The Li-Fh clay absorbs water, which makes it swell. The swelling of layered 2:1 smectite clay particles is caused by a change in the interlayer repetition distance between crystalline sheets (*d*-spacing). This behaviour depends on temperature and humidity, and can be monitored by means of X-ray diffraction.[21]

The paraffin-wax normally refers to a mixture of *n*-alkanes (chemical formula C_nH_{2n+2}) with *n* ranging between 20 and 40 determining the characteristic length of the molecules and also the melting temperature of the paraffin matrix. The material used for composite preparation was ordered from Sigma-Aldrich (ASTM D 127, batch: MKBC6750). This particular type of paraffin wax has its melting point around 65 ºC and was chosen due to the

[13] P. D. Kaviratna, T. J. Pinnavaia and P. A. Schroeder, *J. Phys. Chem. Solids* **57**, 1897 (1996).
[14] J. O. Fossum, *Physica A* **270**, 270 (1999).
[15] J. O. Fossum, *Eur. Phys. J. Special Topics* **204**, 41-56, (2012).
[16] H. Hemmen, L. R. Alme, J. O. Fossum and Y. Meheust, *Phys.Rev. E* **82**, 036315 (2010).
[17] H. Hemmen, L. R. Alme, J. O. Fossum and Y. Meheust, *Phys.Rev. E* **83**, 019901(E) (2011).
[18] B. Wang, M. Zhou, Z. Rozynek and J. O. Fossum, *J. Mater. Chem.* **19**, 1816 (2009).
[19] Z. Rozynek, T. Zacher, M. Janek, M. Čaplovičová and J. O. Fossum, *Electric-field-induced structuring and rheological properties of kaolinite and halloysite clays,* **submitted** to Appl.Clay Sci. (21.04.2012).
[20] Z. Rozynek, B. Wang, J. O. Fossum and K. D. Knudsen, *Eur. Phys. J. E* **35**, 9, (2012).
[21] G. J. Silva, J. O. Fossum, E. DiMasi and K. J. Måløy, *Phys. Rev. B* **67**, 094114 (2003).

following reasons: (i) the X-ray peak positions related to the characteristic molecule dimensions should not overlap with clay reflections related to the interlamellar distance, i.e. space between clay crystalline sheets; (ii) optimal melting and crystallization temperatures providing both the ease of composite preparation and appropriate stiffness of the composite when in solid form at room temperature; (iii) relatively non-polar and non-conductive material that can be used as an electrorheological carrier fluid when in the melted state.

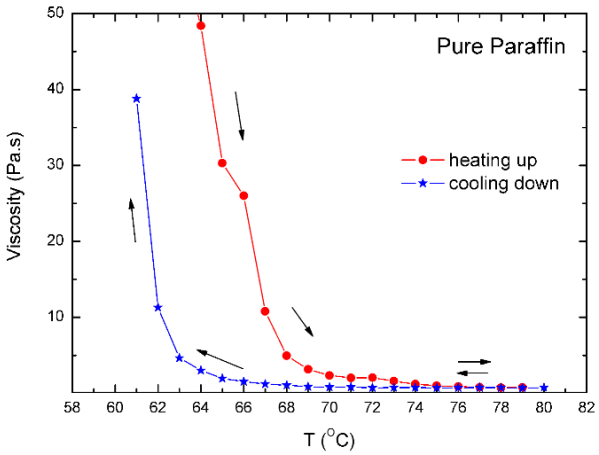

Figure 1. Rheological data showing both the melting and the crystallization transition temperatures for pure paraffin wax used in the present studies, see text.

Prior to the composite preparation, a melting point of the pure paraffin-wax was measured by employing the Physica MCR 300 Rotational Rheometer equipped with a coaxial cylindrical cell C27/ERD. The crystalline melting temperature appeared around 65 ºC, as shown in Figure 1. The temperature range where crystallization occurs, and consequently, also the range of melting during the subsequent heating, are broad. The observed hysteresis width is additionally broadened by the fast heating rate of 1 ºC/min.

Complementary information about pure paraffin is provided by wide angle X-ray diffraction measurements, where diffractograms were collected for the sample during the solid-to-liquid transition, is displayed in Figure 2 and discussed the following: In the solid form, the paraffin-wax has a crystal structure that is composed of stacked layers of the disentangled molecules, each layer being assembled of chain molecules with identical helical conformations.[22] However, when heated up, they take on coiled conformations just like polymers, and the regular structure is lost. Figure 2 shows the X-ray diffractograms of pure paraffin-wax during heating from 25 to 85 °C. The characteristic peaks attributed to the lengths of the oligomer molecules start shifting and decreasing at a temperature range between 60 and 75 °C. They vanish completely for higher temperatures, indicating a loss of

[22] G. Strobl, *The Physics of Polymers*, 2nd ed., Springer, p.143-144 (1997)

crystallinity. These results coincide with our optical microscopy observations (see supporting Figure S1) and our rheological data shown in Figure 1. For more details about paraffin-waxes, their different structural phases, solid-liquid phase transitions, positional and orientational order, viscoelastic behaviour, etc., the reader is referred to the literature.[23,24,25,26]

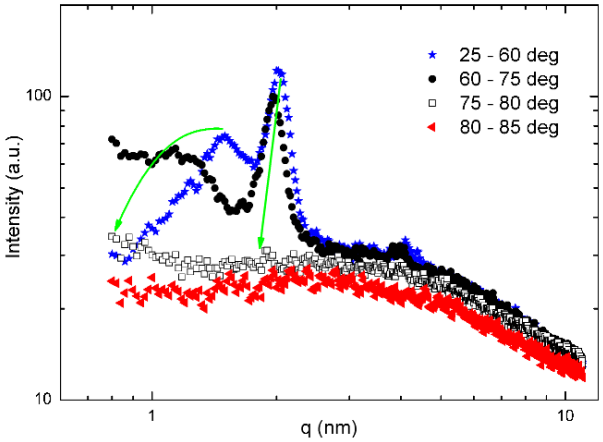

Figure 2. X-ray diffractograms of pure paraffin-wax during heating from 25 to 85 °C. The characteristic peaks attributed to the lengths of the oligomer molecules start shifting and decreasing at temperature range between 60 and 75 °C. They vanish completely for higher temperatures, indicating a loss of crystallinity.

The first set of paraffin/clay composites was prepared as following: 1.4 g of Li-Fh clay powder with one intercalated water layer (1WL) was slowly added into 7 g of pre-melted paraffin wax. After 10 min of stirring, the solution was set at rest for 3 min. to allow the biggest aggregates (in fact, the majority of clay particles) to sediment. The top part (~80 % of the solution), consisting of the smallest clay particles, was then poured into a new 10 ml glass phial. The solution was stabilized at a temperature around 120-130 °C while stirring. Every hour, around 0.5 ml of solution was taken out to make a solid cast. The X-ray diffractograms were collected immediately after each composite had solidified to investigate the time-dependent changes in clay's water content. The same samples (stored in a solid form at room temperature and ~55 % RH) were re-examined by X-ray scattering 6 months later in order to monitor changes in the water content (Set1-Temp).

The second set of samples was prepared similarly to the first one. However, the first sample was collected after 12 h of stirring at temperature between 120 and 130 °C. Around 0.5 ml of a solution was used to make six samples. Electric field (AC, square wave, 100 Hz) with the following magnitudes: 30, 60, 120, 240 and 480 V/mm were applied to five samples during their crystallization while inside a custom-made mould equipped with electrodes

[23] E. Sirota, H. King, D. Singer and H. Shao, *J. Chem.Phys.* **98** 5809 (1993).
[24] G. Ungar, *J. Phys. Chem*. **87** 689 (1983).
[25] M. J. Nowak and S. J. Severtson, *J. Mater. Sci.* **36** 4159 – 4166 (2001).
[26] A. E. Smith, *J. Chem. Phys.* **21**, 2229-2231 (1953).

separated by 6.5 mm. The X-ray diffractograms were collected after each composite had solidified in order to find the clay particle's orientational distribution of particles in an *E*-field (Set2).

The last batch was prepared in order to monitor the dynamic alignment of clay during the composite melting and crystallization inside a custom-made heating cell. Besides temperature, the batch was prepared similarly to the procedure used for the first set. The solution was kept at temperature around 80-90 °C while stirring for 2h. The solution was then cooled down, cut into small pieces that could fit inside the sample holder, sealed inside the glass phial and eventually stored until the experiment. The X-ray diffractograms were collected during heating and cooling to investigate changes in the clay particle's orientational distribution while in an applied *E*-field (Set3-Dyn).

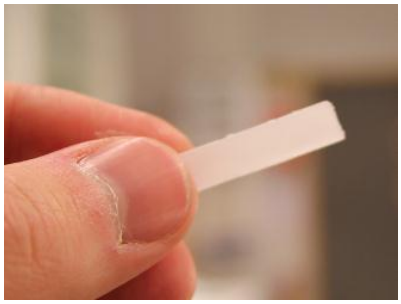

Figure 3. Paraffin/clay composite with a 30 x 6.5 x 1.5 mm^3 dimensions.

The dimensions of composites (Set1-Temp and Set2) are 30 x 6.5 x 1.5 mm^3 and the example of a solid cast is shown in Figure 3. In all samples the clay concentration was estimated roughly to be around 5 wt.%.

3. Results

Two sample sets (Set1-Temp and Set2) were measured at our home laboratory (NTNU, Trondheim, Norway) using NanoSTAR from Bruker AXS setup in a wide-angle X-ray scattering (WAXS) configuration during the present experiments. The instrument is equipped with a CuKα Xenics micro-source emitting X-rays at wavelength of 1.5418 Å and a 2-D detector that collects Bragg diffraction rings allowing investigations of the orientational distribution of the clay platelet stacks embedded in the paraffin-wax matrix. The beam size at the sample is about 0.4 mm in diameter. The sample-to-detector distance was calibrated using a silver behenate standard. The available scattering *q*-range for the setup used here was 0.08 – 1 $Å^{-1}$.

Investigations of the dynamic alignment of clay particles (Set3-Dyn) were performed at the European Synchrotron Radiation Facility (ESRF) in Grenoble, France. An X-ray beam with a wavelength of 0.9Å and a 0.3x0.3 mm^2 beam size was used at the sample. The beamline BM01A is equipped with a two-dimensional MAR345 image plate detector with a diameter equal to 345 mm. The available scattering *q*-range was 0.03 – 1.6 Å. The custom-made sample cell from NTNU (see supporting Figure S2) enabled precise control of heating and cooling in temperature range between 20 – 100 °C.

3.1. One-to-zero water layer transition

Water can intercalate in between each platelet causing the clay to swell. For Li-Fh, the intercalation process which is temperature and relative humidity dependent, yields four stable hydration states.[27] The structures, referred to as having 0, 1, 1.5 or 2 intercalated water layers, are quite well ordered along the stacking direction. The unit cell along the stacking direction is given by the distance between the stacked platelets. The distance is close to 1.0, 1.2, 1.35 and 1.5 nm for the case of 0WL, 1WL, 1.5WL and 2WL, respectively.

The first set of samples was measured to investigate the time-dependent changes in water content intercalated between the clay's crystalline sheets. The recorded X-ray data allowed the evolution of one-to-zero water layer transition to be monitored.

Figure 4 shows radially integrated two-dimensional WAXS patterns from six samples prepared at different times, namely 0, 2, 3, 5, 7 and 10 h of stirring at elevated temperature around 120-130 °C. Initially, the clay particles (kept in room temperature and humidity, in form of powder) were in the pure 1WL hydration state (first measurement - blue dotted curve). The corresponding 100 Bragg peak was located at 1.21 nm. After two hours, the intensity of the 1WL-peak decreased and a new, broad and not yet clear peak appeared with a distance corresponding to the 0WL hydration state. Those two peaks are asymmetric with respect to their intensities and widths, and both of them are shifted from their initial $d_{100}{}^{1WL}$=1.21 nm and final $d_{100}{}^{0WL}$ =1.03 nm positions towards lower and higher values ($d_{100}{}^{1WL}$ =1.19 nm and $d_{100}{}^{0WL}$ =1.07 nm), respectively. The intensity of the peak related to 0WL state increases with time and becomes sharper. After 5 h, clay particles in the scattering volume contain a significantly higher proportion of 0WL - over 1WL spacings. The clay particles needed nearly 10 h to reach nearly pure 0WL hydration final state (red curve with triangles). A minor population of clay particles possessing the intercalated water still exists, but is hardly detectable by the instrument.

[27] R. P. Tenorio, M. Engelsberg, J. O. Fossum and G. J. da Silva, *Langmuir* **26**, 9703 (2010)

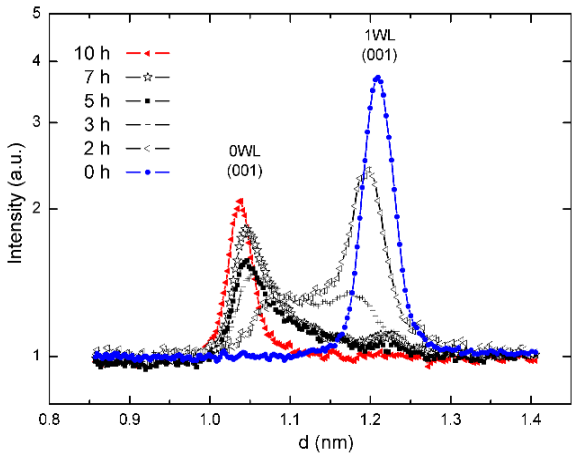

Figure 4. Time evolution of the 1-to-0 water layer transition (S1-Temp).

"Traditionally" the interlayer hydration complexes occurring in smectite clays are considered as pure water layer states, i.e.: 0WL, 1WL, (1.5WL) and 2WL for the case of fluorohectorite clays.[28,] The transitions between those states are "generally" considered to be rather sharp,[29] unlike the present case. However, recently Hemmen et al.[16,17] have thoroughly mapped systematic changes in the d-spacing values (before a discrete transition occurs) as a function of relative humidity (see reprinted Figure 5). Hemmen et al.[16,17] investigated the 1-to-2 WL transition, whereas in the present case the 1-to-0 WL transition was monitored. The maximum values of the smooth changes in the d-spacing, with respect to both the initial and the final state (1WL→0WL), are on the order of approximately 0.3 Å for deviation from 1WL and 0.5 Å for deviation from 0WL. These values are similar to what Hemmen et al.[16,17] reported.

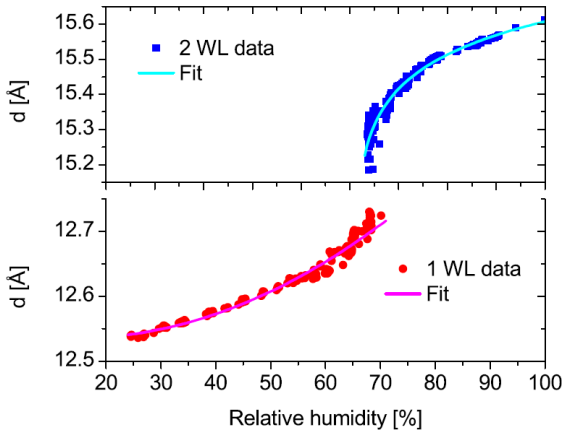

Figure 5. The *d*-spacing as a function or relative humidity (reprinted with permission from Hemmen et al. [16]).

[28] G. J. da Silva, J. O. Fossum, E. DiMasi, K. J. Måløy and S. B. Lutnæs, *Phys.Rev. E* **66,** 011303 (2002).
[29] Y. Méheust, B. Sandnes, G. Løvoll, K. J. Måløy, J. O. Fossum, G. J. da Silva, M. S. P. Mundim, R. Droppa and D. M. Fonseca, *Clay Sci.* **12**, 66 (2006).

3.2. Zero-to-one water layer transition and paraffin intercalation

The same samples (kept in a solid form) were investigated 6 months later in order to monitor the water content. The time 2:1 smectite clays require to hydrate depends on relative humidity, temperature together with size and charge of the exchangeable cation in the interlayer space. For powdered samples the magnitude of the time evolution is on the order of hours.[30,31,32,33] However, as one could expect, the time needed for the entire clay population (inside the paraffin-wax) to absorb 1WL is considerably longer. The effective RH around embedded clay particles is low, since the water penetration through the oligomer matrix is restrained.

Figure 6 shows $I_1/(I_1+I_2)$ ratios between magnitudes of 0WL and 1 WL peak intensities for 6 samples from the Set1-Temp set. Their values are in range 0-1, where 0 indicates a pure dehydrated state, 0.5 is obtained when the number of clay particles in the two states is equal, and 1 depicts the pure mono-hydrated state. Green squared data points were acquired from measuring samples right after their preparation (as shown also in Figure 4). Orange star data points were obtained from the same samples, but measured 6 months later. For all samples (S1-0h omitted in this discussion), water molecules intercalated into clay galleries. However, the complete recovery from a partially dehydrated state (0WL) to a mono-hydrated state (1WL) was only accomplished by the one sample labeled S2-2h. By comparing the intensity ratio values, it can be concluded that the remaining four samples absorbed comparable amounts of water. The two lines in Figure 6 were obtained by fitting the data points to a linear function $y=a+bx$. The calculated values of the slope b were very similar for the two sets, i.e. -0.05±0.02 and -0.06±0.02 for the (dashed) orange and (solid) green curve, respectively.

[30] E. DiMasi, J. O. Fossum and G. J. da Silva, Proceedings of the 12th International Clay Conference, Argentina (2003) *"Synchrotron X-ray Study of Hydration Dynamics in the Synthetic Swelling Clay Na-Fluorohectorite".*

[31] N. Wada, D. R. Hines and S. P. Ahrenkiel, *Phys. Rev. B* **41**, 12895 (1990).

[32] R. W. Mooney, A. G. Keenan and L. A. Wood*, J. Am. Chem. Sot.* **74**, 1371 (1952).

[33] G. Løvoll, B. Sandnes, Y. Méheust, K. J. Måløy, J. O. Fossum, G. J. da Silva, M. S. P. Mundim, R. Droppa Jr. and D. M. Fonseca *Physica B: Condens. Mat.* **370**, 90 (2005).

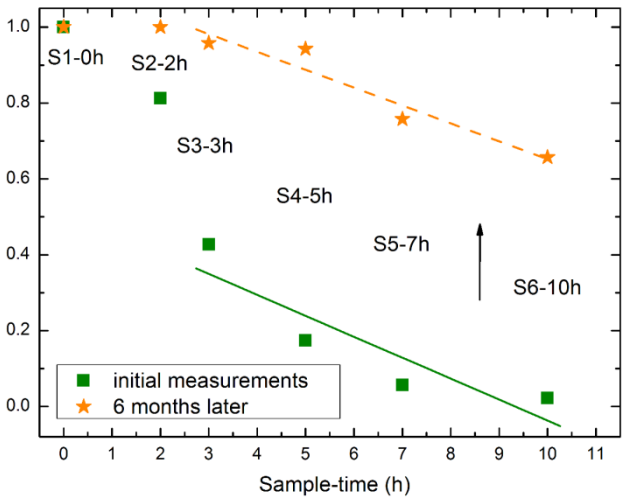

Figure 6. The ratios $I_1/(I_1+ I_2)$ between magnitudes of 0WL and 1 WL peak intensities for 6 samples (Set1-Temp). Their values are in range 0-1, where 0 indicates a pure dehydrated state, 0.5 is obtained when the number of clay particles in the two states are equal, whereas 1 depicts the pure mono-hydrated state.

3.3. Electric field induced alignment of clay particles

Figure 7 shows the two-dimensional WAXS patterns from paraffin/clay composites without (left) and with (right) an external electric field applied. The outermost ring originates from the Bragg 001 reflection that corresponds to the distance between clay's crystalline layers. It becomes anisotropic in the presence of an *E*-field, which indicates that clay particles are aligned with their stacking direction perpendicular to the *E*-field lines.

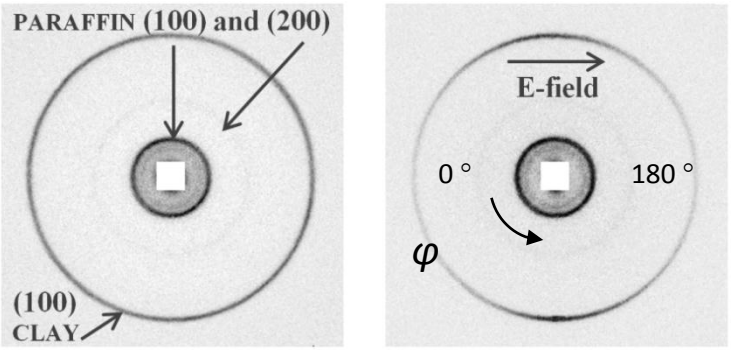

Figure 7. Two-dimensional WAXS patterns from paraffin/clay composites without (left) and with (right) an external *E*-field of 240 V/mm applied. The outermost ring from clay becomes anisotropic indicating that clay particles are aligned with their stacking direction perpendicular to the *E*-field lines.

To quantify the degree of anisotropy of the system, i.e. how well the clay platelets align with respect to the *E*-field direction, one needs to integrate the 2-D WAXS patterns (corresponding to the width of the 001 clay peak) radially over a narrow *q*-range and fit the obtained azimuthal plot to a Maier-Saupe function.[7] The result of such an integration is presented in Figure 8. Intensities of the anisotropic Bragg 001 rings are plotted as a function of the azimuthal angle φ. The peaks at around 90º and 270º indicate a stacking direction perpendicular to the *E*-field lines.

The degree of anisotropy was quantified by fitting the azimuthal plots to the Maier-Saupe function (for details see[12,34,35]). In short, the fitting parameter is a measure of the full width length at half maxima (smaller value equals a higher degree of anisotropy) and can be expressed as the nematic order parameter S_2. The parameter ranges from -1/2 to 1, where 1 indicates perfectly oriented particles in the nematic configuration, 0 states no orientational order, and finally -1/2 indicates perfectly oriented particles in the anti-nematic configuration.[11,34,35] It is expected here that the nematic order parameter should range between 0 and -1/2 since the clay particles align in the anti-nematic fashion and the validity of such an assumption is tested at the end of this section.

Figure 8 shows the azimuthal plots of the first Bragg peak amplitude under different *E*-field strengths for samples from Set2. The scattered points are the experimental data, whereas the fully drawn lines are the Maier-Saupe fits. As one can see, the width of the peaks decreases when the *E*-field strength increases, indicating better particle alignment. Calculations of averaged nematic order parameters (five measurements at different sample positions) for aligned clay particles in paraffin at different *E*-field strengths are presented in Table 1. The S_2 values are between -0.15±0.02 and -0.37±0.01, for *E*-field strengths from 30 to 480 V/mm.

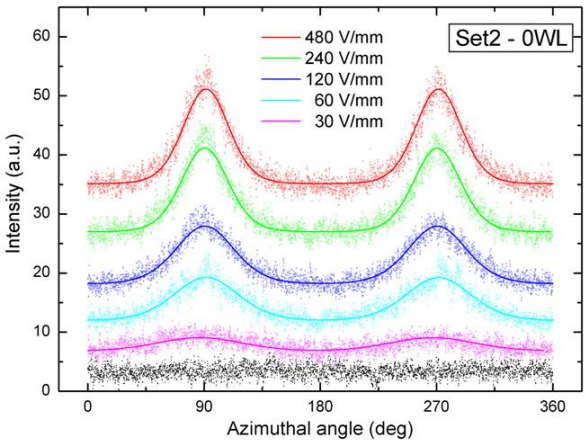

Figure 8. Azimuthal plots of the first Bragg peak amplitude at different *E*-field strengths.

E-field [V/mm]	30	60	120	240	480
S_2	**-0.15** ± 0.02	**-0.18** ± 0.06	**-0.28** ± 0.05	**-0.34** ± 0.02	**-0.37** ± 0.01

Table 1. Calculated nematic order parameters for clay particles aligned in paraffin matrix at different electric field strengths.

As opposed to the particle alignment in clay/silicone oil-suspension (at room temperature) studied previously, the particle orientations in the melted paraffin-wax are clearly *E*-field dependent. The paraffin-wax is significantly more viscous than the silicone oil used in the

[34] I. Dozov, E. Paineau, P. Davidson, K. Antonova, C. Baravian, I. Bihannic and L. J. Michot, *J. Phys. Chem. B* **115**, 7751–7765 (2011).
[35] Y. Méheust, K. D. Knudsen and J. O. Fossum, *J. Appl. Cryst.* **39,** 661 – 670 (2006).

previous work. The characteristic times, namely, the rotation time τ_R (alignment of clay particles along the *E*-field lines) and the two-particle collision (attraction) time τ_C, are longer, and both of them are E^2 dependent. It is yet possible that the ratio τ_R/τ_C is viscosity dependent so that a jamming situation may arise, i.e. particles do not have enough time to rotate completely before the chain-like structuring occurs. However, it is difficult to draw a firm conclusion from the measurements. This is an on-going study and more results are expected in the near future.

We also investigated the clay particle alignment as a function of the polar angle. Ninety two-dimensional WAXS images of the solidified sample were captured at different polar angles with the rotation axis parallel to the *E*-field direction. The nematic order parameters were calculated (in the same manner/fashion as before) for each sample position. The results are presented in Figure 9 where S_2 is plotted against the rotation angle. One sees that the nematic order parameters do not differ significantly from each other indicating that there is no preferential orientation along the polar angle. The arrowed disc shown in the inset of Figure 9 represents the plane normal to the *E*-field direction, and that is in fact the average particle stacking direction. This is a confirmation that the anti-nematic configuration applies for the particles.

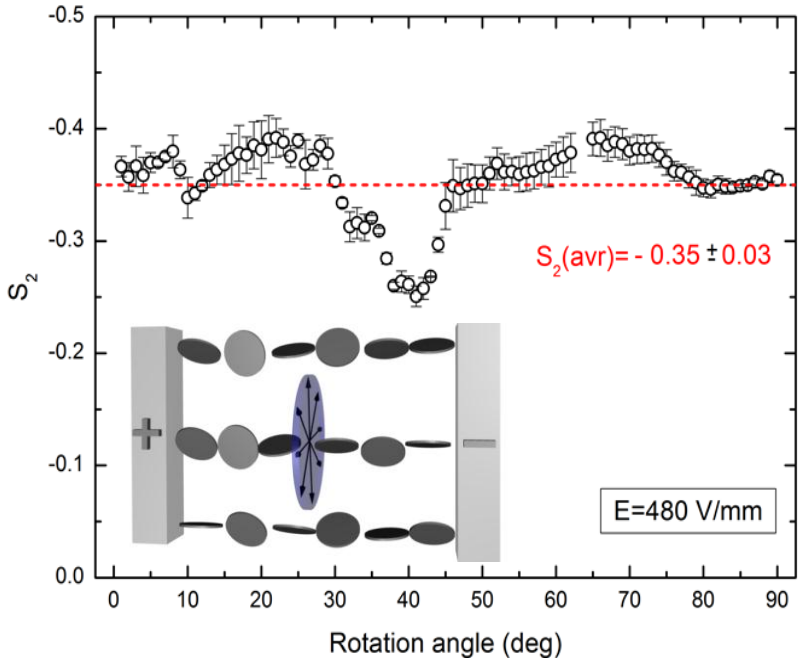

Figure 9. The nematic order parameter calculeted for different rotation angles. The avarage S_2 value is indicated as a dashed line.The inset shows a sketch of the clay alignment in a so-called anti-nematic configuration (see text for details).

3.4. Alignment of clays during paraffin melting and crystallization

To examine whether or not the alignment of clay particles may be disrupted during the paraffin crystallization, the nanoparticles dispersion state was monitored during heating and cooling using the custom made sample cell. X-ray diffractograms were first collected for samples at room temperature with no preferential orientation. Electric fields (125 and 250 V/mm) were applied from the beginning of the measurements, and they did not seem to affect the samples while in solid form. This is shown in Figure 10, where the nematic order parameter S_2=0 (in fact the zero value for frames 1-29 was ascribed by default, since it was not possible to converge the 1-D azimuthal plots with the fitting curve). The degree of anisotropy in the system increases when the paraffin starts melting (24 to 32 min), and S_2 reaches maximum values -0.26 and -0.36, for *E*–field strengths 125 and 250 V/mm, respectively. Interestingly, as time passes, the nematic order values decrease slightly and the average value calculated for time between 40-56 min (paraffin is completely melted and kept at ~100 °C) dropped by ~8 % and ~15 %, respectively. It thus seems that the better particle alignment is achieved before individual particles start forming chain-like structures. After 56 min the sample was cooled down. It took around 5 min for paraffin to start crystalizing. A small drop in S_2 was observed during that time, but only for the sample measured at high *E*-field. This might be caused by the paraffin crystallization. However, to be more conclusive on these two points, more measurements are needed. The final measured nematic order parameter values (last minutes - solid sample) are -0.28 and -0.32 for *E*-field strengths of 125 and 250 V/mm, respectively. These values are in the same range of values as were those obtained for samples from Set 3, described earlier in this article.

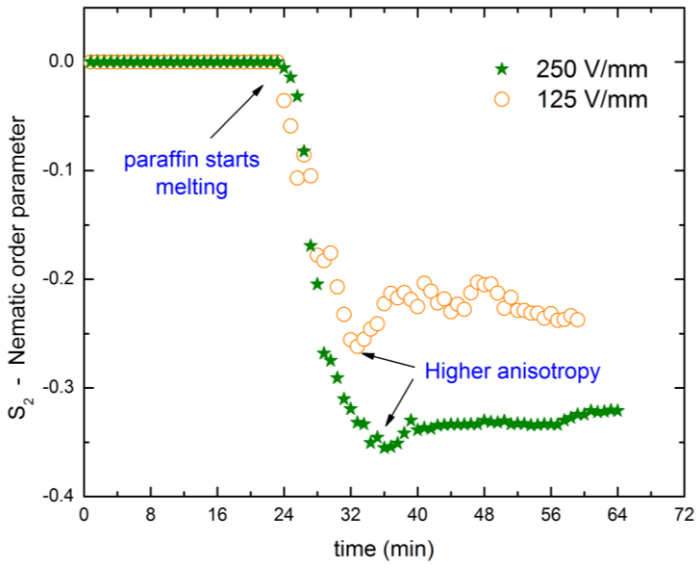

Figure 10. Development of the anisotropy in the system expressed by changes in the nematic order parameter S_2.

4. Conclusions

The primary objective of this research is to investigate the electric field induced alignment of fluorohectorite clay particles in oligomeric matrices. The degree of anisotropy dependence on the *E*-field strength has been quantified and presented in terms of the orientational order parameter S_2. It was found that at low *E*-fields (below 75 V/mm) the clay alignment is fairly low. Strong electric fields are therefore required to attain better alignment.

The development of the system anisotropy was observed during melting and crystallization of samples. Interestingly, it was found that on average the clay particles lose some of their orientational order in order to accommodate chain formation.

In addition, the dehydration of clay particles as a function of time was studied. It took nearly 10 h for the clay particles in the melted wax to nearly reach the pure 0WL hydration final state. However, the zero-to-one water layer transition for clay particles being embedded in crystalized paraffin is very slow. This is due to a very low water penetration through the oligomer matrix. Even after 6 months with air exposure (with ~55 % of RH), the sample still contains a population of clay particles possessing no or very little intercalated water.

Acknowledgement

The authors would like to thank Kenneth Dahl Knudsen for his comments that helped improve the manuscript, and also D. Chernyshov for his assistance while performing experiments at the Swiss-Norwegian Beam Lines at ESRF. Yves Méheust and Henrik Hemmen are acknowledged as creators of the script for fitting the data to the Maier-Saupe function. The 2-D WAXS diffractograms were analyzed using Fit2D created by A. P. Hammersley. This work was supported by the Research Council of Norway through the FRINAT Program: NFR project number 171300, the NANOMAT Program: NFR project number 182075 and the SYNKNØYT Program.

5. Supporting materials

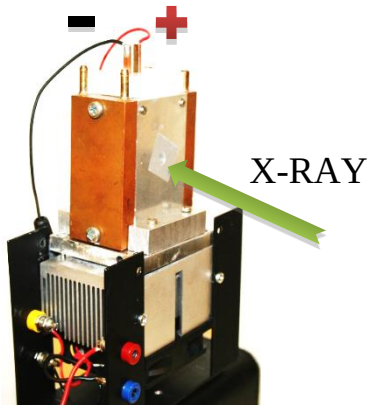

Figure S1. Experimental set-up for studying of dynamic alignment of clay particles during melting and crystallization of clay/paraffin-wax composites.

Bibliography

R S Allan and S G Mason. Particle behavior in sher and electric fields. *Proc. R. Soc. Lond.*, 267(1328):45–61, 1962.

N P Ashby and B P Binks. Pickering emulsions stabilised by laponite clay particles. *Chem. Phys.*, 2(24):5640, 2000.

Attension. `http://www.attension.com/surface-tension`. Accessed November 2011.

M Baviere. *Basic Concepts in Enhanced Oil Recovery Processes*. Springer., first edition, 1991.

J C Baygents, N J Rivette, and H A Stone. Electrohydrodynamic deformation and interaction of drop pairs. *J. Fluid Mech.*, 368:359–375, 1998.

F Bergaya, Theng B K G, and Lagaly G. Handbook of clay science. *Elsevier*, 2006. Amsterdam.

G Beson, C T Mitsud, and J Mering. *Clays Clay Miner.*, 22:379, 1974.

B P Binks. Particles as surfactants - similarities and differences. *Curr. Opin. Colloid In.*, 7 (1-2):21–51, 2002.

D E G Campos. Formao de emulses em uma juno de micro canais em T. Master thesis, PUC Rio, 2011.

F Cardarelli. *Materials handbook: A concise desktop reference*. Springer, second edition, 2008. p.1116.

Colepalmer. `http://www.coleparmer.com/catalog/product_view.asp?sku=7490300`. Accessed November 2011.

G J da Silva, J O Fossum, E DiMasi, K J Maloy, and S B Lutnaes. Synchrotron x-ray scattering studies of water intercalation in a layered synthetic silicate. *Phys.Rev. E*, 66:0113031–8, 2002.

G J da Silva, J O Fossum, E DiMasi, and K J Måløy. Hydration transitions in a nanolayered synthetic silicate: A synchrotron x-ray scattering study. *Phys.Rev. B*, 67:0941141–6, 2003.

DDBST. `http://ddbonline.ddbst.de/EE/11%20SFT%20(Surface%20Tension).shtml`. Accessed November 2011.

M De Menech, P Gartecki, F Jousse, and H A Stone. Transition from squeezing to dripping in a microfluidic T-shaped junction. *J. Fluid Mech.*, 595:141–161, 2008.

E DiMasi, J O Fossum, T Gog, and C Venkataraman. Orientational order in gravity dispersed clay colloids: A synchrotron x-ray scattering study of Na-fluorohectorite suspensions. *Phys. Rev. E*, 64:61704, 2001.

Dow. `https://dow-answer.custhelp.com/app/answers/detail/a_id/1666/~/triton-x-100-surfactant-surface-tension`. Accessed April 2012.

R Dreyfus, P Tabeling, and H Willaime. Ordered and disordered patterns in two-phase flows in microchannels. *Phys. Rev. Lett.*, 90:144505, 2003.

W Ehrfeld, V Hessel, H Mobius, T Richter, and K Russow. *Dechema*, 132(1), 1996.

J Q Feng. Electrohydrodynamic behavior of a drop subjected to a stteady uniform electric field at finite electric Reynolds number. *Proc. R. Soc. Lond.*, A 455:2245–2269, 1999.

J O Fossum, Y Meheust, K P S Parmar, K D Knudsen, K J Måløy, and D M Fonesca. Intercalation-enhanced electric polarization and chain formation of nano-layered particles. *Europhys. Lett.*, 74(3):438–444, 2006.

J C P Gabriel, C Sanchez, and P Davidson. Observation of nematic liquid-crystal textures in aqueous gels of smectite clays. *J. Phys. Chem.*, 100:11139–11143, 1996.

P Garstecki, H A Stone, and G M Whitesides. Mechanism for flow-rate controlled breakup in confined geometries - a route to monodisperse emulsions. *Phys. Rev. Lett.*, 94:164501, 2005.

P Garstecki, M J Fuerstman, H A Stone, and G M Whitesides. Formation of droplets and bubbles in a microfluidic T-junction - scaling and mechanism of break-up. *Lab on a Chip*, 6: 437–446, 2006.

D J Griffiths. *Introduction to Electrodynamics*. Prentice-Hall International Inc., third edition, 1999.

W Ha and S M Yang. Electrohydrodynamics and electrorotation of a drop with fluid less conductive than that of the ambient fluid. *Phys. Fluids*, 12(764), 2000.

K Hersvik. Oil-oil droplet deformation under DC electric field as a method to investigate clay electrorheology. Master thesis, NTNU, July 2010.

S C Jakeway and Russel E L de Mello, A J. Miniaturized total analysis systems for biological analysis. *Fresen. J. Aal. Chem.*, 366:525–539, 2000.

P D Kaviratna, T J Pinnavaia, and P A Schroeder. Dielectric properties of smectite clays. *J. Phys. Chem. Solids*, 57:1897–1906, 1996.

T Kawakatsu, Y Kikuchi, and M Nakajima. Regular-sized cell creation in microchannel emulsification by visual microprocessing method. *J. Am. Oil Chem Soc.*, 74:317–321, 1997.

S H Kim, J Eun-Ju, Y Jung, M Han, and S J Park. Ionic conductivity of polymeric nanocomposite electrolytes based on poly(ethylene oxide) and organo-clay materials. *Colloid Surface*, 313:216–219, 2008.

I Kobayashi and M Nakajima. Effect of emulsifiers on the perparation of food grade oil-in-water emulsions using a straight-through extrusion filter. *Eur. J. Lipid Sci. Tech.*, 104:720–727, 2002.

I Kobayashi, M Nakajima, K Chun, Y Kikuchi, and H Fujita. Silicon array of elongated through-holes for monodisperse emulsion droplets. *AIChE J.*, 48:1639–1644, 2001.

I Kobayashi, S Mukataka, and M Nakajima. Effect of type and physical properties of oil phase on oil-in-water emulsion droplet formation in straight through microchannel emulsification, experimental and CFD studies. *Langmuir*, 21(2):5722–5730, 2005.

S Kokal. Crude-oil emulsions: A state-of-the-art review. *SPE Prod. Facil.*, 20:5–13, 2005.

C T Konski and H C Tacher Jr. The distortion of aerosol droplets by an electric field. *J. Phys. Chem.-US*, 57:955–958, 1953.

S Krause and P Chandratreya. Electrorotation of deformable fluid droplets. *J. Colloid Interface Sci.*, 206(10), 1998.

X B Li, F C Li, J C Yang, H Kinoshita, M Oishi, and M Oshima. Study on the mechanism of droplet formation in T-junction microchannel. *Chem. Eng. Sci.*, 69:340–351, 2012.

J R Lien and G Løvhøiden. *Generell fysikk for universiteter og høgskoler*. Bind 1. Universitetsforlaget, second edition, 2001. p.251-259.

T G Mason and J Bibette. Shear rupturing of droplets in complex fluid. *Langmuir*, 19:4600–4613, 1997.

J R Melcher and G I Taylor. Electrohydrodynamics: A review of the role of interfacial shear stresses. *Annu. Rev. Fluid Mech.*, 1(1):111–146, 1969.

T Nakashima, M Shimizu, and M Kukizaki. Membrane emulsification by microporous glass. *Key Eng. Mat.*, 513:61–62, 1991.

T Nisisako and T Torii. Formation of biphasic janus droplets in a microfabricated channel for the synthesis of shape controlled poymer microparticles. *Advanced Mater.*, 19:1489–1493, 2007.

T Nissiako, T Torii, and T Higuchi. Droplet formation in a microchannel network. *Lab on a Chip*, 2:24–26, 2002.

X Niu, M Zhang, J Wu, W Wen, and P Sheng. Generation and manipulation of smart droplets. *Soft Matter*, 5:576–581, 2009.

I E Odom. Smectite clay minerals: Properties and uses. *Phil. Trans. R. Soc. Lond. A*, 311: 391–409, 1984.

Web of knowledge. `http://apps.webofknowledge.com/`. Searched for **clay suspension** in topics. Accessed May 2012.

C Oriakhi. Nano sandwiches. *Chem. Br.*, 34:59–62, 1998.

G Quincke. Ueber rotationen im constanten electrishen felde. *Annalen der Physik*, 295(11): 417–486, 1896.

N B Raikar, S R Bhatia, M F Malone, and M A Henson. Experimental studies and population balance equation models for breakage prediction of emulsion drop size distributions. *Chem. Eng. Sci.*, 64:2433–2447, 2009.

D Ratna, S Divekar, A B Samui, B C Chakraborty, and A K Banthia. Poly (ethylene oxide)/clay nanocomposite: Thermomechanical properties and morphology. *Polymer*, 47:4068–4074, 2006.

M Rhodes. *Introduction to Particle Technology.* John Wiley and Sons, Ltd, Chichester, UK, second edition, 2008.

Additives Limited Rockwood. Laponite technical brochure. `http://www.scprod.com/pdfs/Laponite%20brochure%20EN.pdf`, 2010. Accessed March 2012.

Z Rozynek, K D Knudsen, J O Fossum, Y Meheust, B Wang, and M Zhou. Electric field induced structuring in clay-oil suspensions: New insights from WAXS, SEM, leak current, dielectric permittivity, and rheometry. *J. Phys.: Condens. Matter*, 22:324104, 2010.

P F Salipante and P M Vlahovska. Electrohydrodynamics of drops in strong unifrom dc electric fields. *Phys. Fluids*, 22(112110):1–9, 2010.

H Sato, N Kaji, T Mochizuki, and Y H Mori. Behavior of oblately deformed droplets in an immiscible dielectric liquid under a steady and uniform electric field. *Phys. Fluids*, 18 (127101), 2006.

D A Saville. Electrohydrodynamics: The Taylor-Melcher leaky dielectric model. *Annu. Rev. Fluid Mech.*, 29:27–64, 1997.

V Schroder, O Behrend, and H Schubert. Effect of dynamic interfacial tension on the emulsification process using micropourous ceramic membranes. *J. Colloid Interf. Sci.*, 202:334–340, 1998.

3B Scientific. `http://www.3bscientific.com/Gay-Lussac-Pycnometer-U14220,p_83_110_583_1062.html`. Accessed April 2012.

H Song, D L Chen, and R F Ismagilov. Reactions in droplets in microfluidic channels. *Angew. Chem., Int. Ed.*, 45:7336–7356, 2006.

R Srinivasan, I Hsing, P Berger, K Jensen, S Firebaugh, M Schmidt, M Harold, J Lerou, and J Ryley. *AIChE J.*, 43(11), 1997.

H A Stone, A D Stroock, and A Ajdari. Engineering flows in small devices: Microfluidics toward a lab-on-a-chip. *Annu. Rev. Fluid Mech.*, 36:381–411, 2004.

Nakajima M Sugiura, S, S Iwamoto, and S Seki. On water-in-oil emulsions stabilized by fine solids. *Langmuir*, 17:5562, 2001.

S Sugiura, M Nakajima, T Oda, M Satake, and M Seki. Effect of interfacial tension on the dynamic behavior of droplet formation during microchannel emulsification. *J. Colloid Interf. Sci*, 269:178–185, 2004.

P Tabeling. *Introduction to microfluidics*. Oxford University Press, New York, 2005. p. 105-117.

Y C Tan, J S Fisher, A I Lee, V Cristini, and A P Lee. Design of microfluidic channel geometries for the control of droplet volume, chemical concentration, and sorting. *Lab on a Chip*, 4: 292–298, 2004.

G Taylor. Studies in electrohydrodynamics. I. the circulation produced in a drop by electrical field. *Proc. R. Soc. Lond.*, A 291:159–166, 1966.

Ltd The Dolomite Centre. Information sheet mitos thin layer T-junction chip with header.

T Thorsen, R W Roberts, F H Arnold, and Quake S R. Dynamic pattern formation in a vesicle-generating microfluidic device. *Phys. Rev. Lett.*, 86:4163–4166, 2001.

J D Tice, H Song, A D Lyon, and R F Ismagilov. Formation of droplets and mixing in multiphase microfluidics at low values of the Reynolds and the capillary numbers. *Langmuir*, 19:9127–9133, 2003.

J D Tice, A D Lyon, and R F Ismagilov. Effect of viscosity on droplet formation and mixing in microfluidic channels. *Anal. Chim. Acta*, 507:73–77, 2004.

S Torza, R G Cox, and S G Mason. Electrohydrodynamic deformation and burst of liquid drops. *Philos. T. Roy. Soc. A*, 269(1198):295–319, 1971.

P B Umbanhowar, V Prasad, and D A Weitz. Monodisperse emulsion generation via drop break off in a coflowing stream. *Langmuir*, 16(2):347–351, 2000.

S van der Graaf, C G P H Schroen, R G M van der Sman, and R M Boom. Influence of dynamic interfacial tension on droplet formation during membrane emulsification. *J. Colloid Interf. Sci.*, 277:456–463, 2004.

S van der Graaf, M L J Steegmans, R G M van der Sman, C G P H Schroen, and R M Boom. Droplet formation in a T-shaped microchannel junction: A model system for membrane emulsification. *Colloid Surface A*, 266:106–116, 2005.

V van Steijn, M T Kreutzer, and C R Kleijn. μ-piv study of formation of segmented flow in microfluidic T-junctions. *Chem. Eng. Sci.*, 62:7505–7514, 2007.

B Velde. *Introduction to Clay Minerals*. Chapman and Hall, London, 1992.

O Vizika and A Saville. The electrohydrodynamic deformation of drops suspended in liquids in steady and oscillatory electric fields. *J. Fluid Mech.*, 239:1–22, 1992.

H J Walls, M W Riley, R R Singhal, R J Spontak, P S Fedkiw, and Khan S A. Nanocomposite electrolytes with fumed silica and hectorite clay networks: Passive versus active fillers. *Adv. Funct. Mater*, 13(9):710–717, 2003.

B Wang, M Zhou, Z Rozynek, and J O Fossum. Behavior of oblately deformed droplets in an immiscible dielectric liquid under a steady and uniform electric field. *J. Mater. Chem.*, 19: 1816–28, 2009.

H Z Wang, X Y Li, M Uehara, Y Yamaguchi, H Nakamura, M P Miyazaki, H Shimizu, and H Maeda. Continous synthesis of CDSe-ZnS composite nanoparticles in a microfluidic reactor. *Chem. Commun.*, pages 48–49, 2004.

B Weigl and K Hedine. *Am. Biotechnol. Lab.*, 28, January 2002.

W Wen, X Huang, K Lu, and P Sheng. The giant electrorheological effect in suspensions of nanoparticles. *Nature Mater.*, 2:727–730, 2003.

W M Winslow. US patent ppecification 2517850, 1947.

J H Xu, S W Li, J Tan, Y J Wang, and G S Luo. Controllable preparation of monodisperse O/W and W/O emulsions in the same microfluidic device. *Langmuir*, 22:7943–7946, 2006a.

J H Xu, S W Li, J Tan, Y J Wang, and G S Luo. Preparation of highly monodisperse droplet in a T-junction microfluidic device. *AIChE Journal*, 52:3005–3010, 2006b.

J H Xu, G S Luo, and G G Chen. Shear force induced monodisperse droplet formation in a microfluidic device by controlling wetting properties. *Lab on a Chip*, 6:131–136, 2006c.

J H Xu, S W Li, J Tan, and G S Luo. Correlations of droplet formation in T-junction microfluidic devices: from squeezing to dripping. *Microfluidics and Nanofluidics*, 5:711–717, 2008.

N X Yan and J H Masliyah. Adsorption and desorption of clay particles at the oil-water interface. *J. Colloid Interf. Sci.*, 168(2):386–392, 1994.

N X Yan, M R Gray, and J H Masliyah. On water-in-oil emulsions stabilized by fine solids. *Colloid. Surface. A*, 193(1-3):97–107, 2001.

C X Zhao and A P J Middelberg. Two-phase microfluidic flows. *Chem. Eng. Sci.*, 66:1394–1411, 2011.

B Zheng and R F Ismagilov. Reactions in droplets in microfluidic channels. *Angew. Chem., Int. Ed.*, 44:2520–2523, 2005.

E K Zholkovskij, J H Masliyah, and J Czarnecki. An electrokinetic model of drop deformation in an electric field. *J. Fluid Mech.*, 472:1–27, 2002.